CARBON FORMATION IN SOLID OXIDE FUEL CELLS DURING INTERNAL REFORMING AND ANODE OFF-GAS RECIRCULATION

BY

Tsang-I Tsai

A thesis submitted to
The University of Birmingham
For the degree of
DOCTOR OF PHILOSOPHY

Centre for Hydrogen and Fuel Cell Research
School of Chemical Engineering
Edgbaston, Birmingham, B15 2TT, UK

May 2015

UNIVERSITY OF
BIRMINGHAM

University of Birmingham Research Archive

e-theses repository

This unpublished thesis/dissertation is copyright of the author and/or third parties. The intellectual property rights of the author or third parties in respect of this work are as defined by The Copyright Designs and Patents Act 1988 or as modified by any successor legislation.

Any use made of information contained in this thesis/dissertation must be in accordance with that legislation and must be properly acknowledged. Further distribution or reproduction in any format is prohibited without the permission of the copyright holder.

Abstract

The formation of solid carbon is one of the main drawbacks of methane internal reforming at the anodes of Solid Oxide Fuel Cells (SOFCs). In practical applications, Anode Off-Gas Recycling (AOGR) has been introduced to overcome this issue. However, the recycled non-fuel gas dilutes the fuel concentration and lowers the cell performance. As a result, an optimum amount of exhaust gases and the boundary of carbon formation need to be well studied to determine the recycling conditions of the anode off-gas.

Commonly, two modelling approaches have been developed in this topic: a Carbon-Steam Equilibrium (C-S EQ) and a kinetic Carbon Activity (CA) approach. The C-S EQ approach can well predict the carbon formation in steam reforming of methane, but cannot deal with a system that contains carbon oxides like in AOGR; whilst the kinetic CA approach can be applied to a system that contains carbon oxides, but usually provides unreasonable results. Furthermore, very few details for both approaches on the theories and mathematical calculations have been provided.

First, detailed theories for building the model are presented, then, the C-S EQ and the kinetic CA approaches are compared and discussed, from their own theories to application conditions. The necessity for the evolvement of the Reversed Syngas Formation (RSF) reaction in the kinetic CA approach is demonstrated, for providing identical results as C-S EQ in steam reforming of methane.

The modified CA approach is then applied to a system containing carbon oxides, combined steam and dry methane reforming, and the results are evaluated by practical experiments. Different oxygen to carbon atomic ratios (i.e. 1.0 - 1.75) with various contents of methane, steam and carbon dioxide, are employed in the modelling and practical experiments to examine methane reforming and carbon formation.

Finally, the modified CA approach is used for a methane fed SOFC with anode recirculation system by integrating steam reforming, an SOFC unit, recirculation and carbon formation models. The combination of different fuel current densities (i.e. 0.5, 1.0 and 1.4 A cm^{-1}), steam to methane ratios (i.e. 0.25 - 4.0) in the fuel and different recycling rates (i.e. 10% - 90%) are employed in the model to investigate the effects of fuel conditions on the system operation.

Evolve every moment, survive everywhere.

Acknowledgements

My heartfelt appreciation goes to my six supervisors: Prof. Robert Steinberger-Wilckens, Prof. Kevin Kendall, Prof. Bruno Pollet, Dr. Philip Robbins, Dr. Waldemar Bujalski, and Dr. Aman Dhir for their enormous support and insightful comments which were invaluable during the course of my study.

I am also indebted to Dr. Shangfeng Du, Dr. Artur Majewski, Dr Arthur Williams, Dr Yu Rong and Mrs Lynn Draper who provided technical help and sincere encouragement. This work could never have been completed without their support.

I would like to further extend my appreciation to my colleagues and friends: Katie, Natascha, Zoe, Hoyyen, Beatrice, Philip, Jonathan, Jason, Lina, Ahmad, Tom and Peter for their kind support and useful discussions.

Finally, and most importantly, I would like to thank my family for their tremendous support and encouragement.

Contents

List of Figures

List of Tables

List of Symbols

Latin Letters		Units
A	Area	m^{-2}
a	Moles consumed/produced by steam methane reforming	mol s^{-1}
$\mathcal{A}$	Coefficients for current densities	
$\mathscr{a}$	Chemical activity	
B	Boltzmann constant = $1.3806488(13)\times10^{-23}$	J K^{-1}
b	Moles consumed/produced by water gas shift reaction	mol s^{-1}
$\mathcal{B}$	Coefficients for current densities	
$\mathcal{C}$	Effective factor	
D	Pre-exponential factor for adsorption constant	
$\mathcal{D}$	Pre-exponential factor for rate constant	
E	Potential voltage	V
e	Electron charge = -1.602×10^{-19}	A s
$\mathcal{E}$	Energy	J
F	Faraday constant = 9.6485×10^{4}	A s mol^{-1}
$\mathcal{F}$	Ratio between adsorption and desorption	
G	Gibbs free energy	J
H	Enthalpy	J

I	Current	A
j	Current density	A m^{-2}
K	Thermodynamic equilibrium	
k	Adsorption constant	Kpa^{-1}
$\mathscr{k}$	Rate coefficient	
l	Length	m
N	Electron transfer number	
n	Molecule number	Mole
O/C	Oxygen to carbon	
P	Pressure	N m^{-2}
Q	Reaction quotient	
q	Heat	J
R	Gas constant = 8.314	J mol^{-1} K^{-1}
r	Reaction rate	
S	Entropy	J K^{-1}
S/C	Steam to carbon	
T	Temperature	K
t	Time	s
U	Internal energy	J

u	utilisation	
V	Voltage	V
v	Volume	m^3
W	Power	W
w	Work	J

Greek Letters

α	Carbon activity	
γ	Product of carbon activities	
ε	Porosity	
η	Efficiency	
θ	Covered surface	
ν	Gas flow rate	
ρ	Electrical resistivity	$\Omega\ m^{-1}$
ψ	Steam to methane ratio	

Subscripts and Superscripts

ads	Adsorption
act	Activation
an	Anode
C	Concentration
ca	Cathode
cell	Fuel cell
chan	Fuel passing channel
con	Concentration
des	Desorption
f	Fuel
el	Electrolyte
elec	Electrical
eq	Thermodynamic equilibrium
j_o	Exchange current density
L	Limit
Ner	Nernst
ohm	Ohmic
ox	Oxidation

P	Pressure
res	Reversible
red	Reduction
Thermo	Thermodynamic
V	Voltage

Abbreviations

AOGR	Anode off-gas recirculation
APU	Auxiliary power unit
ATR	Autothermal reforming
BD	Boudouard reaction
CA	Carbon activity
CAT	Catalyst
CEA	Chemical equilibrium with applications (software)
CHP	Combined heat and power
COx	Carbon monoxide oxidation reaction
CPOx	Catalyst partial oxidation
C-S EQ	Carbon-steam equilibrium
DAQ	Data acquisition
DIR	Direct internal reforming
DG	Decentralised generation
DR	Dry methane reforming
EMF	Electromotive Force
FOx	Methane full oxidation reaction
F-T	Fischer-Tropsch synthesis

GC	Gas chromatography
GHG	Greenhouse gas
GIR	Gradual internal reforming
HALE	High-altitude-long-endurance
HHV	Higher heating value
HOR	Hydrogen oxidation reaction
ICE	Internal combustion engine
LED	Light-emitting diode
LHV	Lower heating value
LPG	Liquefied petroleum gas
LSM	Lanthanum strontium manganite
MC	Methane cracking reaction
MFC	Mass flow controller
MOSFET	Metal–oxide–semiconductor field-effect transistor
MS	Mass spectrometry
NASA	National aeronautics and space administration
OCV	Open circuit voltage
OSR	Oxidative steam reforming
ORR	Oxygen reduction reaction

PEFC	Polymer electrolyte fuel cell
POx	Methane partial oxidation reaction
PPM	Parts per million
RSF	Reverse syngas formation
SiC	Silicon carbide
SF	Syngas formation
SMR	Steam methane reforming
SOFC	Solid oxide fuel cell
TCD	Thermo conductivity detector
TGA	Thermogravimetric analysis
TPB	Triple phase boundary
TPO	Temperature programmed oxidation
TPR	Temperature programmed reduction
UAV	Unmanned aerial vehicle
WGS	Water gas shift reaction
XRF	X-ray fluorescence
YSZ	Yittria stabilised zirconia

Chapter 1 Applications of Solid Oxide Fuel Cells

1.1 Introduction

As one of the most promising energy conversion devices, fuel cells have received increasing attention due to their high energy conversion efficiency, specific energy density (both gravimetric and volumetric energy density) and potentially low green house gas (GHG) emissions. Among the different types of fuel cell, the high operating temperatures of Solid Oxide Fuel Cells (SOFCs) allow more flexibility with regard to fuel selection, ranging from pure hydrogen to various hydrocarbons such as natural gas and biogas [1]. In addition, with a wide range of power output, SOFCs can be applied in various areas including portable power supply, transportation, and stationary power generation [2, 3].

SOFCs are well suited to portable applications due to their low weight. Both the components, and the fuel itself, tend to be much lighter than conventional energy generation technologies. However, carbon formation caused from the use of hydrocarbon as the fuel can shorten the cell operation life, or damage the cell.

Additional equipment is often required to overcome this problem and this adds the complexity and weight to the system. This disadvantage needs to be addressed before SOFC can be applied to the portable application fields.

Stationary applications, ranging from domestic power and heat generation to large power plants, require a longer operation life. In this case, it is more important for these cells to avoid carbon formation. For transportation applications, SOFCs can be utilised as the Auxiliary Power Unit (APU), or the main power supply for propulsion in small vehicles such as Unmanned Aerial Vehicles (UAVs) [4]. Two requirements of power supplies for APUs are reliability, and the ability to provide enough electrical power for the onboard equipment after being launched.

In this chapter, different kinds of application for SOFC are first listed then the suitable scenarios and reasons for choosing SOFC will be discussed. Then the aim of this thesis is presented at the end of this chapter.

1.2 Applications

1.2.1 Decentralised Generation and Combined Heat and Power

There are several advantages for applying SOFC to Decentralised Generation (DG).

The first one is reducing transmission losses since the electricity is generated right at the demand site. Secondly, SOFC's high operating temperature can also provide heat for households or other demands (e.g. steam generation, process heat, ad-/absorption cooling). The whole system can provide both heat and power (called cogeneration, or, Combined Heat and Power, CHP), and the total system efficiency can be up to 88% [5-8]. In CHP applications, weight and volume are of little concern, so this area does not have the same constraints as mobile applications. SOFC systems can more or less compete with Internal Combustion Engines (ICEs) with regard to power density. Finally, unlike hydrogen, the infrastructure for natural gas and Liquefied Petroleum Gas (LPG), which are suitable fuels for SOFCs, are already established [5, 9]. Other fuels like diesel, ethanol and methanol can also be used for SOFC DG applications as they are readily available. However, longer operation time running on hydrocarbon fuels can lead to carbon formation. This is an issue that needs to be focused. An 100 kW SOFC CHP system running on natural gas was demonstrated in the Netherlands back in 2000 [10]. Many power suppliers in South Korea are also interested in building SOFC DG to supply heat and electricity for households [11].

1.2.2 Portable Applications

The high operating temperatures of SOFCs make them difficult to be applied to personal devices for the general public. However, they have attracted considerable attention from the military. The higher cost of a fuel cell would still be accepted in military applications if products are able to meet the functional requirements such as low weight, high efficiency, low noise, and fuel flexibility [11]. Demonstrating this point, five 25 W SOFC systems were developed by Adaptive Materials Inc. for the medical readiness training exercise in 2009 [12]. An amount of $1.4 million was provided by the US military for Protonex to develop a 500 - 1000 W liquid-fuel-fed SOFCs [12].

Due to the reforming process inside the cell (see Chapter 2), hydrocarbon fuels can also be directly used for SOFC. Propane, as an example, can be a fuel choice, and has the additional advantage that it is liquid at room temperature and moderate pressure, which means a higher energy volumetric density than other gas-phase fuels. However, these liquid fuels are prone to carbon formation and shorten the operation life.

Figure 1-1 shows a comparison of energy densities for various fuels. Although the liquid fuels generally have higher volumetric energy densities and are more easily implemented in applications than the gaseous ones, they are more likely to cause carbon deposition on the anode (see section 2.6), which leads to performance degradation [13]. When the liquid fuels are used to power SOFCs, evaporation technology is used to convert the liquid fuel into the gas phase. The Oel-Wärme-Institut, for instance, developed a processor with a "cool frame" technology, which vaporises the liquid fuel at temperatures above 723 K [14].

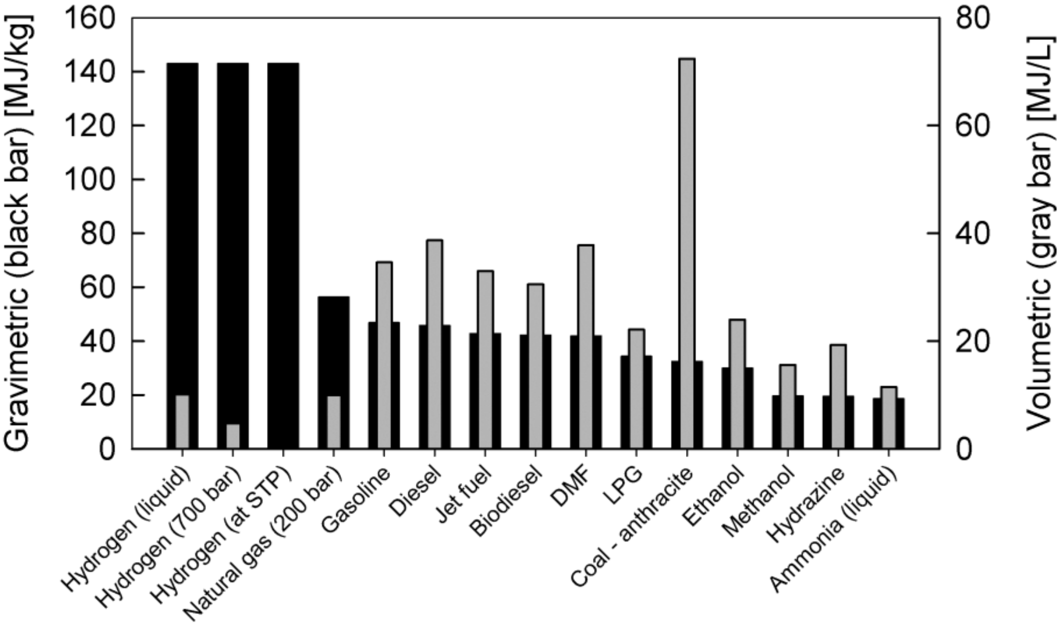

Figure 1-1 Comparison of different energy densities for some common fuels [13].

1.2.3 Auxiliary Power Units

For large and complex vehicles, power is required for more than just propulsion. Onboard equipment such as air conditioning, electronic devices, lighting, and navigation all require electricity. However, the main engine usually produces significant noise and pollution, and has a very low overall electrical efficiency when in operation. As a parallel power source to the main engine, an APU can supply the electricity demand whilst the main engine is off. SOFC APUs are also expected to save fuel because of their high efficiency, as well as reduce the danger of being traced when applied in military field due to their low noise and good thermal management.

In 2001, an SOFC APU was successfully demonstrated by Delphi Automotive Systems and BMW [15, 16]. A diesel-based SOFC APU was demonstrated by Webasto in 2005 [17]. Delphi plans to provide 5 kW SOFC APU systems which can utilise various kinds of fuel including natural gas, propane and diesel reformate [18]. Thyssenkrupp Marine Systems is working on a 500 kW APU for ships [19].

1.2.4 Unmanned Aerial Vehicles

The low power demand and low weight requirements of High-Altitude Long-Endurance (HALE) UAVs can be satisfied by fuel cell systems either operating alone, or combined with batteries to supply the required power. Both Polymer Electrolyte Fuel Cells (PEFCs) and SOFCs have been investigated by the US Air Force Research Laboratory and National Aeronautics and Space Administration (NASA) [20, 21]. The limitation of water management required by PEFCs at low pressure and temperature can be overcome by SOFCs, as their high working temperature keeps water vaporised [22]. Kim and Kwon [23] also suggested that higher energy densities can be obtained from a hydrocarbon fuel fed SOFC. However, some disadvantages of using SOFCs as a source of power were pointed out by Aguiar et al. [22], such as longer starting time, and poorer dynamic response as compared to PEFC due to the fuel processing when hydrogen is not used as the fuel. An investigation into a small, low-altitude UAV project named "Endurance" was conducted by the University of Michigan. This UAV was powered by μSOFCs and was recorded travelling 159 km in 10 hours and 15 minutes [11]. Adaptive Materials was awarded a grant for developing an SOFC stack for powering a UAV and its radio systems for the US military [24].

1.3 Thesis Aims

When hydrocarbons are used as fuel for SOFCs, solid carbon may form under certain operating conditions (see section 2.5). Deposited solid carbon covers the porous anode and nickel catalyst, blocking gas transport and lowering catalytic activity. A lower cell performance is then obtained since the blocked channels lowers the concentrations of reactants and slows down the reaction rates. The reduced catalytic activity leads to an even lower reformation of methane, which has a much slower oxidation rate. Meanwhile, the high methane concentration comes due to the low methane reformation further enhances carbon formation. As a result, the SOFCs can be out of functions within a short operation period.

Two methods have been mentioned in literature to avoid carbon formation in SOFCs: 1) increasing the water vapour concentration at fuel inlet, and 2) increasing the operating temperature. Both of them can shift the reaction direction and prevent carbon formation [25-28]. However, the provision of additional water or carbon dioxide at the fuel inlet increases the system complexity, because the additional water needs to be heated before being fed into the cells, and the additional carbon dioxide implies another gas source is required. The former method can lead to a large temperature gradient and crack the cell, whilst the latter method increases the difficulty of commercialisation. Those disadvantages need to be overcome before SOFCs can be applied as portable power source devices.

The Anode-Off Gas Recirculation (AOGR) can be employed to overcome these problems as both water and carbon dioxide are the products of SOFC electrochemical reactions. They are produced from the oxidation of hydrogen and carbon monoxide, respectively. Moreover, these gases are directly from the cell itself so they are having a similar temperature to the cell itself, which can theoretically eliminate the demand of pre-heater and lower the complexity of the system. However, high steam or carbon dioxide concentrations or recycling rates will dilute the fuel concentration and finally results in a low cell performance.

The aim of this work is to design a high efficiency SOFC system with anode recirculation for biogas or natural gas. This will be achieved by computer modelling to find a common approach to determine the minimal water concentration and recycling rate to optimise the system, under different fuel compositions and operating conditions. Two methods for determining carbon formation based on thermodynamic equilibrium are proposed by other researchers. However, the complete theories, mechanisms, results and conditions of applications have rarely been provided. In this thesis, these two methods are compared, from theories, mechanism, results and the conditions under which these two methods can be applied. Then the combined steam and dry methane reforming is examined by approaches from both thermodynamic equilibrium modelling and experimental validation. Finally, these methods are then used in a model of an SOFC system with anode recirculation to examine the interactions among the fuel composition, cell operating condition, carbon deposition, and the recirculation rate.

The next chapter starts with a literature review by discussing solid oxide fuel cells and their fuels, followed by 0, which explains the theories used for building models and the experimental setup. The two modelling approaches for determining carbon formation are discussed and compared in Chapter 4, followed by the modelling approach and experimental verification of the combined steam and dry reforming of methane in Chapter 5. Chapter 6 presents the modelling results of the SOFC with internal methane steam reforming, anode recirculation and carbon deposition system. The conclusions and future work are presented in Chapter 7.

Chapter 2 Solid Oxide Fuel Cells and Their Fuels

As a promising energy conversion device, SOFCs can reach more than 60% electrical efficiency, and 88% overall efficiency can be expected when used as a cogeneration system [5, 29-31]. Moreover, the high operating temperatures enable hydrocarbon reforming inside the cells which brings in a higher flexibility in the fuel selection in SOFCs than other types of fuel cells. However, poisoning elements such as solid carbon, sulphur, and tar from hydrocarbon fuels can shorten the lifetime or even destroy the cell [32, 33].

In this chapter, an introduction about the SOFC operating principle and main components were firstly presented. Following this, the potential fuels such as methane/natural gas and other larger molecular hydrocarbons were discussed individually. Then, a special focus on the poisoning elements, in particular the carbon deposition in SOFC anodes, were discussed, followed by the methods of the SOFC protection. Finally, the state-of-the-art about methane reforming, carbon formation and SOFC systems were presented.

2.1 Solid Oxide Fuel Cells

2.1.1 Operating Principle

Figure 2-1 demonstrates the SOFC working mechanism. At the cathode, oxygen molecules from the air are reduced by receiving four electrons from the external electrical circuit, leading to the formation of two oxygen ions. This reaction is called the Oxygen Reduction Reaction (ORR, Equation 2.1), and is the rate limiting step in the cell electrochemistry [34].

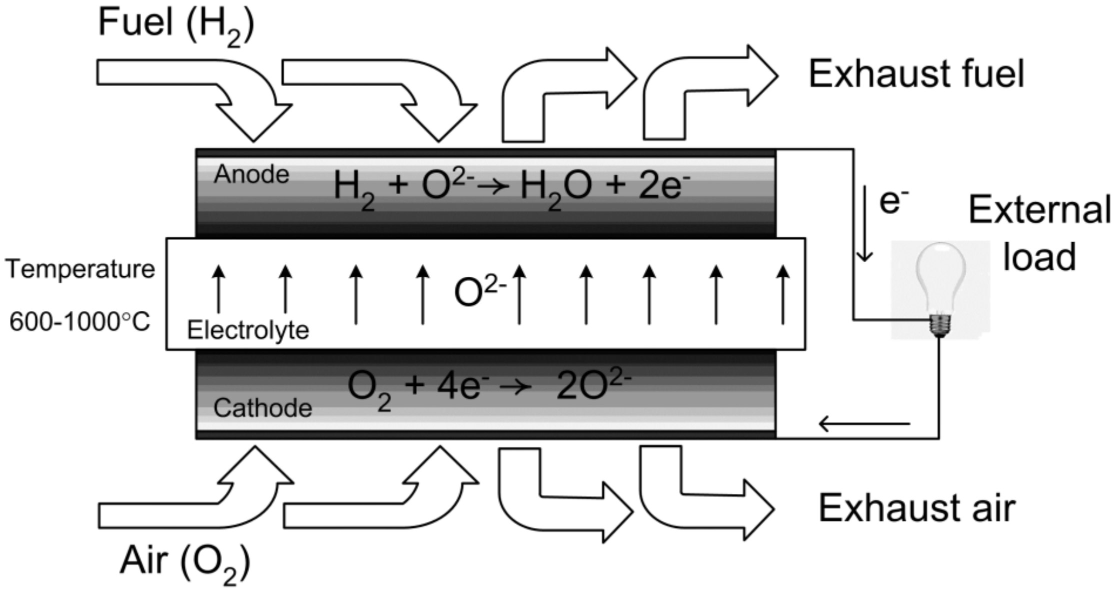

Figure 2-1 Fuel cell operating principle [13].

The ORR contains several steps: 1) The oxygen molecule is adsorbed onto the surface, then dissociates. 2) The dissociated oxygen molecule then diffuses from the surface to the Triple Phase Boundary (TPB). 3) The oxygen ion is formed from the electron transfer and diffuses into the electrolyte, as shown in Figure 2-2 [10] .

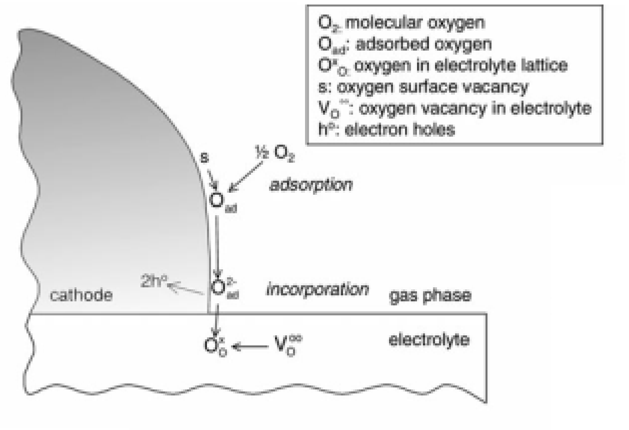

Figure 2-2 The ORR reaction [10].

The electrons in the external circuit stem from the oxidation reaction of hydrogen (Hydrogen Oxidation Reaction, HOR, Equation 2.2) (or carbon monoxide, or methane and other hydrogen-rich hydrocarbon gases) at the anode. Combining the previous two half-cell reactions into an overall reaction for the SOFCs results in the electrochemical reaction given by Equation 2.3. At the boundary between the electrolyte and anode, when hydrogen is utilised as fuel, the hydrogen atoms react with the oxygen ions which have passed through the electrolyte, forming water, and releasing electrons which are gathered into the external circuit.

$$O_2 + 4e^- \rightarrow 2O^{2-}$$ Equation 2.1

$$2H_2 + 2O^{2-} \rightarrow 4e^- + 2H_2O$$ Equation 2.2

$$2H_2 + O_2 \rightarrow 2H_2O$$ Equation 2.3

2.1.2 Geometry Design

Several types of SOFC have been thoroughly investigated over the past few decades with designs including planar [9, 35-37], tubular [38-40], and micro-tubular configurations [41-46].

An advantage of planar SOFCs is the ease in which they are stacked, since their electrodes are able to provide good conductivity. Kanzini and Leone [47] have suggested that anode supported planar cells could provide a better performance for internal reforming than the electrolyte supported ones, as they contain more catalyst (e.g. nickel) due to the thicker anode. Nevertheless, sealing problems, and long start up time are potential drawbacks of planar SOFCs. Differences in thermal expansion coefficients among cell materials limit the heating rate of the system.

The tubular design was invented by Westinghouse Electric Corporation, whilst Microtubular SOFCs (μSOFCs) were pioneered by Prof. Kevin Kendall in the 90's

[42, 48]. The former are usually larger than 15 mm in diameter and longer than 600 mm, whilst the latter usually have a diameter smaller than 15 mm with length between 50-100 mm [10, 42]. The microtubular design allows a shorter heating up time because the heat can be transferred fairly homogeneously and quickly inside the cell. Small ceramic are further more able to sustain large thermal gradients, both in space and time. However, the stacking and interconnection issues complicate stack designs for both tubular and μSOFCs.

μSOFC tubes from Adaptive Materials, Inc. was invested by many researchers [42, 45, 49, 50]. This anode supported cell has 2.3 mm inner diameter, and is 56 mm in length. As supplied, it is formed of a porous, 200 μm thick anode layer made of nickel-Yttria-Stabilized Zirconia (YSZ), surrounded by a 10 μm YSZ electrolyte, as shown in Figure 2-3. The cathode layer was applied by painting an in-house Lanthanum Strontium Manganite (LSM) ink onto the electrolyte layer, approximately 30 mm in length. The cell was sintered at 1373 K and then reduced by a constant flow of hydrogen under 973 K. The silver ink was painted onto the cathode in a three-band pattern. After the silver ink had dried, 70 cm of 99.99% silver wire was wound around the cathode to act as current collector. The final cell configuration is shown in Figure 2-4. These cells were also employed in the study of control system design (see appendix I).

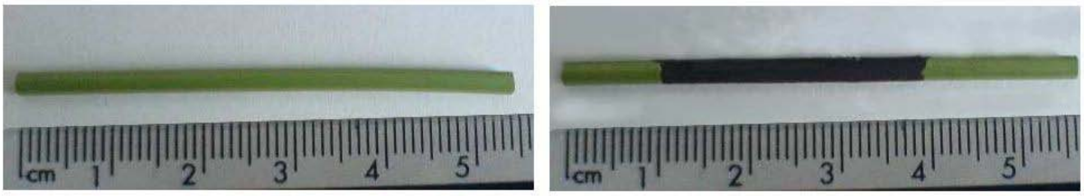

Figure 2-3 The μ-SOFC without (left) and with (right) the cathode layer reproduced from [42].

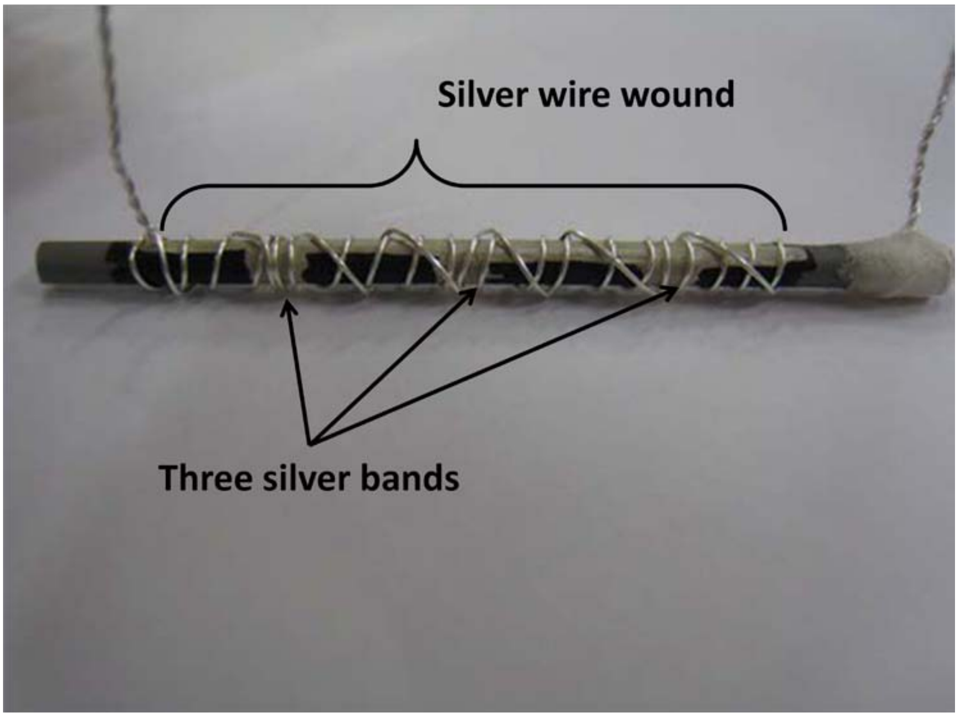

Figure 2-4 Silver ink bonds and wires wound on the μ-SOFC [29].

2.1.3 Current State of Modelling

The high efficiency and low emissions generated by fuel cells have spurred much research over the past few decades. However, considerable cost is incurred when making, or obtaining fuel cells for research purposes. Computational modelling can be used as a tool for testing fuel cell configurations at relatively low cost, although one must be careful that the model produces accurate results via experimental validation. Usually, a zero or one-dimensional (0- or 1-D) model focuses on the system level, with applications such as control systems since they can often be solved in real time. Higher dimensional models, such as 2- and 3-D, provide more detail about the single cell and stack [51]. Modelling both of SOFC and steam methane reforming system have been widely investigated over the past few decades.

SOFC modelling has been widely researched [38, 52-58] and some anode recirculation modelling work has been presented [5, 25, 26, 59-61]. However the relationships between recycling rate, fuel cell performance, and carbon formation have not yet been fully investigated. The strategy of anode off-gas recycling to prevent carbon formation was proposed by many researchers such as Shekhawat et al. [4] and Eveloy [62], but they failed to discuss the issue of overall efficiency decrease in the fuel cell.

Detailed reviews of modelling were also presented by Wang et al. [51] and other researchers [63, 64]. Wang et al. discussed the electrical circuit technique whilst the studies in [63, 64] focus on pure mathematical modelling.

2.2 Anode Function

Both fuel reforming and oxidation reactions occur in the anode and thus the anode material needs to meet four requirements: electronic conductivity, oxide ion conductivity, catalytic activity, and porosity. Platinum and gold were first tested in early SOFC development, then investigations into nickel and iron were also conducted [10] due to their high catalytic activity and electrical conductivity. The problem of nickel agglomeration under high temperature was solved by Spacil by adding Yttria-Stabilised-Zirconia and forming cermets [10]. This has become one of the most common materials for SOFC anodes in modern times.

The issue of carbon deposition on the anode surface was raised when hydrocarbon fuels were used instead of pure hydrogen, as the solid carbon can cover the porous cermet and deactivate the nickel catalyst. Specifically, nickel, as a catalyst for the breakdown of carbon-carbon bonds, also acts as a catalyst for the formation of carbon-carbon bonds, leading to coking [65, 66]. Additionally, nickel is also used as the current collector. A lower nickel concentration at the anode could lead to lower electrical conductivity [67]. Thus many materials have been investigated such as doped samaria [68, 69], cerium [70, 71], gadolinium [72, 73], ruthenium [66, 74], silver [75], and gold [76, 77] as replacement for or alloying agent with nickel in order to reduce the tendency to carbon formation without losing conductivity.

Today, nickel-oxide-YSZ is still a popular material for the SOFC anode because the nickel oxide used in manufacturing will be reduced to metallic nickel under typical anode operating conditions, and due to the reduction in volume from nickel oxide to metallic nickel, helps to form a porous anode which allows gas (e.g. hydrogen) to pass to the TPB whilst nickel also conducts the electrons to the external circuit. Nickel is also generally used as a catalyst in industry for hydrogen production from hydrocarbon reforming such as in steam methane reforming [78].

2.3 Methane / Natural Gas

2.3.1 Introduction

Methane is the main component of natural gas and the gas network infrastructure for this is well established. By using natural gas as the fuel for SOFCs, households can easily generate electricity and heat locally, avoiding grid transmission losses. However, since natural gas contains odorants based on sulphur and traces of hydrogen sulphide, this could poison the anode and reduce the nickel catalytic activity [33]. The poisoning mechanism can either be the adsorption of the sulphur atoms by the nickel, or the formation of nickel-sulphur compounds which decrease the hydrogen oxidation area [79]. The reactions can be distinguished into the adsorption, chemisorption and sulfidation, depending on the sulphur concentration, as listed in Equation 2.4 to Equation 2.7 [80].

$$\frac{n}{2}S_2 + mNi \leftrightarrow Ni_mS_n \qquad \text{Equation 2.4}$$

$$H_2S\ (g) \leftrightarrow HS(ads) + H({}^{g}/_{ads}) \leftrightarrow S(ads) + H_2({}^{g}/_{ads}) \qquad \text{Equation 2.5}$$

$$Ni + H_2S \leftrightarrow NiS + H_2 \qquad \text{Equation 2.6}$$

$$3Ni + xH_2S \leftrightarrow Ni_3S_x + xH_2 \qquad \text{Equation 2.7}$$

2.3.2 Methane Reforming

Methane can either directly be fully or partially oxidised electrochemically in an SOFC and produce electricity (Equation 2.8 and Equation 2.9), or it can be reformed internally at the anode, or externally reformed using additional reformers. Reforming still has many issues which need to be addressed. First of all, the use of an external reformer adds complexity to a system and so is often discouraged. Secondly, the reaction rate of the electrochemical oxidations of methane are much slower than the reforming ones [81]. Finally, SOFC high operating temperature can directly provide the energy required for endothermic reforming reactions and thus increase the overall efficiency. At the same time the heat transfer process reduces the need for stack cooling.

$$CH_4 + 2O_2 \leftrightarrow CO_2 + 2H_2O \quad \Delta H^0_{298} = -802\ \mathrm{kJ\ mol^{-1}}$$ Equation 2.8

$$CH_4 + \frac{1}{2}O_2 \leftrightarrow CO + 2H_2 \quad \Delta H^0_{298} = -36\ \mathrm{kJ\ mol^{-1}}$$ Equation 2.9

Steam Methane Reforming (SMR, Equation 2.10), Water Gas Shift (WGS, Equation 2.11) and Direct/Gradual Internal Reforming (DIR/GIR, also called reverse methanation reaction, Equation 2.12) are often focused upon when methane is mixed with steam [82].

$$CH_4 + H_2O \leftrightarrow CO + 3H_2 \quad \Delta H^0_{298} = +205\ \mathrm{kJ\ mol^{-1}}$$ Equation 2.10

$$CO + H_2O \leftrightarrow CO_2 + H_2 \quad \Delta H^0_{298} = -42\ \mathrm{kJ\ mol^{-1}}$$ Equation 2.11

$$CH_4 + 2H_2O \leftrightarrow CO_2 + 4H_2 \quad \Delta H^0_{298} = +163\ \mathrm{kJ\ mol^{-1}}$$ Equation 2.12

If the water is sufficient for SMR and WGS to occur simultaneously, then the SMR and WGS are combined and thus methane is converted with water into hydrogen and carbon dioxide. This is called DIR; otherwise, if the water is insufficient for both

SMR and WGS, then these two reactions will compete against each other to react with water. This leads to a two-stage reaction, which is called GIR. In the GIR system, methane is first converted through SMR into hydrogen and carbon monoxide. The hydrogen produced by this reaction is then oxidised at the SOFC anode, producing water which is then used for the WGS reaction that converts carbon monoxide into hydrogen and carbon dioxide. The mechanism is shown in Figure 2-5. Whilst it is possible that carbon monoxide can be electrochemically oxidised at the anode, Vernoux [82] suggested that the rate of the shift reaction is much faster than the rate of carbon monoxide oxidation, therefore consuming most of the carbon monoxide in the WGS.

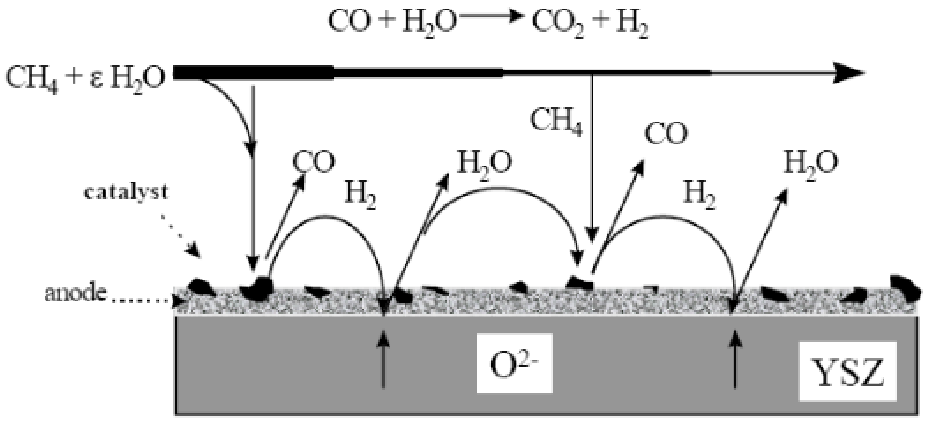

Figure 2-5 Steam methane reforming mechanism [82].

Methane can also be reformed by reacting with carbon dioxide through Dry methane

Reforming (DR, Equation 2.13). In the produced gas from the DR process, the hydrogen to carbon monoxide ratio (H_2/CO ratio) is around 2, which is favoured for the Fischer–Tropsch (F-T) synthesis [83, 84]. Literature shows the SMR has a higher conversion rate in methane than DR, because, unlike with the SMR in which the produced carbon monoxide can still react with water and form hydrogen, the hydrogen produced in the DR causes high hydrogen partial pressure which potentially leads to a reaction with carbon dioxide, forming carbon monoxide and water through the reverse WGS reaction [85].

$$\mathrm{CH_4 + CO_2 \leftrightarrow 2CO + 2H_2} \quad \Delta \mathrm{H}_{298}^{0} = +247\ \mathrm{kJ\ mol^{-1}} \qquad \text{Equation 2.13}$$

The water vapour or carbon dioxide required for methane reforming can be obtained from the anode exhaust gas since they are the products of hydrogen or carbon monoxide oxidation reactions.

2.3.3 Methane Reforming Kinetics

The dynamic modelling approach for methane reforming has been reported in literature [86]. At given operating conditions, the formula can determine the rate of the chemical reactions. As a result, the rates of species consumption and production can be worked out by using the stoichiometric technique in the kinetic modelling, for example, for every second, how many moles of methane are consumed and how many moles of hydrogen are produced. The produced and consumed gases are then added to the initial flow rate, thereby obtaining the gas composition and reforming performance.

SMR (Equation 2.10), WGS (Equation 2.11), and DIR (Equation 2.12) are discussed as the main reactions in steam methane reforming.

Iwai et al. [87] has suggested the reaction rates of SMR and WGS in an intermediate-temperature planar SOFCs, as listed in Equation 2.14 and Equation 2.15 with the units of mole m^{-3} s^{-1}, respectively. The cell has one fuel channel and three air channel, and the anode material Ni-YSZ cermet with a the dimension of 88 mm in length, 100 mm in width, and 0.8 mm in thickness. Additionally, the SMR reaction was assumed to occur on the anode surface only.

$$\mathrm{r_{SMR}} = 4274\left(1 - \frac{\mathrm{P_{co}P_{H_2}^3}}{\mathrm{P_{CH_4}P_{H_2O}K_{P,SMR}}}\right) \times \left(\frac{\mathrm{P_{CH_4}}}{100000}\right) exp\left(\frac{-82000}{RT}\right)$$

Equation 2.14

$$\mathrm{r_{WGS}} = \left(\frac{\varepsilon_{\mathrm{chan}}}{\varepsilon_{\mathrm{an}}}\right) k_{\mathrm{WGS}}\left(\mathrm{P_{H_2O}P_{CO}} - \frac{\mathrm{P_{H_2}P_{CO_2}}}{\mathrm{K_{P,WGS}}}\right)$$

Equation 2.15

Here ε_i (i = chan, an) represent the porosity of the fuel passing channel and the anode surface, and P_i (i = CO, H_2, CH_4, H_2O, CO_2) are the partial pressures of each gas. R is the gas constant, T is the temperature in Kelvin and K_i (i = SMR and WGS) is the equilibrium constant of each reaction. Another set of reaction rates related to the gas concentration, listed in Equation 2.16 and Equation 2.17 is proposed by both Klein et al. and Vakouftsi et al. [9, 88], where [i] is the concentration of each gas with the unit of kmol m^{-3} and T is the temperature in Kelvin.

$$\mathrm{r_{SMR}} = 63.6 \times \mathrm{T}^2 \times exp\left(\frac{-27063}{\mathrm{T}}\right)[\mathrm{CH_4}][\mathrm{H_2O}] - 3.7 \times 10^{-14} \times \mathrm{T}^4 \times exp\left(\frac{-232.78}{\mathrm{T}}\right)[\mathrm{CO}][\mathrm{H_2}]^3 \qquad \text{Equation 2.16}$$

$$\mathrm{r_{WGS}} = 1199 \times \mathrm{T}^2 \times exp\left(\frac{-12509}{\mathrm{T}}\right)[\mathrm{CO}][\mathrm{H_2O}] - 6.77 \times \mathrm{T}^4 \times 10^4 \times exp\left(\frac{-16909}{\mathrm{T}}\right)[\mathrm{CO_2}][\mathrm{H_2}] \qquad \text{Equation 2.17}$$

Methane dry reforming is another way of producing hydrogen from methane. Methane reacts with carbon dioxide and forms carbon monoxide and hydrogen, as shown in Equation 2.13.

One advantage of methane dry reforming is that the kinetic reaction is fast at typical

SOFC operating temperatures. However, as the DR is a strong endothermic reaction, it could also lead to a large temperature gradient during the internal reforming, and eventually to crack formation in the cell due to thermal stress [89].

Darujati et. al [90] reported on the kinetic aspects of methane dry reforming on ceria-based Mo_2C catalyst. The reaction rate related to the partial pressure is given in Equation 2.18.

$$\mathrm{r_{DR}} = 2.21 \times 10^{8} \times \left[exp\left(\frac{-45500}{1.987 \times \mathrm{T}}\right)\right] \times \mathrm{P_{CH_4}^{0.95}} \times \mathrm{P_{CO_2}^{-0.18}} \qquad \text{Equation 2.18}$$

Here T is the temperature in Kelvin and P_i (i= CH_4, CO_2) are the partial pressures of the two gases.

Goula [91] has investigated the cell performance running on methane internal dry reforming by feeding various ratios between methane and carbon dioxide. The results suggest that the Ni-YSZ SOFC anode can operate with a wide range of methane to carbon dioxide ratio for a long period as the risk of carbon formation can be avoided by the carbon electro-oxidation reactions, as listed in Equation 2.19 and Equation 2.20. A similar result is reported by Moon and Ryu [92]. Both reports address that the closed-circuit operation of SOFC has a better ability than the open-circuit status in preventing carbon deposition. This is because the oxygen from the air is introduced into the cell and consumes the hydrogen, carbon monoxide, methane and the formed solid carbon. This shifts the reaction and lowers the possibility of carbon formation.

$$\mathrm{C_{(s)} + O^{2-} \leftrightarrow CO + 2e^{-}} \qquad \text{Equation 2.19}$$

$$\mathrm{C_{(s)} + 2O^{2-} \leftrightarrow CO_2 + 4e^{-}} \qquad \text{Equation 2.20}$$

Wei and Iglesia [93] suggested that the SMR, DR, and the methane cracking reaction have a similar reaction rate when nickel is used for the reforming reactions. This is because the C-H bond dominates the forward reaction steps and the concentration of each gas has little effect on the reaction speed. Moreover, the three reactions have a similar activation energy in the backwards reaction.

2.3.4 Methane Reforming and the Equilibrium Constants

Several forms of equilibrium constants for methane reformation can be found in the literature. For example, for SMR, WGS and DR, the exponential form of K_P with the T is the temperature in Kelvin is used by Hou and Hughes [94], listed in Equation 2.21 to Equation 2.23.

$$\mathrm{K_{P,SMR}} = 1.198 \times 10^{17} \exp\left(-\frac{26830}{\mathrm{T}}\right) \qquad \text{Equation 2.21}$$

$$\mathrm{K_{P,WGS}} = 1.767 \times 10^{-2} \exp\left(\frac{4400}{\mathrm{T}}\right) \qquad \text{Equation 2.22}$$

$$\mathrm{K_{P,DR}} = 6.780 \times 10^{18} \exp\left(-\frac{31230}{\mathrm{T}}\right) \qquad \text{Equation 2.23}$$

On the other hand, the polynomial form of K_C for SMR and WGS, was introduced by Bossel, are found in [5, 95], given in Equation 2.24 and Table 2.1. The polynomial temperature-dependent equation for DR was derived from Hou's work. The coefficients for DR are also listed in Table 2.1. The comparison between the polynomial form and exponential form for SMR, WGS and DR are shown in Figure 2-6 to Figure 2-8. The valid temperature range is from 300 K to 1200 K.

$$\log \mathrm{K_C} = \mathrm{AT^4} + \mathrm{BT^3} + \mathrm{CT^2} + \mathrm{DT} + \mathrm{E} \qquad \text{Equation 2.24}$$

For the SMR reaction, a coefficient of $(RT)^{-\triangle n}$ is required for converting Hou's K_P into K_C and then comparing with Bossel's K_C. The term, $\triangle n$, is the change of the number of mole in the reaction. The logarithm values are shown in Figure 2-6. For WGS, since there is no change in the number of moles, the natural logarithm of equilibrium constants in this reaction are then directly shown in Figure 2-7. In Figure 2-8, the derived *ln(*K_C*)* is compared with the values from Hou's work to validate the DR equation in Equation 2.24.

Table 2.1 Coefficients for SMR, WGS and DR linearised equilibrium constants.

	SMR	WGS	DR
A	-2.6312×10^{-11}	5.4730×10^{-12}	-6.15×10^{-11}
B	1.2406×10^{-7}	-2.5748×10^{-8}	2.42×10^{-7}
C	-2.2523×10^{-4}	4.6374×10^{-5}	-3.7×10^{-4}
D	1.9502×10^{-1}	-3.9150×10^{-2}	2.72×10^{-1}
E	-66.1395	13.2097	-81.5

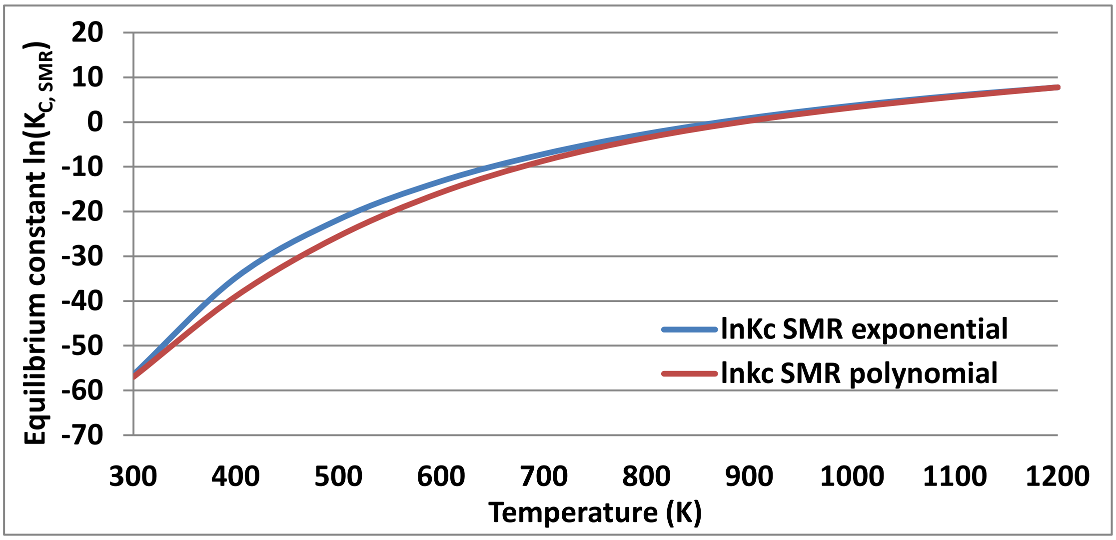

Figure 2-6 Natural logarithm of equilibrium constants for SMR from different methods.

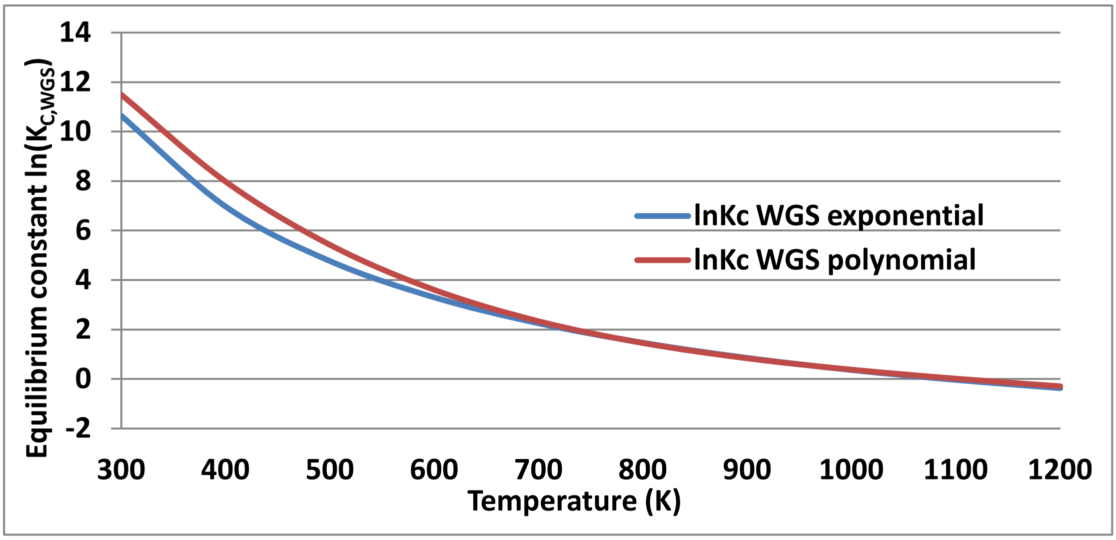

Figure 2-7 Natural logarithm of equilibrium constants for WGS from different methods.

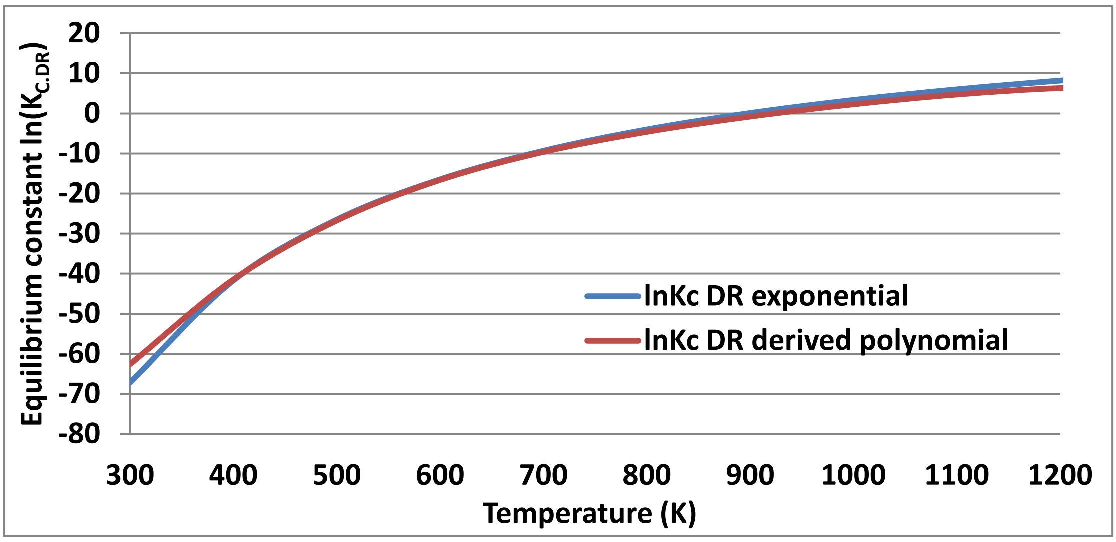

Figure 2-8 Natural logarithm of equilibrium constants for DR from different methods.

It can be seen from Figure 2-6 to Figure 2-8 that both SMR and DR are highly active at high temperatures (above 900 K), whilst WGS reaction prefers the mid to low temperature range. From the thermodynamic viewpoint, methane tends to be converted through SMR and DR into hydrogen rich gases at high temperatures.

2.4 Other Fuels

2.4.1 Ethanol

Ethanol can also be used as a fuel for SOFCs for a variety of reasons, including the issues that it is relative safety in handling and the number of hydrogen atoms it contains per molecule. In addition, it can be produced directly from biomass [96]. Ethanol steam reforming, both full and partial (Equation 2.25 and Equation 2.26), are the most common ways of producing hydrogen for SOFCs with nickel as the catalyst [97].

$$C_2H_5OH + 3H_2O \rightarrow 2CO_2 + 6H_2 \quad \text{Equation 2.25}$$

$$C_2H_5OH + H_2O \rightarrow 2CO + 4H_2 \quad \text{Equation 2.26}$$

Literature reports that the performance of a Ni/CeGd SOFC anode for ethanol steam reforming has a better conversion ability at 773 K by producing minimal by-products, however suffers the problem of carbon formation [98, 99]. The carbon formation is then decreased with increasing operating temperature since the Boudouard reaction is less active at high temperatures.

In 2005, a pure, undiluted ethanol-fed SOFC was presented by Franklin Fuel Cells ™ which can achieve 400 mW cm^{-2} for 100 hours operation. They were also aiming to achieve 50% efficiency in the 10-15 kW_{elec} applications [100].

2.4.2 Biogas

Biogas is produced through the process of anaerobic digestion of different organic wastes such as sewage, agricultural wastes, or even animal manure [101]. It mainly consists of methane and carbon dioxide with traces of hydrogen sulphide and ammonia [102]. As a result, biogas can be used as fuel because it can be directly converted into hydrogen through the dry reforming reaction (Equation 2.13). Another advantage of using biogas is that it reduces the emission of GHGs, such as carbon dioxide and methane. The methane is converted to hydrogen and carbon monoxide in place of acting as a greenhouse gas 20 times more active than carbon dioxide. The carbon dioxide produced comes from biological sources and closes the biological cycle instead of releasing carbon from fossil fuels underground, as shown in Figure 2-9 [103].

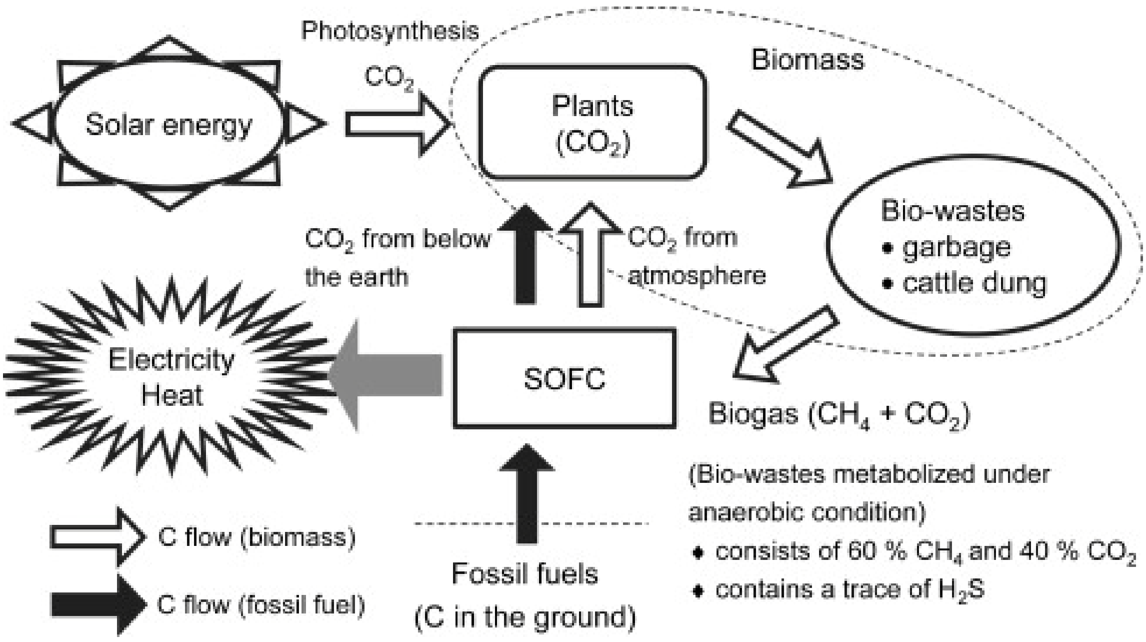

Figure 2-9 The use of biogas can reduce the emission of greenhouse gases [103].

Previous research also suggests that SOFCs can generate power under a very low methane concentration which ICEs would fail to ignite [104], providing better efficiency [103]. Lanzini and Leone [47] also pointed out that additional reactants (i.e. carbon dioxide and steam) were required to avoid carbon formation when bio-methane was used as fuel.

2.4.3 Syngas

Syngas is a mixture of hydrogen and carbon monoxide gas usually obtained from the gasification of coal, biomass, or heavier oils [105]. Among different types of gasifier, the fluidised bed reactor provides higher conversion rates [106]; moreover, the operating temperature and scale are similar to that of SOFCs [107]. However, a gas cleaner is often required to remove sulphur and some tar before being fed into the SOFC as they could poison the anode, causing anode degradation, and therefore decreasing the cell performance [108].

The modelling results by Aloui and Halouani [109] show that the 24%-carbon monoxide contained syngas fuelled SOFCs has a better electrical performance than the pure hydrogen scenario by about 23%. This is because carbon monoxide can be oxidised at high temperature (i.e. 1073 K) directly, instead of being a poison to SOFC as at lower temperatures. However, on the other hand, Li et al. [110] reported on using coal-based syngas fuelled SOFC with a nickel-aluminium oxide treated anode. The results showed that the maximum power density is 34% lower than the case when hydrogen is utilised as fuel at 1073 K. Hackett et al. [111] reported the degradation rate from their results of an SOFC using syngas from gasification as fuel. The degradation rate was around 10% at lower current densities and 17% at higher densities per 1000 hours of operation.

2.4.4 Propane and Butane

Liquid fuels have a higher energy density than gaseous fuels and, furthermore, they are easier to carry, making them more attractive for powering portable devices and vehicles. They are the dominant fuels for ICEs nowadays. Propane and butane are gaseous but can be stored in the liquid phase at room temperature at relatively low pressures. As a result, they are considered as liquid fuels here. However, more effort is needed for utilising these fuels to power SOFCs, as there are some drawbacks such as carbon deposition that need to be overcome.

A result of using Ni-Ru/GDC as the catalyst for propane reforming was reported by Modafferi et al.[74]. The report suggests that propane steam reforming and auto-thermal reforming have good propane conversion rates at temperatures above 973 K. For temperatures below 873 K, the steam reforming has the problem of carbon formation, whilst the latter case can significantly reduce this problem as the oxygen can remove the solid carbon at these temperatures.

A propane partial oxidation for producing hydrogen investigation was conducted by Zhan et al. [112]. Their modelling results suggest that with the ratio above 1.75 between oxygen and propane, and temperature higher than 1006 K, propane is partially oxidised and the system is free from carbon deposition. The results from their experiments showed that hydrogen is the main product, as opposed to the modelling results in which propane–air is used. At 1063 K, the cell generates around 700 mW cm^{-2} and can avoid carbon formation when a mixture of propane and air is used as the fuel.

Figure 2-10 The demonstration of a fan powered by a Butane fed single μ-tubular SOFC, reproduced from [49].

Figure 2-10 is a demonstration with a single μ-tubular SOFC from Adelan to power a small fan with Butane. At the exhaust of the fuel tank, there is a flame used to heat up a catalyst mesh, which reforms Butane through Catalytic Partial Oxidation (CPOx) before it is fed to the SOFC to generate electricity for the fan [49].

2.5 Carbon Formation

2.5.1 Langmuir-Hinshelwood-Hougen-Watson

Langmuir proposed a theory for a gaseous species adsorbed by a solid surface in 1918, which can be applied to methane reforming [113, 114]. In the reforming process, methane breaks down into solid carbon on the catalyst and gaseous hydrogen. The solid carbon is then removed by the oxygen atoms in the steam or carbon dioxide. The theory is based on some assumptions: 1) the adsorption only occurs on the top monolayer of the solid surface, 2) the surface is uniform in energy distribution and 3) the adsorbed species do not interact with others. The adsorption and desorption rates are given in Equation 2.27 and Equation 2.28.

$$\mathrm{r_{ads}} = \mathrm{k_{ads}} \times \mathrm{P_{ads}} \times (1 - \theta) \qquad \text{Equation 2.27}$$

$$\mathrm{r_{des}} = \mathrm{k_{des}} \times \theta \qquad \text{Equation 2.28}$$

Here $r_{,i}$ (i= ads, des) is the adsorption/desorption rate, P is the partial pressure of the adsorbed gas, θ is the covered surface which has adsorbed the gas and k is the adsorption/desorption constant. At equilibrium, the adsorption and desorption rates are equal, thus Equation 2.27 and Equation 2.28 are equal and can be combined as in the Langmuir absorption isotherm (Equation 2.29), where $\mathcal{F}$ is the ratio between k_{abs}

and k_{des}.

$$\theta_{\mathrm{eq}} = \frac{\mathcal{F} \times \mathrm{P_{abs}}}{1 + \mathcal{F} \times \mathrm{p_{abs}}} \quad \text{Equation 2.29}$$

The Langmuir theory can be used to describe the reaction when one molecule is absorbed by the surface. For a system with bimolecular adsorption and desorption, the Langmuir-Hinshelwood, or Eley-Rideal mechanism is required for explanation. The difference between these two mechanisms is that in the former case, both atoms are absorbed and form new products on the surface, as shown in Figure 2-11. In the latter case, only one atom is absorbed by the surface and then reacts directly with the other gaseous atom to form the product, shown in Figure 2-12. The Langmuir-Hinshelwood kinetics focus on the absorption and reaction step. It requires the Hougen-Watson theory to determine the rate-controlling step and to realise the whole reaction process.

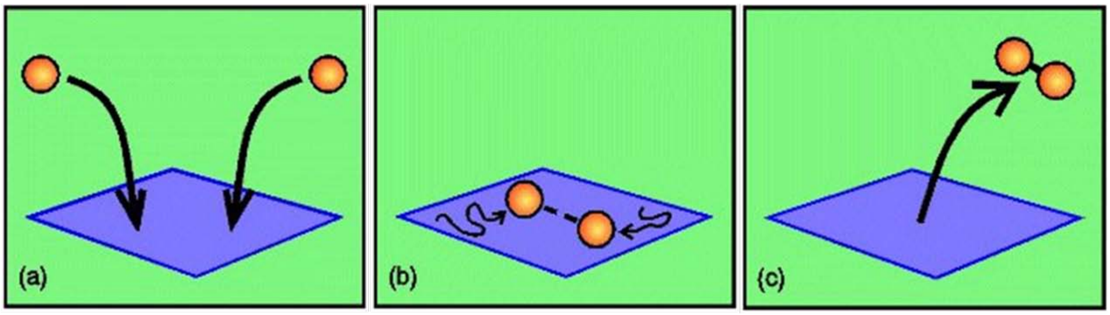

Figure 2-11 The Langmuir-Hinshelwood mechanism [115].

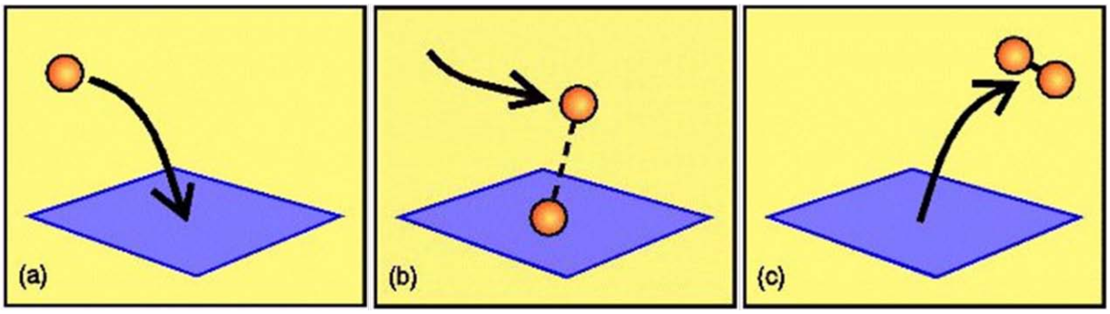

Figure 2-12 The Eley-Rideal mechanism [115].

The Hougen-waston formula was proposed in 1943 for the purpose of determining the reaction controlling rate of any heterogeneous reaction [116]. Because the heterogeneous reactions have many steps and contain various mechanisms that could affect each other, this theory suggests that the reaction rate can be determined by either of the three groups: 1) the kinetic group, 2) the driving-force group, and 3) the adsorption group. The formula is given in Equation 2.30 [116, 117]

$$\mathrm{r} = \frac{(\text{kinetic group})(\text{driving force group})}{\text{adsorption group}} \qquad \text{Equation 2.30}$$

Here, the kinetic group contains the rate coefficient and the ratio between the adsorption and desorption rate of every species. The driving-force group is related to the reaction progress and the equilibrium state. The adsorption group represents the coverage of the surface with respect to each species.

2.5.2 Carbon Formation inside Fuel Cells

Solid carbon formed inside SOFCs during the methane internal reforming can cover the porous anode structure and deactivate the nickel catalyst when hydrocarbon is used as fuel. This is shown in Figure 2-13. This can lead to significant damages to the cell because the covered nickel no longer reforms the fuel, and the porous structure for gases to travel through is blocked. Moreover, unlike other impurities such as sulphur or tar, carbon exists in all hydrocarbon fuels and cannot be removed by any pre-treatment aside from external reforming. Thus, well-designed operating conditions for SOFCs running on hydrocarbons are necessary to avoid the formation of solid carbon inside the cell.

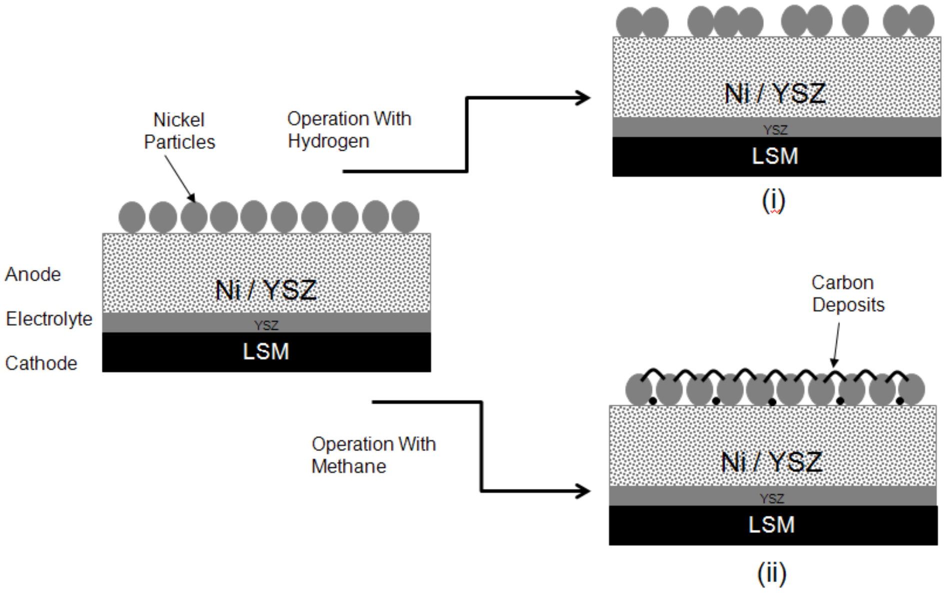

Figure 2-13 Difference between SOFCs running on hydrogen and methane [118].

2.5.3 Reactions Related to Carbon Formation

Solid carbon deposition can be a serious problem for SOFCs as the carbon can aggregate on the nickel particles used as the catalyst for fuel reforming within the anode, thus lowering the reforming ability. Moreover, the porous anode structure may also be blocked by solid carbon, and thus results in poor performance, or even cell failure. Carbon deposition can be caused by several reactions such as Methane Cracking (MC, Equation 2.31), Boudouoard reaction (BD, Equation 2.32) and Reversed Syngas Formation (RSF, Equation 2.33) as listed [119],

$$\mathrm{CH_4} \leftrightarrow \mathrm{2H_2} + \mathrm{C} \;\; \Delta \mathrm{H}^0_{298} = +75 \text{ kJ mol}^{-1} \qquad \text{Equation 2.31}$$

$$\mathrm{2CO} \leftrightarrow \mathrm{CO_2} + \mathrm{C} \;\; \Delta \mathrm{H}^0_{298} = -172 \text{ kJ mol}^{-1} \qquad \text{Equation 2.32}$$

$$\mathrm{CO} + \mathrm{H_2} \leftrightarrow \mathrm{H_2O} + \mathrm{C} \;\; \Delta \mathrm{H}^0_{298} = -131 \text{ kJ mol}^{-1} \qquad \text{Equation 2.33}$$

Armor and Haag et al. [120, 121] suggested that MC and BD are two major pathways for carbon formation. The backwards direction of Equation 2.33 is known as the Syngas Formation (SF) reaction. The natural logarithm equilibrium constants for the MC, BD and RSF reactions from different references are shown in Figure 2-14. The linearised temperature-dependent formula can be obtained from literature [94].

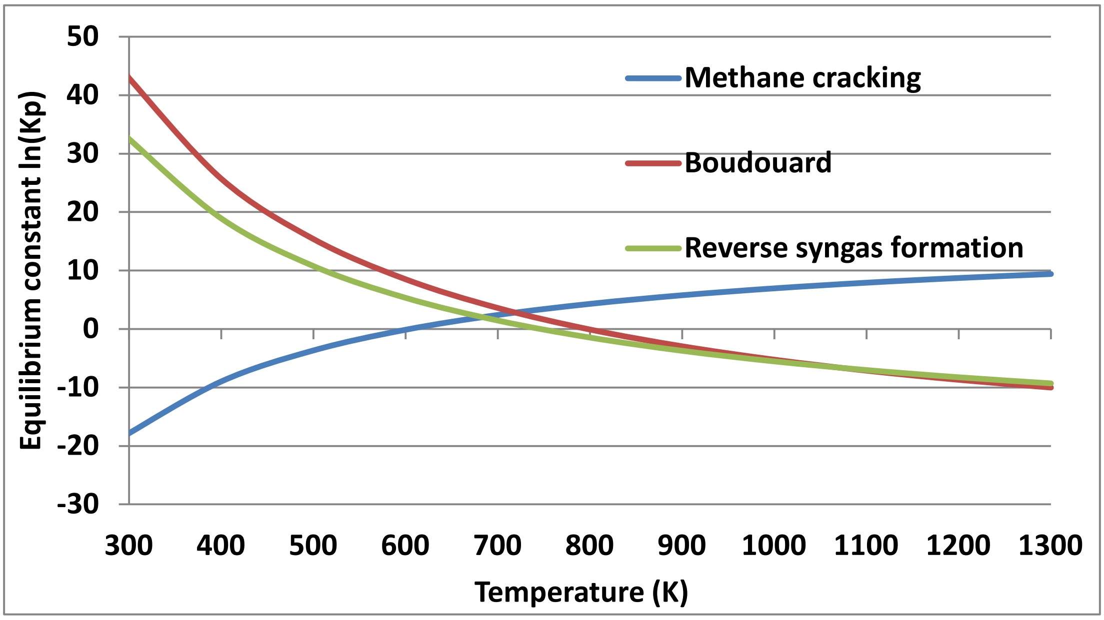

Figure 2-14 Natural logarithm of equilibrium constants for methane cracking, Boudouard and reverse syngas formation reactions.

From Figure 2-14, it can be seen that the values of methane cracking equilibrium constant is increasing with temperature increases whilst the Boudouard and RSF are decreasing. This suggests that the MC reaction is a high temperature favoured reaction, which becomes more active at higher temperatures. On the other hand, both Boudouard and RSF are less active within the same temperature range. However, SOFCs' typical operating temperature is above 800 K, and thus MC reaction is the main source of solid carbon.

2.5.4 Carbon Formation Restriction

Many investigations have been conducted into the prevention of carbon formation from both the kinetic [119, 122] and the thermodynamic equilibrium [62, 121, 123] viewpoints. A common way is to decrease the concentration of carbon sources. As discussed previously, the carbon formed through MC, BD and RSF reactions are sourced from methane or carbon monoxide. The theory is to increase the reactants, such as water and carbon dioxide that are expected to improve reforming reactions, thus lowering the possibility of carbon formation. Because these species shift the reaction directions away from the carbon formation conditions, the system is protected from carbon formation. On the other hand, a large amount of non-fuel gases decreases the fuel concentration within the SOFC and lowers the cell voltage, according to the Nernst equation. As a result, the amount of non-fuel gases requires a detailed calculation.

Figure 2-15 is the C-H-O equilibrium diagram at different temperatures. On the lines, the ratio between two atoms are marked to present the compositions of the reactant gas. For example, methane, consisting of one carbon and four hydrogen atoms, is labelled at the 0.2 mark between the angle of C and H. Similarly, carbon dioxide and water are labelled at the 0.67 mark the carbon and oxygen angle as well as the oxygen and hydrogen angle, respectively. Several lines representing different temperatures within the triangle clearly mark the thresholds of carbon formation at equilibrium.

Within the figure, the gray triangle represents the mixture of methane, carbon dioxide and water. The system will be free of carbon formation if the C-H-O ratio is below the operating temperature line; otherwise, the system could suffer from the formation of soot. However, the definition of "carbon formation" is not "absolutely no carbon formation"; if the carbon formed is less than 1 Parts Per Million (ppm) in quantity, this can be regarded as a trace amount and ignored.

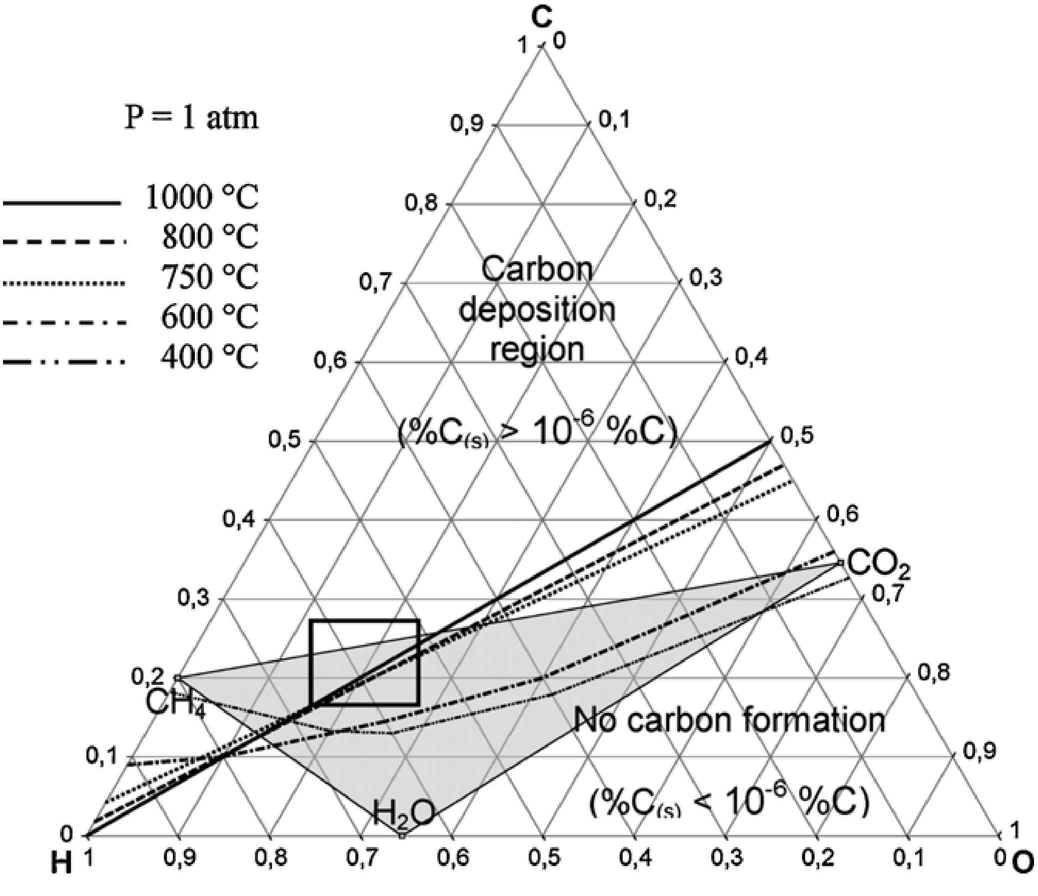

Figure 2-15 Carbon formation limitation diagram (% of the carbon atom present in the fuel) [124].

2.6 State-of-the-Art

2.6.1 Methane Reforming

Methane steam and dry reforming are two major ways for converting methane into hydrogen rich gas in industry. The advantage of steam methane reforming is that it provides a higher hydrogen yield than dry reforming. However the additional steam and the exposure to the high temperature could lead to corrosion of the nickel. Dry reforming, on the other hand, uses carbon dioxide in the reaction but results in a relatively low hydrogen yield. Moreover, both reforming reactions are strongly endothermic. This lowers the overall efficiency and could cause a large temperature gradient when internal reforming is applied, leading to cracked cells [125].

Practical experimental work of combined steam and dry methane reforming was reported by Al-Nakoua et al. [126], Maestri et al. [127] and Soria et al. [66]. Al-Nakoua has reported the combined SMR and DR in a narrow channel, but failed to address how the ratios among the fuel gases affect the conversion reactions; instead, it was focused on how the pressure affects the reforming reaction was focused. The reports from Maestri and Soria focus on the catalyst utilised in the reforming process. Rhodium was the material investigated by Maestri, whilst Soria focused on ruthenium with the explanations from the kinetic viewpoint. Soria suggested that in a system that contains steam, carbon dioxide and methane, the reforming reactions can be significantly affected by the steam concentration within the system. Özkara-Aydınoğlu [128] calculated the results of the combined steam and dry reforming of methane at different pressure by using the thermodynamic equilibrium. The results showed that the additional steam can increase the methane conversion significantly when the reaction temperature is lower than 1073 K, and for higher temperatures, methane can be almost entirely converted by both DR and SMR. Majewski and Wood [84] have conducted methane tri-reforming, which includes SMR, DR and partial oxidation by utilising nickel silica as the catalyst. The experimental results showed that the methane conversion can be improved by additional oxygen, whilst the effect on the hydrogen to carbon monoxide ratio in the produced syngas is insignificant. Additionally, they also suggest that the nickel-silica based catalyst can potentially be very suitable for the methane tri-reforming due to its high methane conversion rate and low tendency to carbon formation.

2.6.2 Carbon Deposition

A thermodynamic approach for investigating dry methane reforming and carbon formation was reported by Nikoo and Amin [129]. Meanwhile, two methods for modelling methane steam reforming and carbon deposition based on thermodynamic equilibrium are reported in [119, 130, 131].

The first method is to take the MC, BD and RSF reactions into consideration directly. The ratio between methane and water is critical for carbon formation, as shown in Figure 4-1. The second method is to determine the equilibrium composition of each species involved in the steam methane reforming reactions through the equilibrium constants. Different ratios of steam to methane were given as initial values. The composition of all species in the system can then be obtained by using their equilibrium constants at different temperatures. The concentrations of each composition were calculated for a particular temperature and then were used in the carbon activity (α) to determine the possibility of carbon formation caused by MC, BD, and RSF reactions [119]. Both methods will be presented and discussed in Chapter 4.

2.6.3 System

The use of anode off-gas recirculation for improving methane internal reforming in SOFC was reported by Lee [25], but that work mainly focused on the methane conversion and failed to discuss carbon formation or dry reforming. Shekhawat et al. [4] reported the fuel cell anode recycle for fuel reforming and did not discuss the cell performance. A system scale modelling consisting of SOFC, steam methane reforming and anode recirculation systems was reported by Colpan et. al [58]. By using thermodynamic equilibrium, the study shows that the anode recycling rate with the cell output current can have a significant effect on the cell performance, especially at high current densities; however, this work fails to discuss the effect of carbon dioxide, as carbon dioxide can be utilised for DR and is also the product of carbon monoxide reduction. The authors, though, assume that hydrogen is the only fuel oxidised in the SOFC. Moreover, this work did not take the carbon formation into account. Massardo and Lubelli [95] reported modelling results of the combined SOFC and gas turbine system for anode recirculation, but carbon deposition was again not included. Zhu et al. [59] designed a fuel injector for the anode recirculation SOFC system. A report discussing an SOFC with anode recirculation running on propane is presented by Dietrich et al. [26]. A modelling work for controlling the injector for SOFC recirculation was achieved by Zhu [60]. Cheddie and Murray [61] have developed the modelling for investigating an SOFC with gas turbine using anode recirculation. A modelling work focused on the mass and heat transfer inside the cell was reported by Ackman [132].

The SOFC concept has been investigated from many different aspects, from materials issues to system architecture, from electrochemical and thermodynamic analysis of methane reformation to fuel cell operation status, and beyond, to the mechanism of carbon formation and the best way of removing any soot formed. However, the strategy of using the recycled anode off-gas to prevent carbon formation from methane internal reforming is rarely investigated when the fuel cell is in operation. The composition of the anode off-gas is directly affected by the fuel cell operating status, thus needs to be included in the analysis for further consideration. In the following chapter, a further discussion towards the theories used in this work will be presented.

Chapter 3 Model Development and Experimental Setup

3.1 Introduction

The aim of this thesis is to find the optimised anode off-gas recirculation rate to prevent carbon formation inside SOFCs, from both thermodynamic and kinetic modelling approaches and practical experiments. This chapter discusses the mathematical model for a whole system, including, the methane reforming unit, an SOFC cell, a performance monitor, carbon deposition, and fuel stream recycling. Then, the experimental setup for validating the combined steam and dry reforming of methane is introduced.

A brief introduction to thermodynamic theories is presented in section 3.2, followed by the theories for building SOFC models introduced in section 3.3. Section 3.4 presents the methane reforming model. Then, the carbon activity for the determination of carbon formation is discussed in section 3.5, with the system monitoring model presented in section 3.6. Finally, section 3.7 presents the experimental setup for the combined steam and dry reforming of methane.

3.2 Thermodynamics

As an electrochemical device, SOFCs convert energy from fuel gas/liquid to electricity and heat. As a result, they can be discussed from a thermodynamic viewpoint, because the power is released from reactions, and the composition at equilibrium status can be determined from the enthalpy and the change of Gibbs free energy. Additionally, the equilibrium constant approach provides a general framework since it discusses all reactions simultaneously. By using the laws of thermodynamics, this static modelling gives the boundary of the system, which is difficult for the dynamic modelling approach as it considers the system from a general aspect (i.e. from the Gibbs free energy of all species, whilst the kinetic one considers the reactions assumed in the system model).

3.2.1 Gibbs Free Energy

According to the second law of Thermodynamics, the change of Gibbs free energy ΔG is equal to the enthalpy ΔH minus the product of temperature T and the change of entropy ΔS:

$$\Delta G = \Delta H - T\Delta S = [\Delta U + \Delta(Pv)] - T\Delta S$$

Equation 3.1

$$= [\Delta q_{res} + \Delta w_{res}] + \Delta(Pv) - T\Delta S$$

Here, v is the volume, and U is the internal energy. The term ΔPv represents the change of the pressure or volume in the sysetm. At steady state, the reversible heat Δq_{res} is equal to $T\Delta S$, reversible work Δw_{res} equals zero, and the volume remains constant so that Equation 3.1 can be rewritten as Equation 3.2. By introducing the Van't Hoff isotherm equation into Equation 3.1, Equation 3.3 is obtained. Combining this with Equation 3.2 leads to Equation 3.4.

$$\Delta G = v\Delta P = \left(\frac{nRT}{P}\right)\Delta P = nRT\left(\frac{\Delta P}{P}\right)$$ Equation 3.2

$$\Delta G = \Delta G^0 + nRT \ln Q$$ Equation 3.3

Here, ΔG^0 is standard the Gibbs energy change for each reaction and can be calculated at 298 K and 1 atm. At equilibrium, ΔG is zero and the reaction quotient, Q, is equal to the equilibrium constant, K_C.

$$\Delta G^0 = -RT \ln K_c$$ Equation 3.4

In order to calculate the change of Gibbs free energy (*ΔG*), the enthalpy (*H*) and entropy (*S*) of the reactants as well as products are required at different temperatures. They have been linearised in Equation 3.5 to Equation 3.16.

$$\mathrm{H_{H_2}} = 29.44 \times \mathrm{T} - 8703.8 \qquad \text{Equation 3.5}$$

$$\mathrm{H_{H_2O}} = 37.36 \times \mathrm{T} - 252907 \qquad \text{Equation 3.6}$$

$$\mathrm{H_{O_2}} = 32.346 \times \mathrm{T} - 9553.5 \qquad \text{Equation 3.7}$$

$$\mathrm{H_{CH_4}} = 49.598 \times \mathrm{T} - 89513 \qquad \text{Equation 3.8}$$

$$\mathrm{H_{CO}} = 31.068 \times \mathrm{T} - 119778 \qquad \text{Equation 3.9}$$

$$\mathrm{H_{CO_2}} = 46.634 \times \mathrm{T} - 406637 \qquad \text{Equation 3.10}$$

$$\mathrm{S_{H_2}} = 27.887 \times \ln \mathrm{T} - 33.432 \qquad \text{Equation 3.11}$$

$$\mathrm{S_{H_2O}} = 35.697 \times \ln \mathrm{T} - 14.026 \qquad \text{Equation 3.12}$$

$$\mathrm{S_{O_2}} = 35.128 \times \ln \mathrm{T} + 28.294 \qquad \text{Equation 3.13}$$

$$\mathrm{S_{CH_4}} = 42.657 \times \ln \mathrm{T} - 53.578 \qquad \text{Equation 3.14}$$

$$\mathrm{S_{CO}} = 30.895 \times \ln \mathrm{T} + 21.228 \qquad \text{Equation 3.15}$$

$$\mathrm{S_{CO_2}} = 42.227 \times \ln \mathrm{T} - 23.668 \qquad \text{Equation 3.16}$$

Here, S_i, H_i (i= CH_4, CO, CO_2, H_2, O_2, H_2O) are the entropy and enthalpy of each species. These linearised equations allow the model to calculate the change of Gibbs free energy; thus the energy released from each reaction can be obtained from Equation 3.17. The change of the Gibbs free energies of hydrogen oxidation, carbon monoxide oxidation, methane partial oxidation and methane full oxidation are shown in Figure 3-1.

$$\begin{aligned}\Delta G &= \Delta H - T\Delta S \\ &= \left(H_{product} - H_{reactant}\right) - T\left(S_{product} - S_{reactant}\right)\end{aligned}$$

Equation 3.17

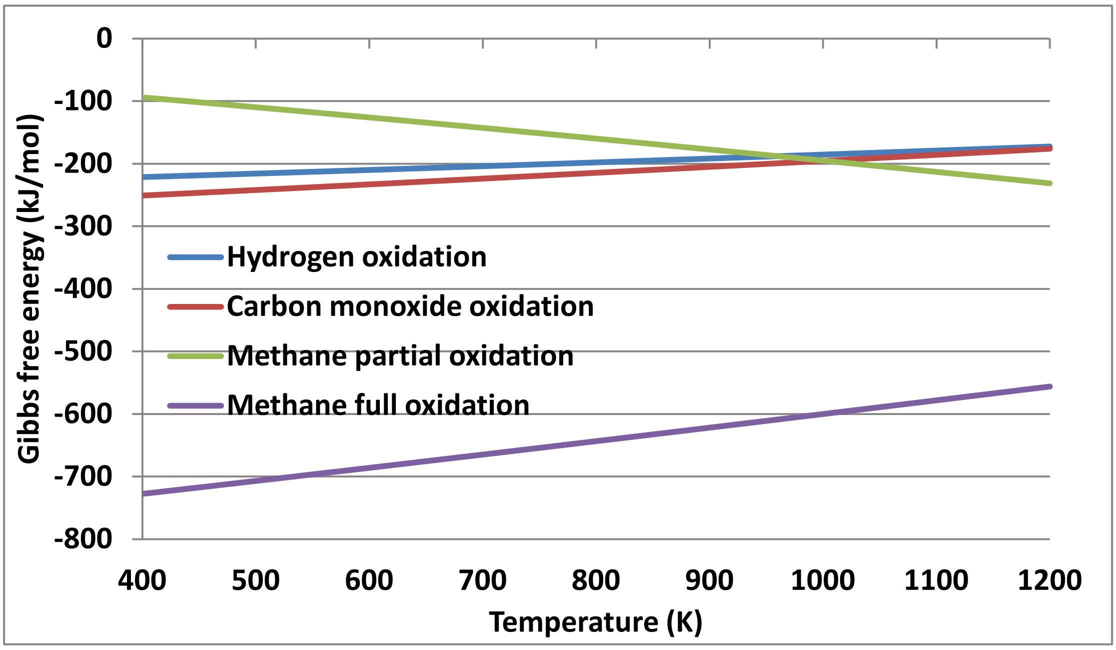

Figure 3-1 The Gibbs free energy of different reactions.

It can be seen from Figure 3-1 that all oxidation reactions release energy as the Gibbs free energy are all negative. However, when the temperature is below 373 K, water is in liquid form and thus has different thermodynamic values. This increases the complexity of linearising the formula. As a result, the values shown are from 400 K. Additionally, methane full oxidation is expected to provide more energy than any of the other three reactions. The released energy is decreasing with the temperature increasing in hydrogen, carbon monoxide and methane full oxidation reactions. As a result, from the three reactions, a relative low Nernst voltage is obtained at a relatively higher temperature.

3.2.2 Thermodynamic and Equilibrium Constants

The relationship between the change of Gibbs free energy and the equilibrium constants can be derived from Equation 3.4, written in Equation 3.18.

$$\ln \mathrm{K_c} = \frac{-\Delta \mathrm{G}}{\mathrm{RT}} \qquad \text{Equation 3.18}$$

The equilibrium constants K_C are based on the concentration of the reactants and products. For gas phase reactions, the constant can be written in the partial pressure form, K_P. The relationship between $\mathrm{K_C}$ and $\mathrm{K_P}$ can be determined as follows,

$$K_P = K_C(RT)^{\Delta n}$$ Equation 3.19

Here, Δn is the sum of the moles produced minus the sum of the moles of reactants. R is the gas constant with the value of 0.08205746 L atm K^{-1} mol^{-1}. Due to the different units of pressure used in the different constants, a factor of 100 is needed for converting between bar and kPa when K_P is used for calculation, as in Equation 3.20.

$$\text{kp (bar)} = \text{kp (kPa)} \times (100)^{\Delta n}$$ Equation 3.20

3.3 Solid Oxide Fuel Cell Model

In the model described in this section, hydrogen and carbon monoxide are assumed to react directly in the SOFC and generate electricity through hydrogen oxidation reaction (HOR, Equation 3.21) and carbon monoxide oxidation reaction (COx, Equation 3.22). Methane, on the other hand, can also theoretically react within an SOFC through the full or partial oxidation (FOx: Equation 3.23 and POx: Equation 3.24) and generate electricity [50]. However, the reaction rate of SMR (Equation 2.10) and WGS (Equation 2.11) reactions are much faster than the methane oxidation reaction [1, 133]. Thus, hydrogen and carbon monoxide are the only two gases assumed to be oxidised in the model.

$$\mathrm{H_2 + \frac{1}{2}O_2 \leftrightarrow H_2O}$$ Equation 3.21

$$\mathrm{CO + \frac{1}{2}O_2 \leftrightarrow CO_2}$$ Equation 3.22

$$\mathrm{CH_4 + 2O_2 \leftrightarrow CO_2 + 2H_2O}$$ Equation 3.23

$$\mathrm{CH_4 + \frac{1}{2}O_2 \leftrightarrow CO + 2H_2}$$ Equation 3.24

3.3.1 Nernst Equation

The cell potential (E) of the oxidation-reduction reaction is caused by the change of Gibbs free energy of the elements in the specific reactions. The Nernst equation describes the relationship,

$$\mathrm{E} = \mathrm{E_0} - \frac{\mathrm{BT}}{\mathrm{Ne}} \ln \frac{a_{\mathrm{red}}}{a_{\mathrm{ox}}}$$ Equation 3.25

Here, *E* is the potential in voltage, *B* is the Boltzmann constant, *T* is the temperature in Kelvin, *e* is the electron charge, *N* is the electron transfer number and a is the chemical activity of reduction and oxidation. Because

$$\frac{\mathrm{BT}}{\mathrm{e}} = \frac{\mathrm{RT}}{\mathrm{F}}$$ Equation 3.26

Equation 3.25 then can be rewritten as Equation 3.27,

$$\mathrm{E} = \mathrm{E_0} - \frac{\mathrm{RT}}{\mathrm{NF}} \ln \frac{a_{\mathrm{red}}}{a_{\mathrm{ox}}} = \mathrm{E_0} - \frac{\mathrm{RT}}{\mathrm{NF}} \ln \mathrm{Q} \qquad \text{Equation 3.27}$$

Here, Q is the reaction quotient. At equilibrium, Q is equal to K_c and E is equal to 0, leading to Equation 3.28.

$$\mathrm{NFE_0} = \mathrm{RT} \ln \mathrm{K_c} \qquad \text{Equation 3.28}$$

Combining Equation 3.4, Equation 3.27 and Equation 3.28, the cell potential E can be obtained as following,

$$\mathrm{E} = \frac{-\Delta \mathrm{G}}{\mathrm{NF}} + \frac{\mathrm{RT}}{\mathrm{NF}} \ln(\mathrm{Q}) \qquad \text{Equation 3.29}$$

For the Nernst voltage from hydrogen oxidation at equilibrium state, the value is around 1.14 V at 400 K, and decreasing with temperature increasing, as from Figure 3-1. The Nernst voltage is only 0.96 V at 1000 K.

3.3.2 Open Circuit Voltage

The cell potential can be calculated from substituting from the Nernst equation into Equation 3.30 and Equation 3.31, depending on the fuel used.

$$E = \frac{-\Delta G}{NF} + \frac{RT}{NF} \ln\left(\frac{\sqrt{P_{O_2}} \times P_{H_2}}{P_{H_2O}}\right) \qquad \text{Equation 3.30}$$

$$E = \frac{-\Delta G}{NF} + \frac{RT}{NF} \ln\left(\frac{\sqrt{P_{O_2}} \times P_{CO}}{P_{CO_2}}\right) \qquad \text{Equation 3.31}$$

From Equation 3.30 and Equation 3.31, it can be seen that the cell voltage is affected by the partial pressure of both reactants and products, and temperature. When the system reaches equilibrium, the natural logarithm turn becomes zero so the voltage only depends on the change of Gibbs free energy.

The electrochemical oxidation of carbon monoxide is rarely investigated, Inui et. al [35] suggested that the oxidation ratio between carbon monoxide and hydrogen is unknown thus they assumed only hydrogen can be oxidised. Ni et al. [134] also pointed out that the carbon monoxide oxidation rate is much slower than the WGS reaction. Matsuzaki and Yasuda [135] agree this point, and even suggest that the oxidation of carbon monoxide is also slower than the hydrogen oxidation by 2-3 times. As a result, it can theoretically therefore be ignored in cell voltage calculations.

However, hydrogen and carbon monoxide are still assumed to be the fuel in this work, as a preparation for modelling the SOFCs running on carbon monoxide.

In order to work out the cell output voltage when multiple fuels are fed into a fuel cell, a mathematical iterative method was employed to calculate the internal resistance and current contributed by different fuels which results in the same terminal voltage [87]. Aloui and Halouani [109] use an appropriate coefficient to work out the cell voltage. In this work, the fuel cell voltage will be calculated based on the fuel molecular ratio, as given in Equation 3.32.

$$\mathrm{V_{cell}} = \mathrm{V_{H_2}} \times \frac{\mathrm{n_{H_2}}}{\mathrm{n_{total}}} + \mathrm{V_{CO}} \times \frac{\mathrm{n_{CO}}}{\mathrm{n_{total}}} \qquad \text{Equation 3.32}$$

The actual fuel cell voltage V_{cell} is defined to be the reversible voltage, E, minus the activation, ohmic, and concentration losses inside the cell, as shown in Equation 3.33.

$$V_{cell} = E - V_{act} - V_{ohm} - V_{con} \qquad \text{Equation 3.33}$$

E is the cell potential source from the change of Gibbs free energy (ΔG) in the chemical reactions, V_{act}, V_{ohm} and V_{con} are the activation, ohmic and concentration losses of the cell.

3.3.3 Activation Losses

Activation losses are introduced by the energy required to initiate the electrode reactions in an SOFC [25, 136] and come from both the anode and cathode side. At cathode side, it is the energy required for oxygen to transform into the oxygen ion. The overall activation loss for different fuels are given in Equation 3.34

$$\begin{aligned} V_{act} = \frac{2RT}{NF}\sinh^{-1}\left(\frac{j_i}{2 \times j_{o,an}}\right) \\ + \frac{2RT}{NF}\sinh^{-1}\left(\frac{j}{2 \times j_{o,ca}}\right) \end{aligned}$$

Equation 3.34

Here, R, T, N and F are the universal gas constant, temperature in Kelvin, electron transfer number, and the Faraday constant, respectively. The term j is the current density, j_i (i = H_2 or CO) represents the current density contributed by hydrogen or carbon monoxide; $j_{o,i}$ (i = an, ca) are the anode and cathode exchange current density limits. The current density limits are a temperature dependent function which are given in Equation 3.35 and Equation 3.36. For the anode, the coefficients $\mathcal{A}_i$ and $\mathcal{B}_i$ (i = an) are 1.2903×10^{7} and 151532, whilst for the cathode (i = ca), they are 3.9255×10^{6} and 149395, respectively [25].

$$j_{o,an} = \mathcal{A}_{an} \times \exp^{\left(-\frac{\mathcal{B}an}{RT}\right)}$$ Equation 3.35

$$j_{o,ca} = \mathcal{A}_{ca} \times \exp^{\left(-\frac{\mathcal{B}_{ca}}{RT}\right)}$$ Equation 3.36

Different electron transfer numbers, *N*, are caused by the oxidation reactions of different fuels. For hydrogen and carbon oxidation, the value is 2. Methane, although its oxidation reaction rate is much slower than the reforming reactions, can theoretically be fully or partially oxidised, giving the number of 2, 4 or 8.

3.3.4 Ohmic Losses

Ohmic losses are caused by the resistance to the ions travelling through the different fuel cell layers and follows the rule of Ohm. The resistance is propositional to the length of its passage which is shown in Equation 3.37, where ρ is the resistivity with units of ohm per meter and l is the thickness of the respective layer in meters.

$$V_{ohm} = (\rho_{an} l_{an} + \rho_{el} l_{el} + \rho_{ca} l_{ca}) \times j$$ Equation 3.37

In the model, the anode, electrolyte and cathode resistivity were set to be 0.01, 5000 and 1 Ω m^{-1}, based on literature [10]. Nickel-YSZ, YSZ and LSM is generally used as the anode, electrolyte and cathode with thicknesses of 200, 60 and 300 μm respectively, based on practical experience. Since the resistivity also depends on the cross-section of the current flow path, it depends on the size of the fuel cell.

3.3.5 Concentration Losses

The concentration loss is due to imbalance of reactant and reaction product concentration under higher current density operation [36, 137]:

$$\mathrm{V_{con}} = \frac{-\mathrm{RT}}{\mathrm{NF}} \ln\left(1 - \frac{\mathrm{j}}{\mathrm{j_L}}\right) \qquad \text{Equation 3.38}$$

Here R, T, N and F are the universe gas constant, temperature in Kelvin, electron transfer number and Faraday constant, respectively. The term j_L is the limiting current density which represents the maximum current density the SOFC can deliver. This depends on the fuel concentration at reaction site. The concentration of fuel decreases with the output current increases, and the limiting current is the output current that leads to zero concentration of reactants. A value of 400 A m^{-2} is suggested by Roberts [137] whereas Kang et al [36] suggested 12000 A m^{-2}, depending on the SOFC properties. The assumption of 20000 A m^{-2} (equal to 2 A cm^{-2}) was used in this model, because the value can be reached by good quality SOFC cells [138].

3.4 Methane Reforming Model

3.4.1 Introduction

Due to the high operating temperature of SOFCs, methane can be directly used as the fuel because it can be directly reformed inside the cells. The high operating temperature allows the reactions described in section 2.3 to take place within the SOFC. There are many reactions for converting methane into hydrogen-rich gas such as SMR, DR, and Oxidative Steam Reforming (OSR), depending on the gas present in the system, as shown in Figure 3-2.

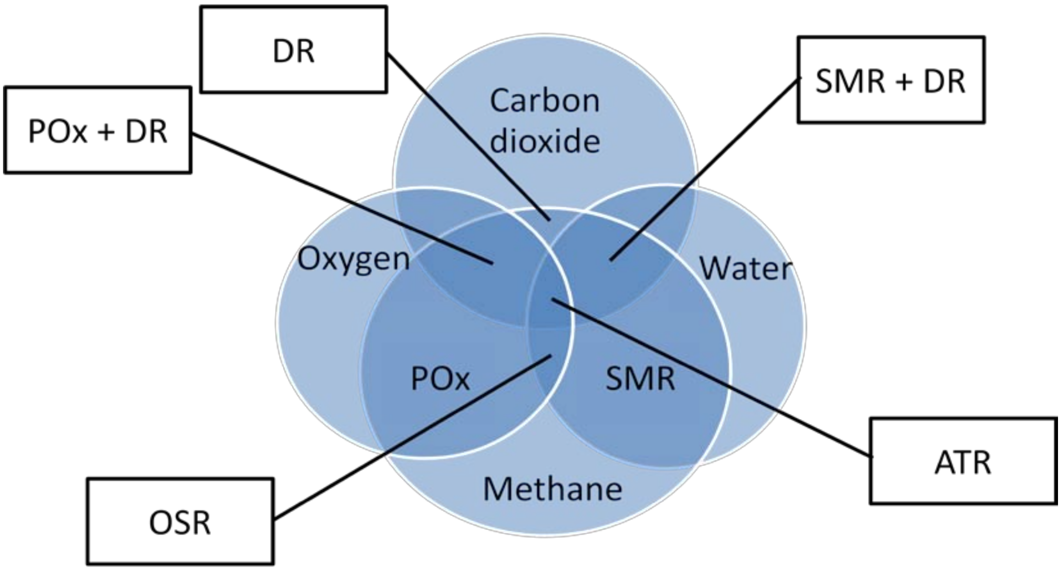

Figure 3-2 The methane reforming reactions at different conditions.

Figure 3-2 shows the preferred reactions by methane reforming at different reactant combinations. SMR occurs when the system has methane and water whilst DR takes place when water is replaced by carbon dioxide. Methane can be oxidised by the oxygen molecules existing in the system through the POx. OSR indicates methane is reformed into syngas through SMR and POx reactions.

In this work, two methods were introduced including kinetic and equilibrium approaches. The former focuses on the reaction rate, which tries to work out the consumption and production rates of each component in the system. The mole fraction and partial pressure can be derived by adding or subtracting the changes of moles from the reaction rate to the inlet fuel flow rate. Many factors must be considered such as the concentration of reactants, the type, the size and the amount of catalyst, as they will lead to difference in reaction rates. Autothermal Reforming (ATR) represents all reactions discussed in Figure 3-2 in which methane reacts with carbon dioxide, water and oxygen in a single system.

In this work, a 50% porosity fuel cell with 50% in weight nickel was assumed for building an SOFC-based reforming model, which can provide the reaction speed based on the reactant concentrations and the operating conditions. On the other hand, the second method uses thermodynamic equilibrium to calculate the system status at equilibrium. Unlike the kinetic model, the equilibrium approach is only affected by temperature and pressure. In this work, the pressure will be fixed at 1 bar.

3.4.2 Steam Methane Reforming

The reaction rates of steam methane reforming that are used in this work are taken from Xu [78], and have been widely employed in many investigations [136, 137, 139-141]. However, Xu's work was based on pure catalyst reforming. The terms, *a*, *b*, and *c* are the consumption or production rates of SMR, WGS and DIR reactions with the units of kmol h^{-1} kg-catalyst^{-1} (cat). For application in SOFCs, the value of 5.0×10^{-4} effective factor, $\mathcal{C}$, is proposed by Wang et al [139] to adjust the reforming rate of Equation 3.39 to Equation 3.41 based on their experimental results. This is to account for the fact that the SOFC anode structure is porous, and the metal nickel is doped into the anode structure.

$$a = \frac{k_{SMR}}{P_{H_2}^{2.5}} \times \frac{\mathcal{C} \times (P_{CH_4}P_{H_2O} - \frac{P_{H_2}^3 P_{CO}}{K_{p,SMR}})}{(1.0 + k_{CO}P_{CO} + k_{H_2}P_{H_2} + k_{CH_4}P_{CH_4} + \frac{k_{H_2O}P_{H_2O}}{P_{H_2}})^2}$$

Equation 3.39

$$b = \frac{k_{WGS}}{P_{H_2}} \times \frac{\mathcal{C} \times (P_{CO}P_{H_2O} - \frac{P_{H_2} P_{CO_2}}{K_{P,WGS}})}{\left(1.0 + k_{CO}P_{CO} + k_{H_2}P_{H_2} + k_{CH_4}P_{CH_4} + \frac{k_{H_2O}P_{H_2O}}{P_{H_2}}\right)^2}$$

Equation 3.40

$$c = \frac{\mathscr{k}_{DIR}}{P_{H_2}^{3.5}} \times \frac{\mathcal{C} \times (P_{CH_4}P_{H_2O}^2 - \frac{P_{H_2}^4 P_{CO_2}}{K_{P,DIR}})}{(1.0 + k_{CO}P_{CO} + k_{H_2}P_{H_2} + k_{CH_4}P_{CH_4} + \frac{k_{H_2O}P_{H_2O}}{P_{H_2}})^2}$$ Equation 3.41

The term $\mathscr{k}_i$ (i = SMR, WGS and DIR) are the rate constants of the SMR, WGS and DIR with the unit of kmol kPa$^{0.5}$ kg-cat^{-1} hour^{-1} for SMR and DIR and kmol kPa^{-1} kg-cat^{-1} hour^{-1} for WGS. The adsorption constants k_i (i = H_2O, CO, CH_4, H_2) can be obtained from Arrhenius and Van't Hoff equations and the unit is kpa^{-1}[78, 136].

$$\mathscr{k} = \mathcal{D}_i exp^{(\frac{-\mathcal{E}_{act,i}}{RT})}$$ Equation 3.42

$$k_i = D_i exp^{(\frac{\Delta H_{ads,i}}{RT})}$$ Equation 3.43

$\mathcal{D}_i$ (i = SMR, WGS and DIR) and D_i (i = H_2O, CO, CH_4, H_2) are the dimensionless pre-exponential factors. $\mathcal{E}_{act,i}$ (i = SMR, WGS and DIR) are the activation energies and $\Delta H_{ads,i}$ (i = H_2O, CO, CH_4, H_2) are the adsorption enthalpies with the same unit of Joule per mole. R and T are the universal gas constant and temperature in Kelvin respectively. A set of values were suggested by various sources in the literatures [78, 136, 140]. These are listed in Table 3.1 and Table 3.2.

Table 3.1 The activation energies and the pre-exponential factors for different reactions.

$\mathcal{E}_{\text{act, SMR}}$	$\mathcal{E}_{\text{act, WGS}}$	$\mathcal{E}_{\text{act, DIR}}$	$\mathcal{D}_{SMR}$	$\mathcal{D}_{WGS}$	$\mathcal{D}_{DIR}$
240100	67130	243900	4.225×10^{15}	1.955×10^{6}	1.020×10^{15}

Table 3.2 The pre-exponential factors and adsorption enthalpies for different elements.

D_{CH4}	D_{CO}	D_{H2O}	D_{H2}	$\Delta H_{\text{ads, CH4}}$	$\Delta H_{\text{ads, CO}}$	$\Delta H_{\text{ads, H2O}}$	$\Delta H_{\text{ads, H2}}$
6.65×10^{-4}	8.23×10^{-5}	1.77×10^{5}	6.12×10^{-9}	-38280	-70650	-88680	-82900

$K_{P,\,i}$ (i = SMR, WGS and DIR) are the equilibrium constants suggested by Wang et al. and Hou [94, 139].

$$\mathrm{K}_{\mathrm{P,SMR}} = 1.198 \times 10^{17} exp^{(\frac{-26830}{RT})} \quad \text{Equation 3.44}$$

$$\mathrm{K}_{\mathrm{P,WGS}} = 1.767 \times 10^{-2} exp^{(\frac{4400}{RT})} \quad \text{Equation 3.45}$$

$$\mathrm{K}_{\mathrm{P,DIR}} = 2.117 \times 10^{15} exp^{(\frac{-22430}{RT})} \quad \text{Equation 3.46}$$

3.5 Carbon Activity

The carbon activity coefficients, α, are the reaction quotients divided by the equilibrium constants. Carbon coefficient α_{MC} and α_{BD} were introduced to determine the possibility of carbon formation from methane cracking (Equation 2.31) and Boudouard reaction (Equation 2.32), as defined in the following [62, 131],

$$\alpha_{\mathrm{MC}} = \frac{P_{H_2}^2}{P_{CH_4} \times K_{P,MC}} \quad \text{Equation 3.47}$$

$$\alpha_{BD} = \frac{P_{CO_2}}{P_{CO}^2 \times K_{P,BD}} \quad \text{Equation 3.48}$$

where Pi (i = H_2, CH_4 and CO) are the partial pressure of hydrogen, methane and carbon monoxide, and $K_{P,i}$ (i = MC and BD) are the equilibrium constants of methane cracking and Boudouard reactions, which were obtained from literature [94, 121, 139], as listed in Equation 3.49 and Equation 3.50. The term T is the absolute temperature.

$$\mathrm{K_{P,MC}} = 4.161 \times 10^{7} \times \exp^{\left(\frac{-10614}{\mathrm{T}}\right)} \quad \text{Equation 3.49}$$

$$\mathrm{K_{P,BD}} = 5.744 \times 10^{-12} \times \exp^{\left(\frac{20634}{\mathrm{T}}\right)} \quad \text{Equation 3.50}$$

However, syngas formation (the reversed Equation 2.33) can be used to remove solid carbon in the cell under certain operating conditions. The equilibrium constant for RSF ($K_{P,\ RSF}$) can also be found in Hou's work [94] and thus the carbon activity for RSF (α_{RSF}) are,

$$\mathrm{K_{P,RSF}} = 3.173 \times 10^{-10} \exp\left(\frac{16318}{\mathrm{T}}\right) \qquad \text{Equation 3.51}$$

$$\alpha_{RSF} = \frac{P_{H_2O}}{P_{H_2} \times P_{CO} \times K_{P,RSF}} \qquad \text{Equation 3.52}$$

where P_i (i= CH_4, H_2, CO and H_2O) are the partial pressures of each gas. If α is less than one, the formation of solid carbon is thermodynamically possible. Another coefficient, γ, was suggested by Klein and Eveloy [62, 88] for the situations when either α_{MC} or α_{BD} is less than 1, whilst the other is greater.

$$\gamma_{MC-BD} = \alpha_{\mathrm{MC}} \times \alpha_{BD} \qquad \text{Equation 3.53}$$

The results provide the status, and reaction direction of the chemical reactions considered. For the case that α is less than 1, the reaction has not reached equilibrium, thus the reaction direction is forward, producing more products. Otherwise, the excess products reverse the reaction and more of the original reactants are producing. As a result, this method can also be applied when three reactions, including methane cracking (Equation 2.31), Boudouard (Equation 2.32) and RSF (Equation 2.33) are considered simultaneously, as shown in Equation 3.54.

$$\gamma_{MC-BD-RSF} = \alpha_{\mathrm{MC}} \times \alpha_{BD} \times \alpha_{RSF} \qquad \text{Equation 3.54}$$

And since solid carbon is the product in all three reactions, the value 1 is still the boundary for carbon formation. A natural logarithm gamma, *ln(γ)*, was introduced in this work to make the boundary easily visible, as zero is the threshold of carbon formation in the system, and *ln(γ)* can easily show the distance of the system away from carbon deposition. If *ln(γ)* is negative, it is thermodynamically possible that solid carbon formation could happen, otherwise, the system is expected to successfully inhibit carbon deposition.

By considering these three reactions (MC, BD and RSF), all the main products exist in the methane reforming (methane, steam, carbon monoxide, carbon dioxide, hydrogen and solid carbon) were considered simultaneously. Steam methane reforming reaction (Equation 2.10) can be obtained by combining methane cracking (Equation 2.31) and syngas formation (reversed Equation 2.33) reactions. Similarly, water gas shift reaction (Equation 2.11) can be derived from the combination of Boudouard (Equation 2.32) and syngas formation. Combining methane cracking and reversed Boudouard reactions can lead to methane dry reforming reaction (Equation 2.12).

3.6 Performance Monitoring

Many measurements are used to examine the performance of a system, for example, monitoring of the anode off-gas recirculation system performance from the methane reforming, fuel utilisation, and system efficiency. The definitions of performance from different prospective are defined in this section.

3.6.1 Steam to Carbon Ratio, Oxygen to Carbon Ratio

The Steam to Carbon (*S/C*) ratio is defined as the number of water molecules divided by the number of carbon atoms in the system, as given in Equation 3.55 [142]. The term is usually used for the steam methane reforming reactions and under the circumstance when only steam and methane are given as the initial fuel input. Equation 3.55 can therefore be rewritten as Equation 3.56.

$$\mathrm{S/C\ ratio} = \frac{n_{H_2O}}{n_{CH_4} + n_{CO_2} + n_{CO}} \qquad \text{Equation 3.55}$$

$$\mathrm{S/C\ ratio} = \frac{n_{H_2O}}{n_{CH_4}} \qquad \text{Equation 3.56}$$

Carbon monoxide is the product of SMR, and can also be oxidised into carbon dioxide within SOFCs. Thus it can be found in the recycled exhaust gas. Moreover, carbon monoxide and carbon dioxide can react with methane through the WGS and

DR reactions to produce hydrogen. This lowers the concentrations of carbon monoxide and methane, which are the sources of the carbon deposition. The Oxygen to Carbon (*O/C*) ratio defined in Equation 3.57 is expected to provide a better picture of the reforming conditions [123]. By using the *O/C* ratio inside the fuel stream, this ratio can be used to determine the formation of carbon based on the thermodynamic equilibrium.

$$\mathrm{O/C\ ratio} = \frac{\mathrm{n_{H_2O}} + 2 \times \mathrm{n_{CO_2}} + \mathrm{n_{CO}}}{\mathrm{n_{CH_4}} + \mathrm{n_{CO_2}} + \mathrm{n_{CO}}} \qquad \text{Equation 3.57}$$

3.6.2 Efficiency Monitoring

There are many coefficients for measuring the system efficiency. The overall efficiency (η) here is determined as fuel cell power divided by the change of enthalpy, as given in Equation 3.58. Other measurements of efficiency, such as thermodynamic efficiency (η_{thermo}, Equation 3.59) and voltage efficiency (η_V, Equation 3.60) are also listed in the following. Equation 3.58 and Equation 3.60 can be directly monitored, whereas the values of the change of enthalpy *(ΔH)* and Gibbs free energy (*ΔG)* will need to be taken from other reference sources.

$$\eta = \frac{\mathrm{w_{elec}}}{\Delta \mathrm{H}} \qquad \text{Equation 3.58}$$

$$\eta_{\mathrm{thermo}} = \frac{\Delta G}{\Delta H}$$ Equation 3.59

$$\eta_{V} = \frac{E_{\mathrm{cell}}}{E_{\mathrm{Nert}}}$$ Equation 3.60

Here W_{elec} is the electrical power produced by the cell, E_i (i = cell, Ner) represent the cell and Nernst voltage, respectively.

3.6.3 Fuel Utilisation

The fuel utilisation (u_f) can be obtained from Equation 3.61, I is the current in amperes, N is the electron transfer number, which depends upon the fuel used. The term υ is the fuel flow rate with units of Standard Cubic Centimetre per Minute (sccm), equivalent to a millilitre per minute.

$$u_f = \frac{I}{NF\upsilon}$$ Equation 3.61

This equation holds only for a single fuel. For the case where SOFCs oxidise several fuels at the same time (e.g. hydrogen and carbon monoxide), the fuel utilisation is assumed to be related to the fuel mole fraction. For example, in this work, both hydrogen and carbon monoxide are fuels for SOFC simultaneously, the fuel utilisation of hydrogen ($u_{f,\,H_2}$) and carbon monoxide ($u_{f,\,CO}$) is defined as in Equation 3.62 and

Equation 3.63.

$$u_{f,H_2} = \frac{I \times \frac{P_{H_2}}{P_{CO} + P_{H_2}}}{N \times F \times \upsilon_{H_2}} \qquad \text{Equation 3.62}$$

$$u_{f,CO} = \frac{I \times \frac{P_{CO}}{P_{CO} + P_{H_2}}}{N \times F \times \upsilon_{CO}} \qquad \text{Equation 3.63}$$

Here, P_i (i = H_2, CO) are the partial pressure of hydrogen and carbon monoxide. The term ν_i (i = H_2, CO) are the inlet fuel flow rates of hydrogen and carbon monoxide, which are controlled by the Mass Flow Controllers (MFCs), so the partial pressures can be calculated. As the output current is measured, the utilisation is then obtained.

3.6.4 Conversion Rates

In order to examine the reforming performance, the conversion rates for different species in the reactions are listed in Equation 3.64 to Equation 3.67. However, in practical experiments, the inlet gas flow was shown to be less than expected due to the back pressure inside the reaction tube. The methane inlet flow can sometimes be replaced by the sum of the carbon monoxide, carbon dioxide and methane at exhaust, under the assumption that no solid carbon is formed. The conversion rate can be determined by utilising the following equations [140]:

$$\text{Methane conversion rate} = \frac{\nu_{\mathrm{CH_4,in}} - \nu_{\mathrm{CH_4,out}}}{\nu_{\mathrm{CH_4,in}}} \qquad \text{Equation 3.64}$$

$$\text{Carbon dioxide conversion rate} = \frac{\nu_{\mathrm{CO_2,in}} - \nu_{\mathrm{CO_2,out}}}{\nu_{\mathrm{CO_2,in}}} \qquad \text{Equation 3.65}$$

$$\text{Carbon monoxide yleid } = \frac{\nu_{\mathrm{CO,out}}}{\nu_{\mathrm{CH_4,in}} + \nu_{\mathrm{CO_2,in}}} \qquad \text{Equation 3.66}$$

$$\text{Hydrogen yield } = \frac{\nu_{\mathrm{H_2,out}}}{\nu_{\mathrm{CH_4,in}}} \qquad \text{Equation 3.67}$$

Here, the term ν_i (i=CH_4, H_2, CO, CO_2) represent the flow rate of each gas in sccm.

3.7 Experimental Setup

In the SOFC internal methane reforming with AOGR, both carbon dioxide and steam are recycled back to the fuel inlet stream, so these gases are competing with each other to react with methane. This experimental setup was used to allow a more detailed investigation to the interactions among the reactions. The catalyst used in the experiment was a commercial half cell, consisting of an anode and an electrolyte. Sample of the cell was examined by using X-Ray Fluorescence (XRF) to determine both the components, and the nickel concentration. The Temperature Programmed Reduction (TPR) technique was employed to find the optimal temperature for the reduction of the catalyst.

Different amount of methane, steam and carbon dioxide was given to the catalyst at 750 ℃ for the reforming reactions. The reformed gases were then analysed by an on-line Gas Chromatography (GC) and the catalyst was then examined for the carbon formation by using Temperature Programmed Oxidation (TPO) and TGA Thermogravimetric Analysis (TGA). The results were then compared with the results from thermodynamic modelling.

3.7.1 Catalyst Preparation

X-Ray Fluorescence

The Bruker S8 Tiger XRF was employed to determine the composition of the cell which acted as the catalyst in this experiment. The results show, as in Figure 3-3, that the commercial half cell (Ni-YSZ anode and YSZ electrolyte) has 50% nickel with 47% zirconium, and the final 3% being yttrium.

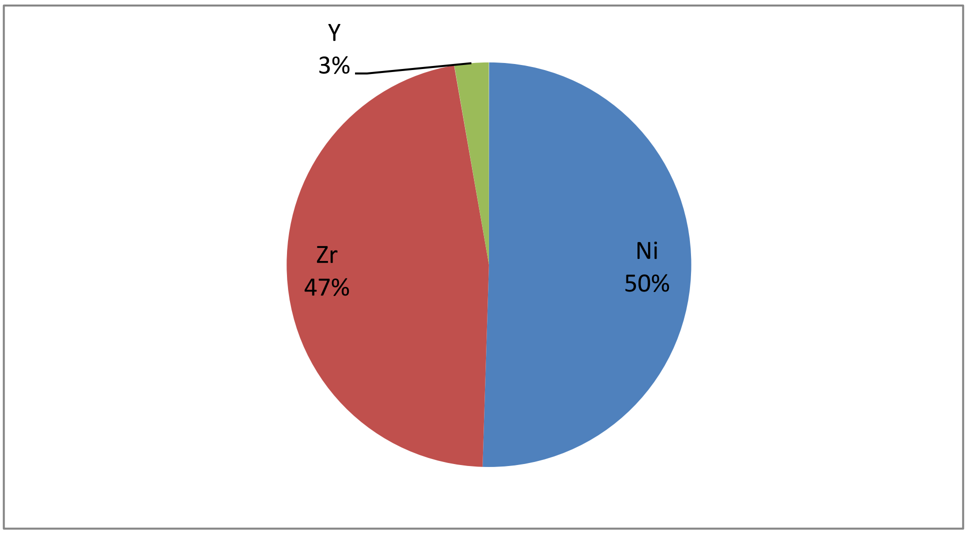

Figure 3-3 The half-cell composition.

Temperature Programmed Reduction

Temperature Programmed Reduction was used to determine at which temperature the catalyst can be fully reduced. In this experiment, it was the nickel oxide from the half-cell reduced to metallic nickel. The Micromeritics Autochem II Chemisorption Analyser, shown in Figure 3-4, was employed to examine the reduction temperature of the catalyst. The sample of the half-cell weighted 0.1 gram was placed in an U-shaped tube and inserted into the analyser. The sample was heated up from room temperature to 500 ℃ at the rate of 10 ℃ min^{-1} and then cooled down to 25 ℃, in a helium atmosphere. This technique removed the impurities within the catalyst. Afterwards, the temperature was increased again at the rate of 10 ℃ min^{-1} to 800 ℃ under a mixed gas atmosphere consisting of 10% hydrogen and 90% helium. The

Thermal Conductivity Detector (TCD) result shown in Figure 3-5 indicates that the nickel oxide was almost fully reduced into nickel at around 750 ℃. Thus, the catalyst was reduced at 750 ℃ before the methane reforming reactions in all the following experiments.

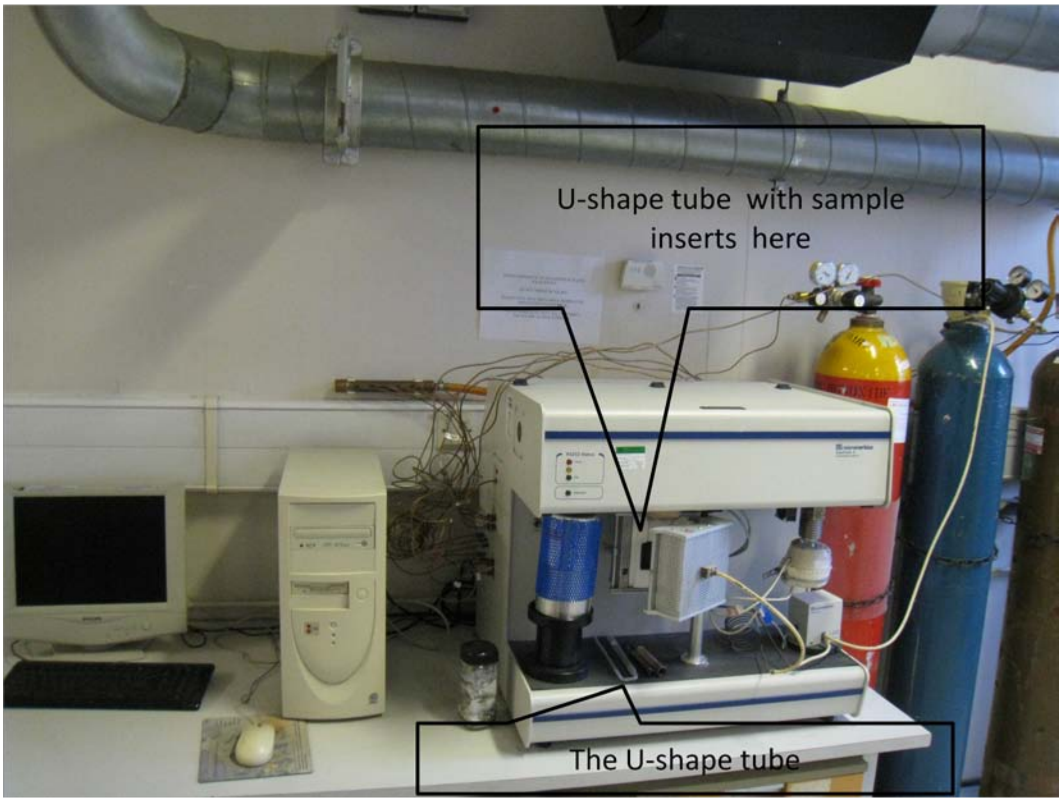

Figure 3-4 The TPR setup.

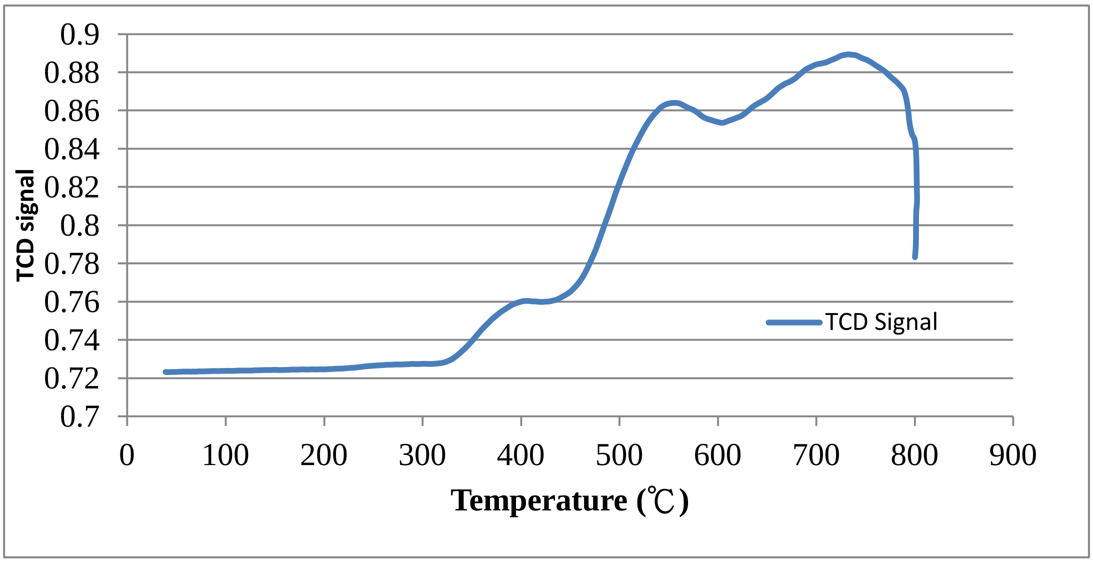

Figure 3-5 The TCD signal of the catalyst at different temperatures from the TPR method.

3.7.2 Reforming Preparation

For the reforming experiment, the SOFC half cell was ground into a powder then mixed with Silicon Carbide (SiC). A mixture consisting of a 0.2 g of the ground cell (particle size smaller than 600 μm) and 1.8 g SiC was placed at the centre of the reaction tube (fixed bed reactor). The SiC added to the catalyst was selected as an inert material to avoid gas pressure drop, particles clogging and catalyst bypass. Quartz wool was used at both sides of the catalyst bed in order to both support the catalyst and separate the catalyst bed from the pure SiC loaded in both ends. An additional layer of pure SiC was used on the top to distribute the fuel flow to allow it to evenly react with the catalyst and to heat up the fuel gas to the reacting temperature. The bottom SiC was used to support the catalyst bed. At the bottom of the reactor, glass wool was used as an additional support for the SiC and the catalyst, as shown in Figure 3-6.

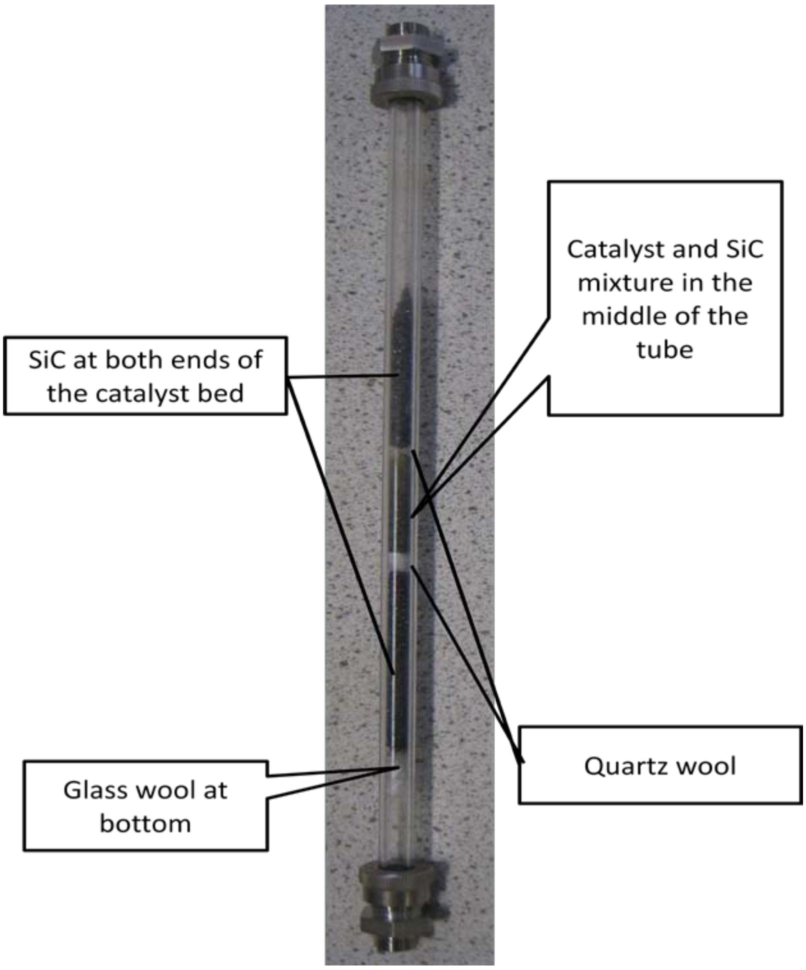

Figure 3-6 The reaction tube set up – quartz tube id-6 mm.

At the fuel supply end, the methane inlet flow rate was fixed at 25 ml min^{-1} in all of the experiments, expect in case 6. Carbon dioxide and water were added in different ratios, along with methane as listed in Table 5.1. All gaseous reactants were controlled by digital Brooks 5850S mass flow controller. Water is given in the unit of grams because it is in liquid form at room temperature. The amount of 0.02 g liquid water was pumped through a Cole-Palmer EW74930-05 series one pump and used for the 25 sccm of steam in the experiment. The liquid water was heated up to 120 ℃ by the OMEGA FGR - 100 trace heating tape controlled by a West 2300 PID controller to generate steam and then mixed with the other gases before being injected into the system. However, the test tube was not tested with no catalyst filled in as the aim of this work is to simulate the methane internal reforming inside SOFCs and the reforming reactions were assumed not to occur without the catalyst.

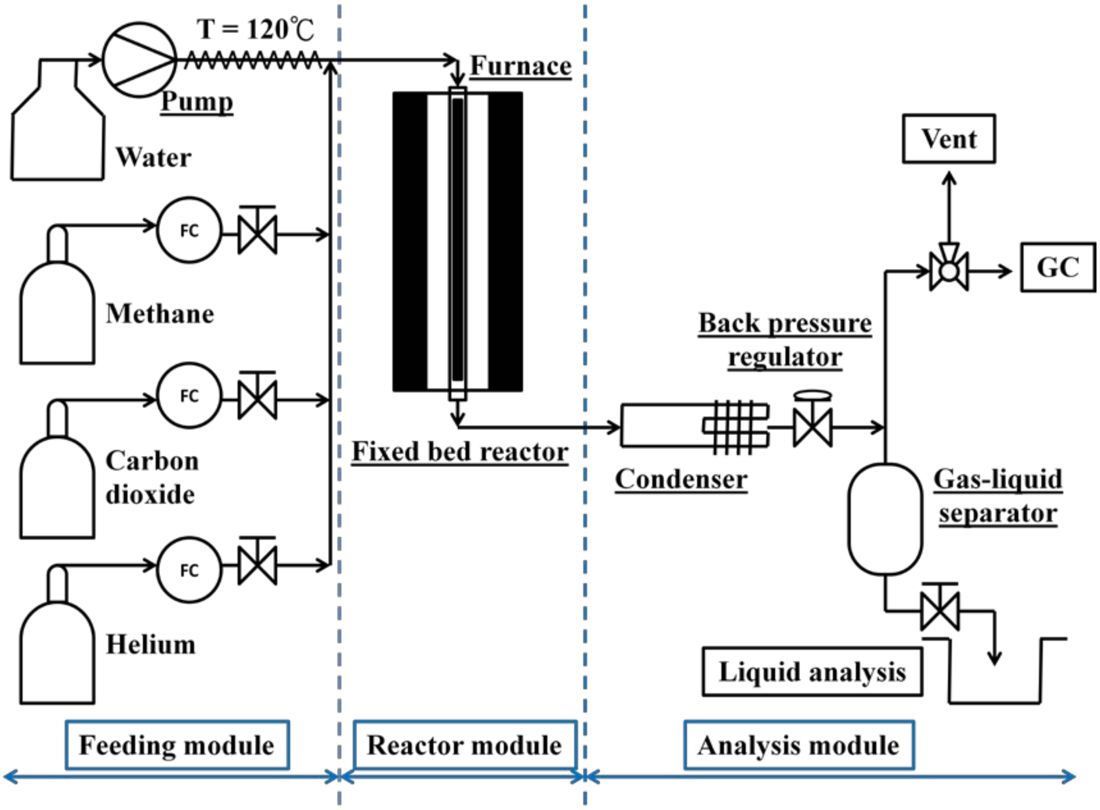

Figure 3-7 The Experimental process flow diagram.

The reaction tube was placed inside a tubular furnace (Seven thermo solutions TF 38-3-12-F) and connected to the fuel supply system, as shown in Figure 3-7 and Figure 3-8.The whole system was operating without being pressurised and the exhaust is open to the air, thus it is assumed that there is no pressure drop inside the reaction tube.

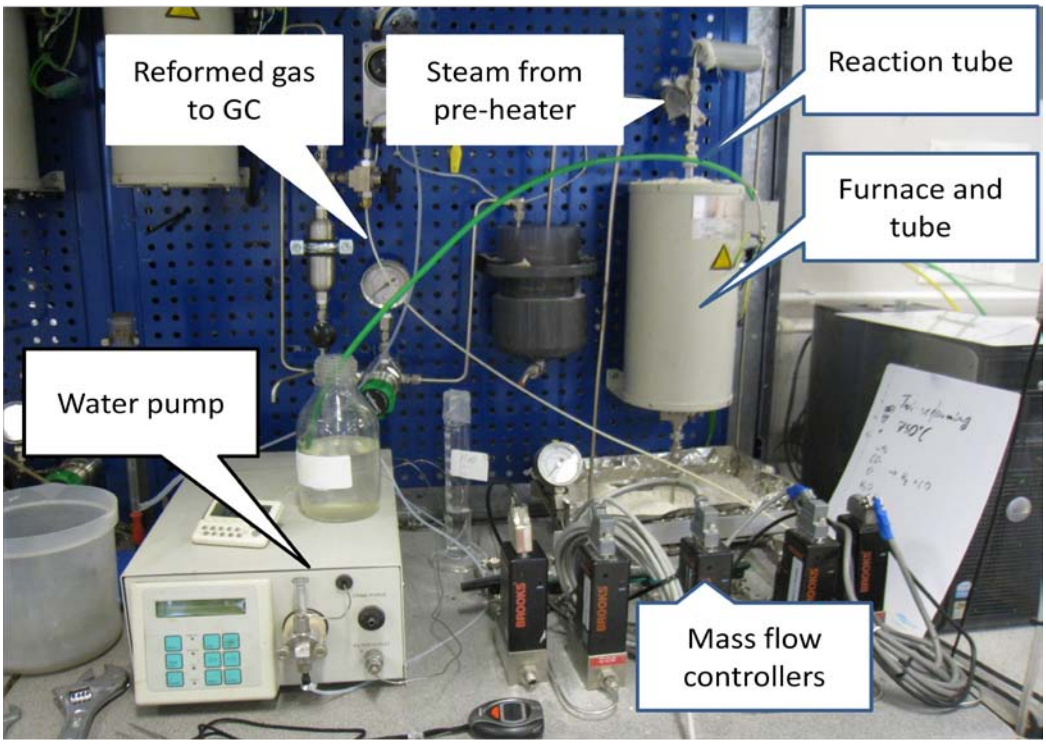

Figure 3-8 The test rig layout.

The furnace is controlled by a EUROTHERM PID controller. Gaseous products at the reactor exhaust were analysed by an on-line Gas Chromatography (Agilent Technologies 7890A) after cooling and condensing any water. Prior to the reaction, the catalyst was reduced (in situ) with a continuous flow of 10 sccm stream of hydrogen, and heated from room temperature to 200 ℃ at an initial rate of 20 ℃ min^{-1}, and then slowed down to 5 ℃ min^{-1} until the system reached 750 ℃ in order to prevent nickel aggregation. Afterwards, the system was kept at 750 ℃ with 10 sccm of hydrogen constantly flowing for another hour, which allowed the nickel oxide to be fully reduced into metallic nickel. After that, an 100 sccm of helium was given for 5 minutes before the reforming reactions started.

During the reaction process, the reformed gases were analysed by the GC after the first 15 minutes, 30 minutes, and then every 30 minutes until 4.5 hours had passed. The gas composition in different cases is listed in Table 5.1. The ratio of 2.0 between steam and methane was not tested experimentally as the modelling results in section 5.2 showed that the 1.5 steam to methane molar ratio was sufficient to prevent carbon formation. As a result, the 1.0 and 1.5 steam to methane molar ratio were sufficient to present the steam methane reforming reactions as a whole.

3.7.3 Carbon Formation Analysis

Thermogravimetric Analysis

The TGA was used here to examine the solid carbon formed from the reforming reactions. The principle was to heat up the sample with a constant air flow. As the temperature increases, the solid carbon formed in the sample is then oxidised and forms carbon dioxide gas which escapes into the atmosphere, thus reducing the weight of the sample. In the experiment, NETZSCH TG209F thermo-microbalance was employed to examine the carbon in the sample. In this analysis, the half-cell made catalyst from the various experiments previously explained (in section 3.7.1). was firstly separated from the mixture with SiC. A small amount of the used catalyst (around 25 mg) was then used for the analysis.

However, the metallic nickel was also oxidised in the examination. This led to the weight increase, which reduced the weight decrease from the oxidation of carbon. In order to overcome this, a sample of the unused catalyst was reduced and the oxidised to measure the weight change. For the reduction/oxidation, the sample was heated up from room temperature to 900 ℃ at a rate of 10 ℃ min^{-1} with an hydrogen/air flow rate of 40 sccm. The weight change in percentage against the reference was then turned into to the numerical date, for comparing with the TPO results.

Temperature Programmed Oxidation

The TPO technique was used as a different approach to determine the amount of solid carbon formed within the catalyst from the reforming reactions. By heating up the sample to a high temperature under an oxygen atmosphere, the solid carbon reacts with the oxygen and forms carbon dioxide which will be examined by the Mass Spectrometer (MS) directly connected to the exhaust of the experimental setup. The difference between TPO and TGA is that the TPO examines the gaseous carbon dioxide from the oxidation of solid carbon; whilst the TGA method is focusing on the weight change of the sample. As a result, the TPO method is not affected by the oxidation of metallic nickel.

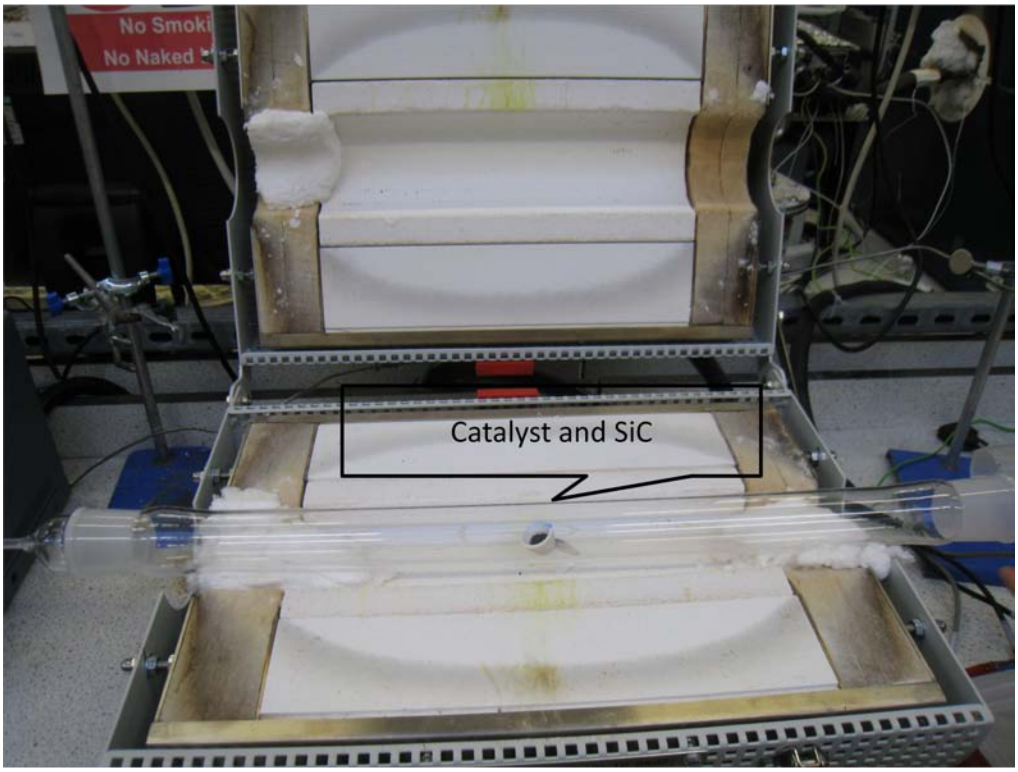

Figure 3-9 The TPO experiment setup.

An amount of 1 gram of catalyst bed (mixture of catalyst and SiC) used in the methane reforming was placed in the centre of a quartz tube inside a furnace, as shown in Figure 3-9. The exhaust from the tube was connected to the on-line MKS minilab LM80 mass spectrometry. A gas mixture consisting of 40 sccm helium and 10 sccm oxygen was entered at room temperature for 1 hour to remove the impurities. The tube was then heated up with the same gas condition at a rate of 10 ℃ min^{-1} to 900 ℃ and kept for 30 minutes or longer until no carbon dioxide signal was shown in the MS. This allowed the solid carbon formed from the reforming experiment to be oxidised into carbon dioxide gas and then detected by the MS connected at the exhaust. The tube was then cooled down naturally under a 50 sccm helium gas flow. The catalyst bed was then separated into SiC and the ground half-cell, for which the weight was used to work out the amount of carbon formed per gram of the catalyst.

The total amount of carbon dioxide generated during the oxidation of the spent catalyst was calculated by summarising all the carbon dioxide signals from the MS during the TPO. Signals from carbon dioxide 25 minutes before and after the peak, respectively, were added and used for the further calculation.

Chapter 4 The Determination of Carbon Formation

4.1 Introduction

Carbon formation from methane internal reforming is one of the major problems that needs to be addressed. Two methods for determining carbon formation based on thermodynamic equilibrium were mentioned in literature [62, 88, 130, 131, 143] - namely, a Carbon-Steam Equilibrium (C-S EQ) and a Carbon Activity (CA) approach. Both of them are expected to provide a rough idea about whether the system is going to be suffered from carbon formation at thermodynamic equilibrium. Then the system operating conditions (i.e. pressure, temperature or steam to methane ratio) can be adjusted accordingly. The former one was used as a reference for a suitable ratio between steam and methane when only these two gases were fed to SOFCs as the fuel. The latter, on the other hand, is expected to be applied to the system which contains other carbon oxides. However the mechanism and the application occasions of these two approaches were rarely seen. In this chapter, two methods were compiled from the theories and calculation processes, followed by the discussions of application occasions.

4.2 Carbon-Steam Equilibrium Method

4.2.1 Mathematical Derivation

The C-S EQ method was mentioned in the literature [130, 131, 143], but the theories and calculation details are not provided. This method only focuses on how much water is required at the system input to prevent formation of soot within it without calculating the concentrations of each species exactly. The main reactions leading to carbon formation, methane cracking (Equation 2.31), the Boudouard reaction (Equation 2.32) and reverse syngas formation (Equation 2.33), were considered in this model. On the other hand, the formed solid carbon can be removed via the syngas formation reaction. By considering these three reactions, the other three reactions, SMR, WGS and DR were also considered simultaneously, as SMR is the sum of methane cracking and syngas formation, WGS can be obtained from adding syngas formation and Boudouard reactions whilst methane dry reforming can be included from methane cracking and reverse Boudouard reaction. As a result, these reactions represent the full set of reactions to obtain equilibrium. By using the three reaction equilibrium constants, three equations can be established as in Equation 4.1, Equation 4.2, and Equation 4.3.

$$K_{P,MC} = \frac{P_{H_2}^2}{P_{CH_4}}$$ Equation 4.1

$$K_{P,BD} = \frac{P_{CO_2}}{P_{CO}^2}$$ Equation 4.2

$$K_{P,RSF} = \frac{P_{CO}P_{H_2}}{P_{H2O}}$$ Equation 4.3

Here, P_i, (i = CH_4, CO, CO_2, H_2 and H_2O) represents the partial pressures of each gas in the system. The temperature dependent values of the equilibrium constants $K_{P,i}$ (i = MC, BD and RSF) were obtained from tabulated reaction data [5, 94]. Based on the element balance, Equation 4.4 was set.

$$P_{CH_4} + P_{CO_2} + P_{CO} + P_{H2O} + P_{H_2} = 1$$ Equation 4.4

The term ψ is the ratio between oxygen atoms to carbon atoms. For a system initially containing only methane and water, this is equal to the initial ratio of steam to methane, and $\psi + 2$ is equal to the ratio of hydrogen molecules to carbon atoms (H_2/C ratio). Moreover, due to the conservation of elements, the relationship remains constant throughout the reforming process. This relationship results in Equation 4.5 and Equation 4.6

$$\psi = \frac{P_{H2O} + P_{CO} + 2 \times P_{CO_2}}{P_{CH_4} + P_{CO} + P_{CO_2}}$$ Equation 4.5

$$\psi + 2 = \frac{P_{H_2} + P_{H2O} + 2 \times P_{CH_4}}{P_{CH_4} + P_{CO} + P_{CO_2}} \qquad \text{Equation 4.6}$$

The six equations, Equation 4.1 to Equation 4.6, for six unknowns can be solved, and the steam to methane ratio ψ required to prevent carbon formation is obtained. However, this method can only be applied to a fuel entering the reforming system that only contains steam and methane. Despite the fact that the produced carbon dioxide, carbon monoxide, and hydrogen are included in the calculation, the additional gases from outside the system lead to failure of this method. Moreover, this method is based on the assumption that there is no carbon formation inside the system, as the solid carbon is not included in the conservation of elements in Equation 4.5 and Equation 4.6.

An analytical mathematical simplification is employed, before these equations are processed for numerical solution. This reduces the unknowns, leads to a shorter calculation time and increases the accuracy of solution. Equation 4.1to Equation 4.3 can be rewritten as Equation 4.7 to Equation 4.9 and then substituted into Equation 4.4. Thus Equation 4.10 is obtained.

$$P_{CH_4} = \frac{P_{H_2}^2}{K_{P,MC}} \qquad \text{Equation 4.7}$$

$$P_{CO_2} = K_{P,BD} \times P_{CO}^2 \qquad \text{Equation 4.8}$$

$$P_{H2O} = \frac{P_{CO} \times P_{H_2}}{K_{P,RSF}} \qquad \text{Equation 4.9}$$

$$P_{CO} \times \left(K_{P,BD} \times P_{CO} + 1 + \frac{P_{H_2}}{K_{P,RSF}}\right) + P_{H_2} \times \left(\frac{P_{H_2}}{K_{P,MC}} + 1\right) - 1 = 0 \qquad \text{Equation 4.10}$$

Similarly, combining Equation 4.5 and Equation 4.6, and replacing Equation 4.7 to Equation 4.9, then Equation 4.11 is obtained and then rewritten into Equation 4.12.

$$\frac{\frac{P_{CO} \times P_{H_2}}{K_{P,RSF}} + P_{CO} + 2 \times K_{P,BD} \times P_{CO}^2}{\frac{P_{H_2}^2}{K_{P,MC}} + P_{CO} + K_{P,BD} \times P_{CO}^2} + 2 = \frac{P_{H_2} + \frac{P_{CO} \times P_{H_2}}{K_{P,RSF}} + 2 \times \frac{P_{H_2}^2}{K_{P,MC}}}{\frac{P_{H_2}^2}{K_{P,MC}} + P_{CO} + K_{P,BD} \times P_{CO}^2} \qquad \text{Equation 4.11}$$

$$P_{CO} \times (3 + 4 \times P_{CO} \times K_{P,BD}) - P_{H_2} = 0 \qquad \text{Equation 4.12}$$

Thus these six equations were reduced into Equation 4.11 and Equation 4.12. The two equations were solved and thus the steam to methane ratio (ψ) is obtained. In the above two equations, when a temperature is given, the equilibrium constants of MC, BD, and RSF are known (see section 3.5). As a result, only the hydrogen and carbon monoxide partial pressures remained uncrowned, and can be solved by using MATLAB® R2010b fsolve funcation, the code is in the attached CD. Once these the partial pressures of hydrogen and carbon monoxide are known, the partial pressures of other gases such as carbon dioxide, methane and steam are known. The programming code is given in the attached disc.

4.2.2 The Carbon-Steam Equilibrium Results

In Figure 4-1, the results show the critical S/C ratio for methane steam reforming to prevent carbon formation, when the three soot forming reactions are examined. At temperatures lower than 850 K, lower S/C ratios are required for the system with decreasing temperature. This is because methane cracking is more active at higher temperatures. At lower temperatures, despite there being abundant methane, only a small amount of methane cracks into soot and hydrogen. Meanwhile, the concentrations of carbon monoxide and hydrogen are relatively low for the RSF and Boudouard reactions. As a result, low S/C ratios are sufficient for the system to prevent carbon formation or to remove the soot. The methane cracking reaction becomes more active with increasing temperature, producing more hydrogen and soot. Thus the demand for water increases for the syngas formation reaction (Equation 2.33) to remove the carbon.

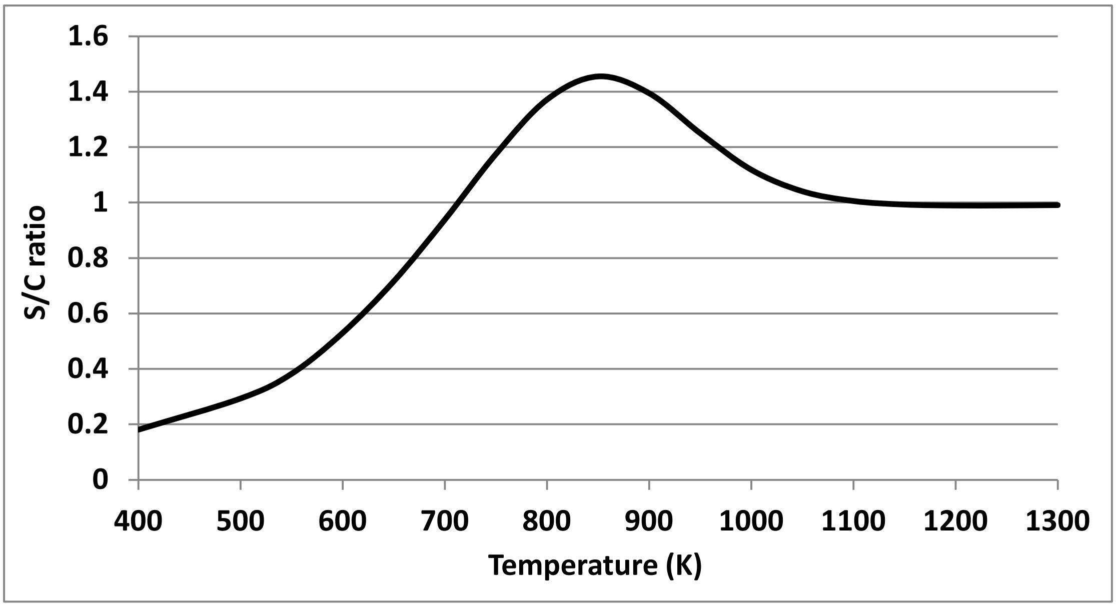

Figure 4-1 Critical S/C ratios for carbon formation at different temperatures. The graph is in accordance with the results presented in [143].

The system requires more steam at 850 K than at any other temperature to prevent carbon formation. This is because at this temperature, both Boudouard and methane cracking can occur, leading to carbon formation. Thus more water is required for the syngas formation reaction to remove solid carbon and turn it into hydrogen and carbon monoxide.

From above it can be seen that this method can be used as a reference when inputting fuels to an SOFC system. Nevertheless, for the SOFC with AOGR system, this method is not capable to determine the carbon formation, as the recycled gases break the relationships set in this method. As a result, the CA approach introduced in the next session is expected to overcome this problem. By providing identical system conditions, the CA is expected to provide the same result as the C-S EQ method.

4.3 Carbon Activity Method

4.3.1 Pre-Equilibrium

Computation of carbon activity has been introduced in many papers [62, 88]. The mechanism behind this method is to use the reaction quotient to determine whether the reaction has reached equilibrium. Then the reaction direction (forwards or backwards) can be determined. However, in order to compare with the C-S EQ method, a pre-equilibrium step was required in this method. This is because the C-S EQ method directly determines the system at equilibrium, the pre-equilibrium stage in this method is employed to provide the identical system for the CA method to be applied.

Different ratios of methane and steam, ranging from 0.5 to 2.5, were given as the initial state. SMR and WGS were the reactions considered for steam methane reforming. Although DIR has also been considered in some previous studies for steam methane reforming [78, 136], the concentration of the gases at equilibrium is expected to be the same for two reasons:

1. DIR is the sum of SMR and WGS. The concentration of each gas is considered instead of the amount consumed/produced through the reactions; and
2. As the concentration of each component is balanced, according to Le Chatelier's principle, the system should be effectively static. That means all species in the system are consumed and produced at the same rate so the concentrations remain constant.

Here P_i (i = CH_4, CO, CO_2, H_2O and H_2) are the partial pressures of each species, and $K_{P,i}$ (i = SMR, WGS and DIR) are the temperature dependent equilibrium constants for the three reforming reactions, which can be found in literature [95, 144].

$$\mathrm{K_{P,SMR}} = \frac{\mathrm{P_{CO}} \times \mathrm{P_{H_2}}^3}{\mathrm{P_{CH_4}} \times \mathrm{P_{H_2O}}} \quad \text{Equation 4.13}$$

$$\mathrm{K_{P,WGS}} = \frac{\mathrm{P_{CO_2}} \times \mathrm{P_{H_2}}}{\mathrm{P_{CO}} \times \mathrm{P_{H_2O}}} \quad \text{Equation 4.14}$$

$$\mathrm{K_{P,DIR}} = \frac{\mathrm{P_{CO_2}} \times \mathrm{P_{H_2}}^4}{\mathrm{P_{CH_4}} \times \mathrm{P_{H_2O}}^2} \quad \text{Equation 4.15}$$

Using any two of Equation 4.13 to Equation 4.15 is sufficient for calculating the homogeneous equilibrium. However, as the carbon formed will be solid, it is not included in any reaction above, because they only discuss the gaseous partial pressures only. In order to simultaneously consider the carbon, one of the carbon related reactions (MC, BD, and RSF) has to be considered.

Alternatively, the NASA Chemical Equilibrium with Applications (CEA) software was employed in this work to determine the compositions at equilibrium from different initial conditions [145]. The concentrations were calculated by using the minimised Gibbs free energy when the temperature, pressure and expected products were given. For the following work, the expected products were methane, water, carbon dioxide, carbon monoxide, hydrogen and solid carbon.

The concentrations at equilibrium from different initial conditions were then used in the carbon activity calculation to determine the boundary of the formation of solid carbon.

4.3.2 Compositions at Equilibrium

The following figures show the results of equilibrium gas composition by using the NASA CEA software. The low temperature favoured WGS reaction converts carbon monoxide produced from the SMR reaction into carbon dioxide at temperatures between 500 K and 750 K. Within this temperature range, the hydrogen and carbon dioxide concentrations are found to increase whilst the carbon monoxide concentration increases relatively little, as shown in Figure 4-2 to Figure 4-6.

As temperature increases above 750 K, the carbon monoxide concentrations start to increase and the hydrogen concentration is increasing sharply. This is because SMR, being strongly endothermic and thus a high-temperature favoured reaction, became more active and start dominating the reforming process. Even though the WGS reaction is still occurring, the reaction is less active compared with SMR. Additionally, with the increase of temperature, WGS starts to reverse and turn carbon dioxide and hydrogen back into water and carbon monoxide. SMR and reverse WGS lead to the result that carbon dioxide concentration decreases but carbon monoxide and hydrogen concentrations increase at temperatures above 900 K.

As shown in Figure 4-2, when S/C = 0.5, the water is entirely consumed for reforming reactions at temperatures above 1100 K and thus there was still some unreformed carbon monoxide, with 13% of solid carbon formed, because the unconverted methane, which is due to the insufficient steam, breaks down into solid carbon and hydrogen through the MC reaction (Equation 2.31). The carbon concentration decreases with the increase of carbon monoxide concentration when the steam concentration increases - doubling the steam to carbon ratio to S/C = 1.0 is shown in Figure 4-3. Both methane and water are almost entirely consumed and produce more hydrogen than in the S/C = 0.5 scenario at temperatures above 1100 K. Moreover, the amount of the formed carbon is decreased due to more steam being added to allow a more complete SMR reaction. However, for higher S/C ratios (e.g. S/C above 1.5), the abundant steam converts almost all methane into hydrogen and carbon monoxide, as shown in Figure 4-4 to Figure 4-6. Meanwhile, excess water remains within the system, which could lead to nickel corrosion, causing damage to the system and lowering the efficiency. Despite the fact that some carbon monoxide and water still exist in the system, as mentioned above, WGS is disfavoured at higher temperatures and thus no more hydrogen is produced at high temperatures.

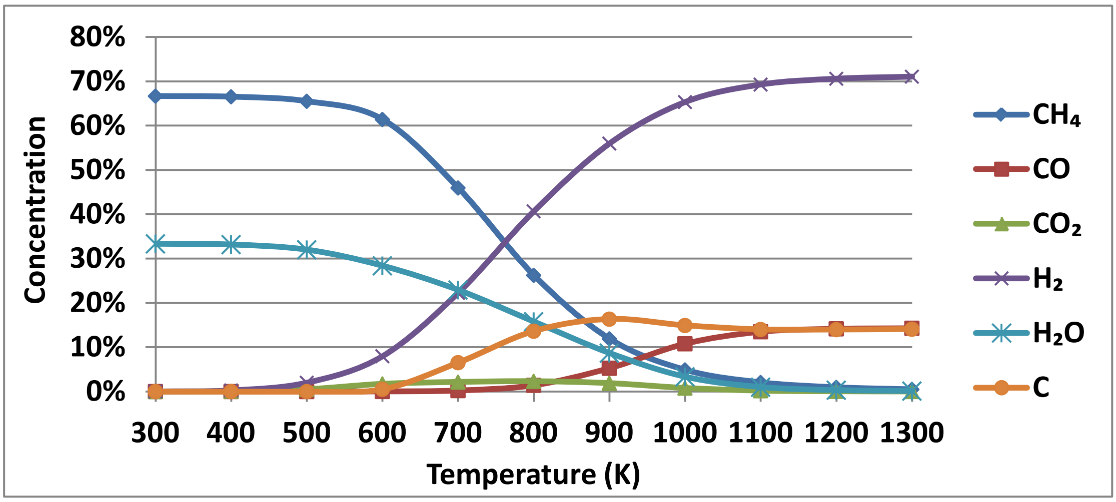

Figure 4-2 Element composition at equilibrium when S/C ratio is given at 0.5.

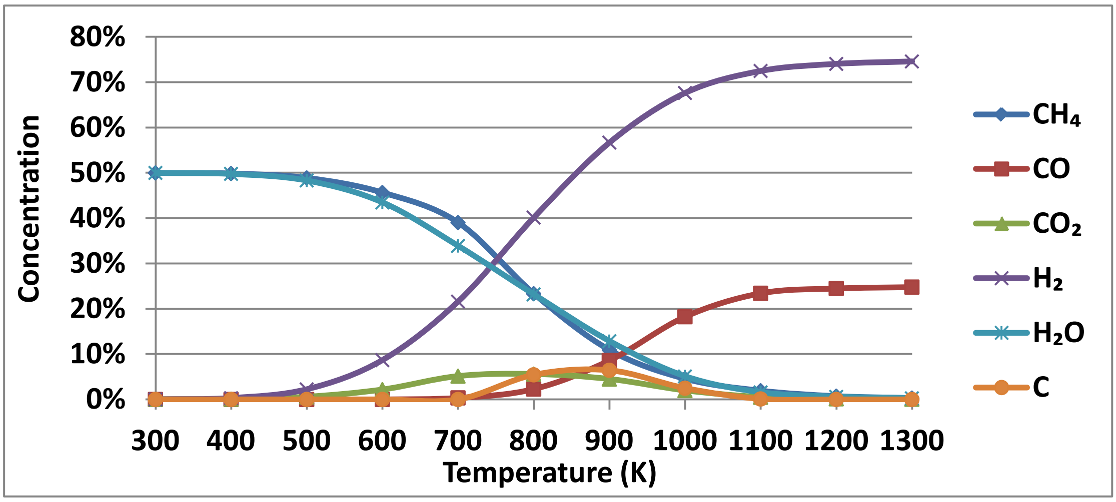

Figure 4-3 Element composition at equilibrium when S/C ratio is given at 1.0.

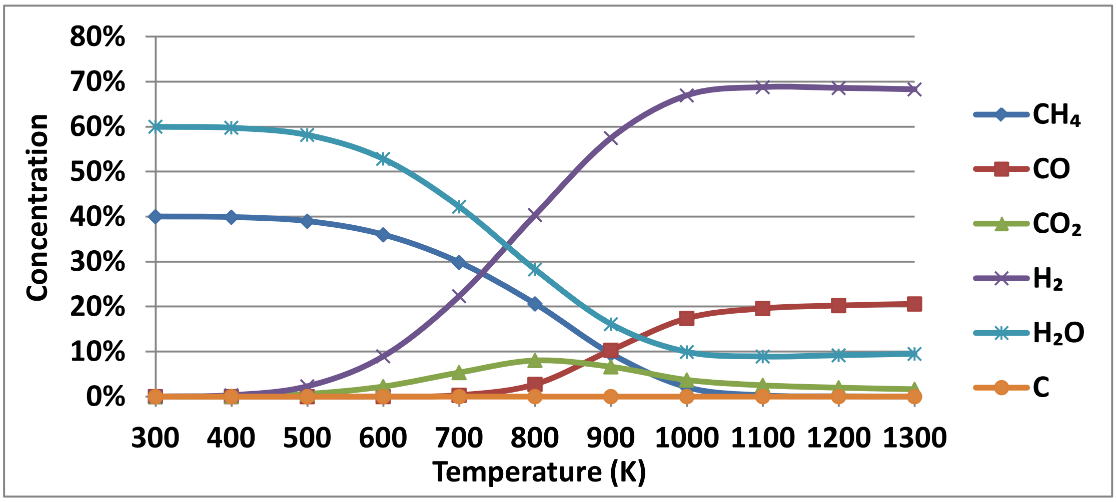

Figure 4-4 Element composition at equilibrium when S/C ratio is given at 1.5.

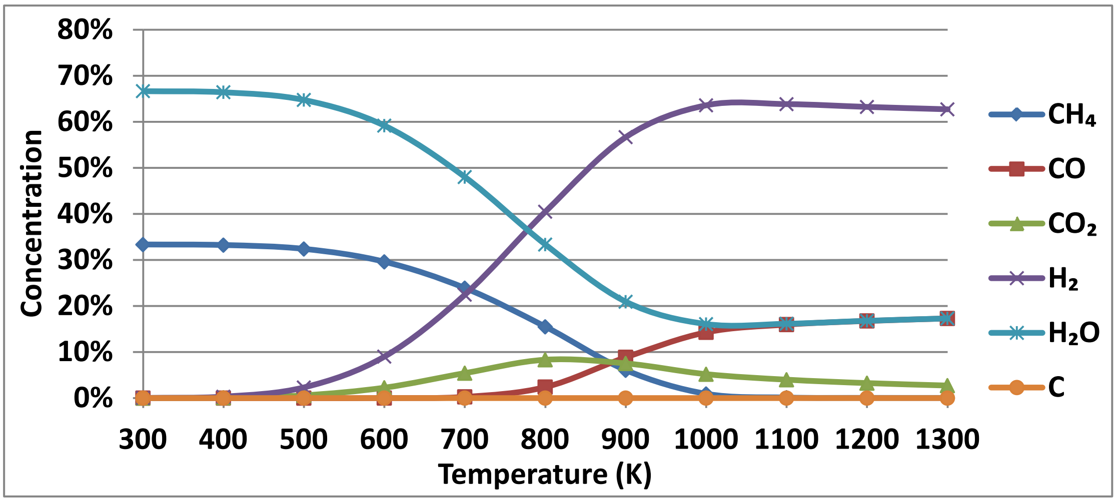

Figure 4-5 Element composition at equilibrium when S/C ratio is given at 2.0.

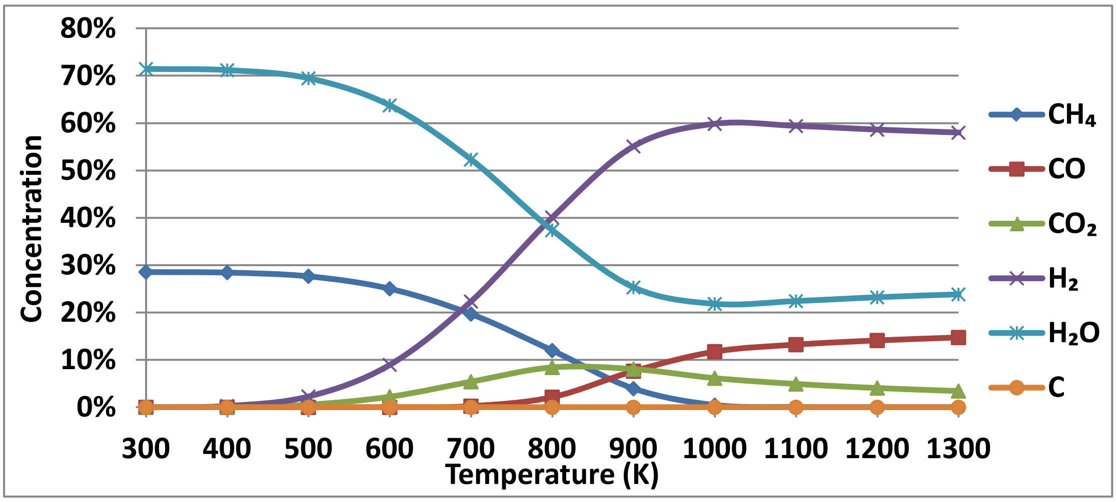

Figure 4-6 Element composition at equilibrium when S/C ratio is given at 2.5.

4.3.2 Carbon Activity Results

The second step of the CA approach is to use the carbon activity to determine the formation of carbon based on the concentration of gases at equilibrium (shown in Figure 4-2 to Figure 4-6) under various conditions. System operating temperatures below 600 K were not considered here for two reasons: firstly, the methane reforming reactions do not take place within this temperature range. The very small concentrations could lead to computational singularities. Secondly, SOFCs seldom operate within this lower temperature range because most materials used in SOFCs are not ionically conductive at these temperatures.

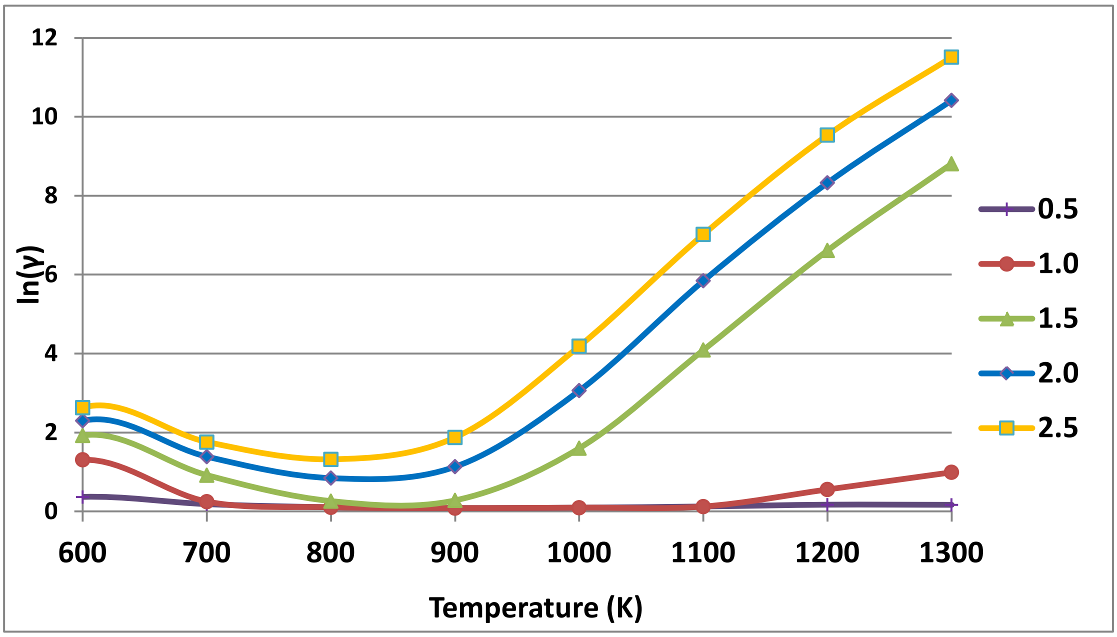

Figure 4-7 The temperature-dependent carbon formation region with different S/C ratio

Figure 4-7 shows the gamma function (Equation 3.54) results of the product of the three carbon activities based on the concentrations at equilibrium shown in Figure 4-2 to Figure 4-6. For the S/C = 0.5 scenario, the result is very close to the x-axis at all temperatures discussed. The carbon activities here only consider the gaseous concentration after the equilibrium thus the gamma is above the x-axis. This means that no more extra carbon will be formed from the residual gases. As a results, the S/C = 0.5 ratio between steam and methane in the initial fuel stream is expected to lead to carbon formation in the full range of 600 K - 1300 K, as shown in Figure 4-2.

For the S/C ratio = 1.0 in Figure 4-7, the gamma values are much higher than the 0.5 ones at temperatures below 700 K and above 1150 K. From Figure 4-3, it can be seen that carbon is formed within the temperature range 700 - 1100 K. As a result, it can be deduced that the 1.0 ratio between steam and methane is sufficient for preventing carbon formation at temperatures below 700 K and above 1100 K.

As can be understood, evaluation of the value of gamma is slightly ambiguous as values of $\gamma > 1$ can be obtained even if one of the α is less than 1. Therefore a value of $\gamma > 1$ from Equation 3.53 but close to "one" needs to be interpreted as "potentially carbon forming".

Figure 4-4 showed that no carbon was formed in equilibrium. Meanwhile, when referring to the S/C = 1.5 case in Figure 4-7, it can be seen that the value is very close to the x-axis at the temperature 850 K. This suggests that the gaseous concentrations at equilibrium are at the boundary of carbon formation. Therefore, the amount of steam required for preventing carbon formation at 850 K is 1.5 times that of the methane amount.

At a higher temperature range, for example, 900 K-1100 K, it can be deduced that the ratio between steam and methane required is between 1.5 and 1.0, and decreases with increase of temperature. This can be seen in Figure 4-7 as the value of the 1.5 ratio increases sharply whilst the value for the S/C=1.0 ratio is still on the x-axis. The steam demand decreases with the temperature increasing at temperatures above 1150 K. The demand for the steam to methane ratio is between 1.0 and 0.5, but very close to 1.0, as shown in Figure 4-7.

4.4 Comparison

Figure 4-8 was deduced from Figure 4-7, thus there can be some minute deviations. However, in general, Figure 4-8 shows a similar pattern to Figure 4-1, as shown in dashed line here. By comparing Figure 4-1 and Figure 4-8, it can be seen that both methods are based on thermodynamic equilibrium thus the similarity of results is expected. However, the pre-equilibrium in the CA approach was presented in order to allow both methods 1 and 2 to examine the system under identical conditions. This stage is not required when the CA approach is applied in the practical occasions. These results show that the carbon activity method can be used to determine the carbon formation when all the methane cracking, Boudouard and reverse syngas formation reactions are considered simultaneously. Moreover, unlike the C-S EQ approach, the presence of carbon monoxide, carbon dioxide and hydrogen is allowed in the carbon activity method. This method also avoids the complex mathematical calculation. With only the concentrations and the equilibrium constants, the carbon activity is expected to be more useful in examining the carbon formation for operating SOFC systems in practice. After all, this method also gives some information on the margin by which the gas composition in question is removed from carbon formation conditions.

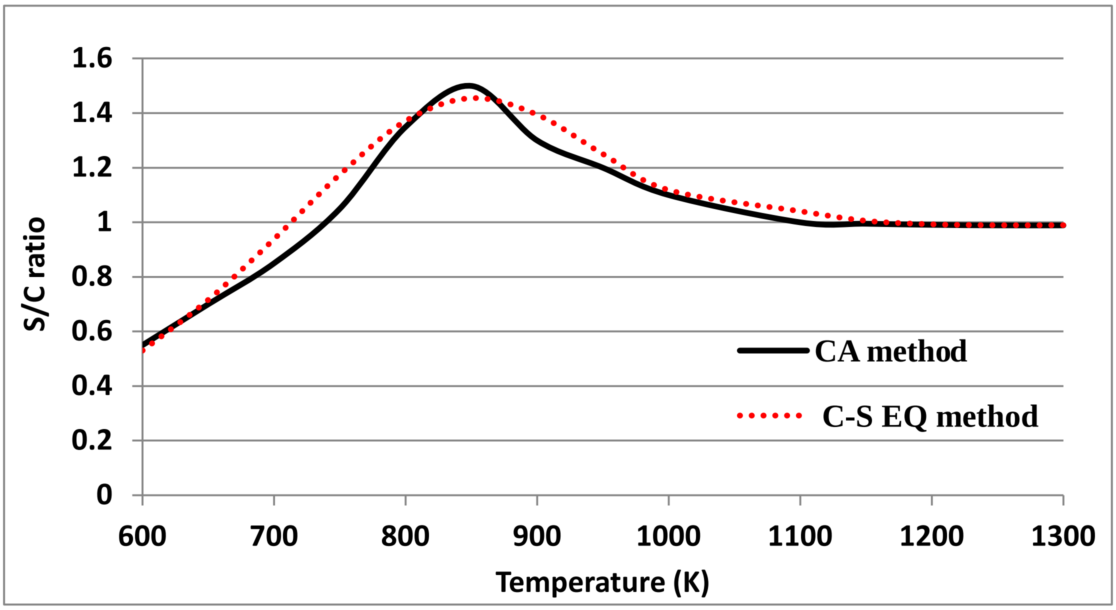

Figure 4-8 The minimal steam required for preventing carbon formation from the CA approach.

4.5 Hydrogen Production

For an SOFC system, the hydrogen partial pressure is crucial, as it directly affects the Nernst equation and the cell voltage. Figure 4-9 (a) and (b) show the hydrogen partial pressure for different S/C ratios and temperatures from Figure 4-2 to Figure 4-6.

From Figure 4-9 (a), it can be seen that higher S/C ratios lead to a lower hydrogen partial pressure. This is due to the residual steam in the system after reformation lowering the hydrogen gas partial pressure in the gas mixture. It is noteworthy that the highest S/C ratio tested, the S/C = 2.5 ratio, provides the lowest hydrogen partial pressure at temperatures above 900 K. This is because the high steam ratio provides more than enough steam for methane reforming, and thus the residual steam after reformation reduces the hydrogen partial pressure, as shown in Figure 4-6. As a result, S/C = 1.0 is expected to provide the SOFC system with better performance as at high open circuit voltage can be obtained from the high hydrogen partial pressure, as can be seen from the Nernst equation (Equation 3.30).

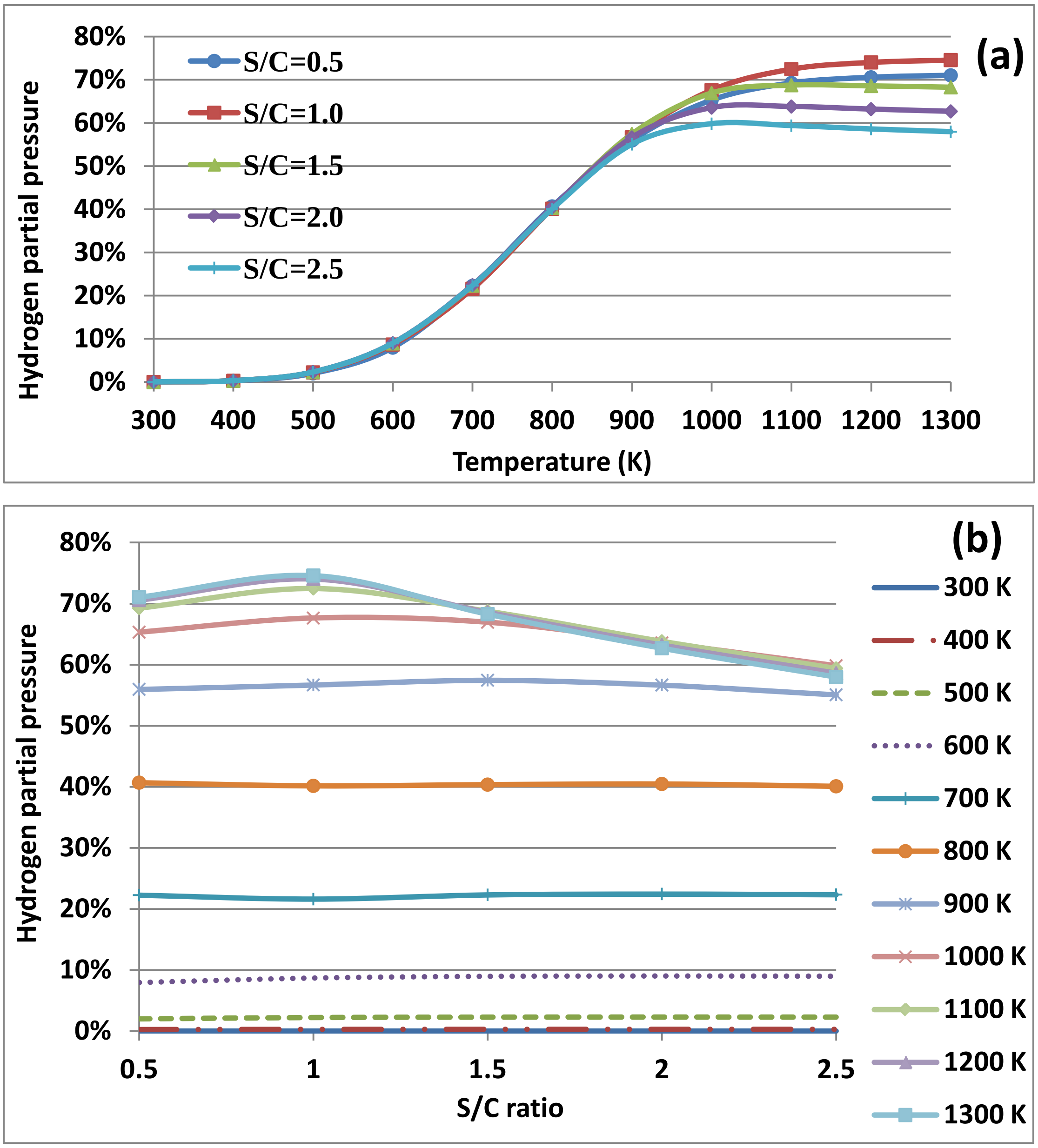

Figure 4-9 (a) (b) Hydrogen partial pressure at different S/C ratio and temperature.

Figure 4-9 (b) reveals that higher temperatures lead to higher hydrogen concentrations for S/C ratios blow 2.0. The results shown in this figure confirm that the S/C = 1.0 ratio gives peak hydrogen concentrations at temperatures above 1000 K. In addition, the results show that higher temperatures improve methane conversion at the 1.0 S/C ratio, and thus result in higher hydrogen concentrations. However, at higher S/C ratios (1.5, 2.0, and 2.5), the hydrogen partial pressures are little affected by the temperature when the temperature is above 900 K. This is due to the conversion of methane reaching completion by 900 K, such that further temperature increases have no further effect. For temperatures below 800 K, lower hydrogen concentration is obtained because methane is not completely reformed.

4.6 Chapter Review

This work examines the effect of operating temperature and steam to carbon ratios on carbon formation, using two different approaches. With a similar result, the peak steam demand around 1.5 S/C ratio occurs at 850 K and decreases with increasing temperature. An 1.2 ratio is required at 950 K, and only 1.0 of steam to methane ratio is required at temperatures above 1100 K to prevent carbon formation.

The C-S EQ method can only deal with the carbon formation within the system fed with methane and steam only. By contrast, the carbon activity method approach is free from this limitation. With the product of the carbon activities from methane cracking, Boudouard, and especially the reverse syngas formation reactions, it can be applied to a kinetic system that allows the presence of carbon monoxide, carbon dioxide and hydrogen additional to the fuel steam.

To conclude, the C-S EQ approach can only be used for pure steam methane reforming and at the beginning of the reactions. The carbon activities used in the CA approach can be applied during the reaction, where the C-S EQ method failed to predict the formation of carbon, without the pre-equilibrium procedure.

Chapter 5 Combined Steam and Dry Methane Reforming

5.1 Introduction

As discussed in the previous chapters, methane can be reformed through steam (Equation 2.21) and dry reforming (Equation 2.23). In the anode exhaust gas, both water and carbon dioxide can be found as they are products of hydrogen and carbon monoxide oxidation (Equation 3.21 and Equation 3.22). The two gases are then recycled and mixed with the methane from the inlet, to produce hydrogen for the SOFC. In order to investigate the cell performance, a solid understanding of the interactions of various reforming reactions is necessary.

In this session, both thermodynamic equilibrium modelling and practical kinetic experiments for the combined steam and dry reforming of methane were conducted and the results are compared. Different methane-water-carbon dioxide ratios were used in both modelling and experimental works, as listed in Table 5.1. Additional, the pressure were set at 1 atm and the reaction temperature was 1023 K in both works.

Table 5.1 Parameters used for methane reforming.

	CH_4 (sccm)	H_2O (sccm)	CO_2 (sccm)	H_2O/C	O/C
Case 1	25	25	0	1	1
Case 2	25	37.5	0	1.5	1.5
Case 3	25	0	25	0	1
Case 4	25	0	37.5	0	1.2
Case 5	25	0	50	0	1.333
Case 6	50	50	50	0.5	1.5
Case 7	25	25	25	0.5	1.5
Case 8	25	50	50	0.66	2
Case 9	25	25	37.5	0.4	1.6
Case 10	25	37.5	25	1.5	1.75

In Table 5.1, the CH_4, and CO_2 columns represents the flow rates of each gas in sccm. However, water is in liquid form at room temperature, so the unit for H_2O is g min^{-1}. The H_2O/C column is the steam molecule to carbon atom ratio based on the fuel input in each case. The O/C column indicates the atomic ratio between oxygen to carbon atoms. These two ratios are for the further discussions.

5.2 Modelling

5.2.1 Introduction

In this section, the NASA CEA software [145] was used to calculate gas concentrations at thermodynamic equilibrium concentrations for different ratios among methane, water and carbon dioxide.

Different amounts of methane, water and carbon dioxide were given, for various molecular ratios, as the initial values to the software. However, the testing without the catalyst was not conducted as this work was aiming to simulate the methane reforming reactions on the anode surface. As a result, it is assumed that no reforming reactions occur if catalyst is not present in this work. The concentration of each gas at equilibrium was calculated by determining the minimised Gibbs free energy in the CEA modelling software. The results are presented in Figure 5-1 and Figure 5-2 in the next session.

5.2.2 Results and Discussions

Methane reforming

Figure 5-1 shows the gas composition at equilibrium for different cases. Case 1 and 2 focus on the different ratios between methane and water, 1.0 and 1.5. The decrease of residual methane concentration, from 3.72% in case 1 down to 1.28% in case 2, implies the methane is reformed more completely with increasing water concentration. However, the increase in residual water, from 3.91% to 9.39%, due to the increasing steam to methane ratio at the beginning, also causes a decrease in the hydrogen concentration, from 69.23% in case 1, down to 67.82% in case 2. Meanwhile, the formation of solid carbon is also eliminated by increasing the water content. Carbon is formed only in case 1 among these three cases. Case 2 is carbon free at equilibrium.

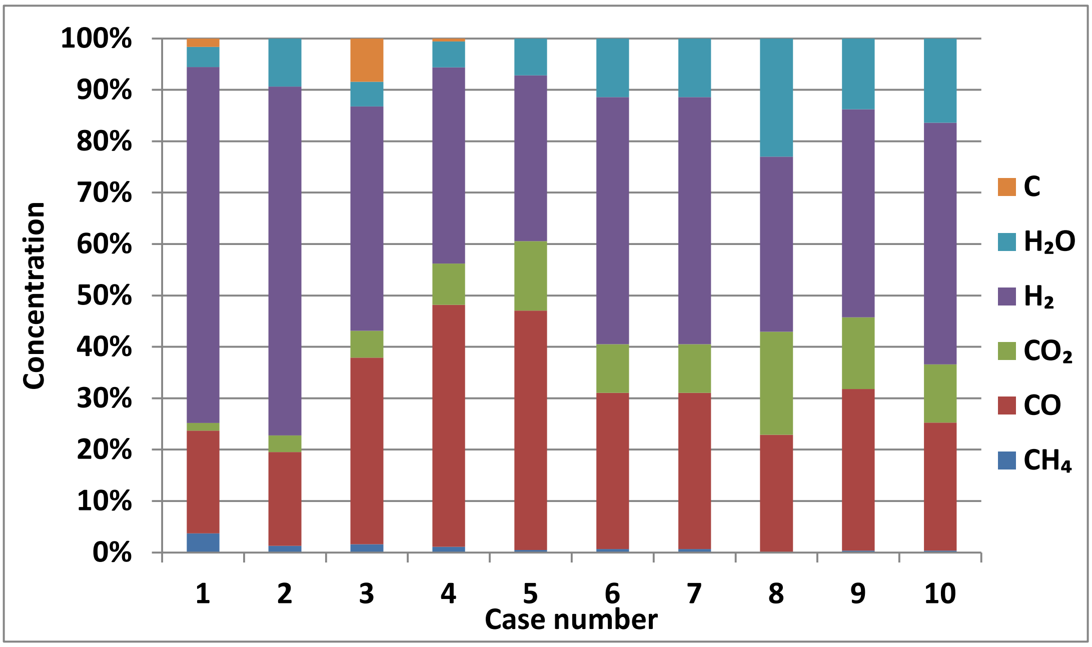

Figure 5-1 Results from CEA modelling for different scenarios with carbon and water.

Similarly, different ratios between carbon dioxide and methane, ranging from 1.0, 1.5

to 2.0, were also investigated in cases 3 to 5. Case 4 has 8.44% of carbon formed at equilibrium due to the residual methane inside the system. When comparing case 1 and case 3, both have 1 in the O/C ratio; however, the higher hydrogen partial pressure in case 1 lowers the activity of the methane cracking reaction. As a result, even though the methane partial pressure in case 1 is higher than the pressure in case 3, case 3 has more solid carbon formed than case 1. The carbon concentration then decreases to 0.6% for case 4, when the carbon dioxide to methane ratio increases from 1.0 to 1.5. Comparing this result with case 2, which has the same ratio between water and methane, case 4 has an extra carbon atom, supplied in the carbon dioxide molecule. This leads to a lower oxygen to carbon ratio, down to 1.2 from 1.5 in case 2. As a result, carbon formation is thermodynamically possible. In Case 5, which has a 1.33 oxygen to carbon ratio, the system can prevent carbon formation completely. However, the increase in carbon dioxide concentration also decreases the hydrogen partial pressure. When comparing steam methane reforming (cases 1 and 2) with dry reforming (cases 4, 5, and 6), the former cases have significantly higher hydrogen yield than the latter. This is because with DR, there is no water inside the system at the beginning for providing extra hydrogen molecules like in cases 1 and 2. Additionally, water also provides hydrogen during the reforming but carbon dioxide only consists of carbon and oxygen atoms. Moreover, the produced hydrogen can react with the existed carbon dioxide and form water and carbon monoxide through the reversed WGS. However, as discussed previously, carbon monoxide can theoretically be oxidised inside SOFCs and produces electricity, the oxidation rate is much slower than being reformed, so the effect of carbon monoxide on the output voltage is not discussed here.

Cases 6 to 10 examined how the reactions interact and compete with each other. The two species, water and carbon dioxide both exist in the system simultaneously, competing with each other to react with methane.

Cases 6 and 7 were used to demonstrate that the thermodynamic equilibrium is not affected by the different flow rates. The ratio between methane, water and carbon dioxide is 1:1:1 and 2:2:2. The results showed that the thermodynamic equilibrium is a stoichiometric based calculation, it is only related to the ratios among the atoms. As a result, despite the fact that case 6 has twice the flow rate in each gas, the individual equilibrium concentration is the same as in case 7. However, this is the viewpoint of thermodynamic equilibrium; the reforming is highly affected by the surrounding conditions which will be discussed in the next section.

When comparing case 6 with the pure steam reforming (cases 1 and 2) and dry reforming (cases 3 to 5), the methane conversion is better than the 1.0 and 1.5 ratio, and only slightly less than the 2.0 ratio. This suggests that, in general, a higher O/C ratio improves the methane conversion. The residual methane is 0.63% in case 6, compared with 1.28% and 1.12% in cases 2 and 4 (the 1.5 ratio for steam and dry reforming), and the 0.52% and 0.47% in cases 3 and 6 (the 2.0 ratio).

Hydrogen Yield

From the hydrogen yield perspective, the combined reforming reaction has a better hydrogen production (48.07%) than all ratios of dry reforming (43.61%, 38.18% and 32.28%), but lower hydrogen yield than all steam reforming ratios (69.23% and 67.82%). This is because steam contains hydrogen molecules which are released through the reforming reactions. The ratios of the hydrogen atom to carbon atom are 6 and 7 in cases 1 and 2. On the other hand, they are only 2, 1.6 and 1.333 in cases 3, 4 and 5. For cases 6 and 7, the ratio is 3. As a result, the steam methane reforming has a higher hydrogen yield than the combined reforming in case 6.

In case 8, the amount of water and carbon dioxide were doubled, whilst methane remained the same as in case 6. The results show a better methane conversion (0.08%

residual); however, the hydrogen partial pressure is only 34.11%, which is lower than the 48.07% in case 6. Despite the higher concentrations of water and carbon dioxide actually improving the methane conversion, the residual gases in fact lower the hydrogen concentration.

Cases 9 and 10 show a similar performance with regard to methane conversion (0.32% and 0.33% of methane left individually), when the water to carbon dioxide is 1:1.5 (case 9) and 1.5:1 (case 10). Nevertheless, the higher steam concentration in case 10 leads to a better hydrogen yield (46.97%) than in case 9 (40.47%) since the water also contributes hydrogen molecules, as mentioned before.

Carbon Formation

From the carbon deposition perspective, only cases 1 (1.0 steam reforming), 3 and 4 (dry reforming, 1.0 and 1.5 ratio) have carbon deposition at equilibrium. It can be easily observed that the system can suffer from carbon deposition when the oxygen to carbon ratio is lower than 1.3. For steam reforming, the water molecule contains one oxygen atom, whilst the carbon dioxide molecule has a carbon atom and an oxygen molecule. As a result, the 1.5 ratio of steam reforming has a 1.5 O/C ratio, whilst it is just 1.2 in the dry reforming. The lower O/C ratio leads to carbon deposition in cases

3 and 4. For the rest of the cases, the O/C ratios are above 1.3, and therefore free from the formation of solid carbon.

Results for Comparing with the Experimental

In order to prepare these results for experimental verification by the results from gas chromatography and also taking the point of view of fuel gas production, water and solid carbon need to be removed from the balance. Technically, this is easily done.

Figure 5-2 shows the results obtained by removing the water and solid carbon at equilibrium because in this work, steam was condensed before the reformed gas was fed into the GC. For the steam reforming scenarios (cases 1 and 2), the higher the S/C ratio, the better the methane conversion rate, and therefore the hydrogen yield. This is different from the results in Figure 5-1, and it is due to the residual water is removed, then the hydrogen concentration increases.

For the dry reforming cases (cases 3, 4 and 5), the results are quite similar in both figures, as the water is produced during the reactions, not given at the beginning. As a result, the removal of water has an insignificant effect on the species concentrations.

Cases 6 and 7 have a similar pattern in both figures, but all elements share a higher concentration when the water is removed. Moreover, these two scenarios have the same ratios among methane, water and carbon dioxide (1:1:1), and thus the gas composition should be the same from the thermodynamic equilibrium viewpoint.

The gas concentrations increase when the water is removed in cases 8, 9, and 10, as there was a certain amount of water left in the system at equilibrium. Methane was almost completely reformed as mentioned before. Hydrogen increases from 44.27% in case 8, to 56.2% in case 10. This is also because the concentration is affected by residual carbon dioxide in the system. However, a noteworthy issue is that the carbon monoxide peaks at case 9, with an input ratio of 1:1:1.5 of methane to water to carbon dioxide. This can be explained by the fact that both SMR and DR are high temperature favoured reactions thus they convert methane into hydrogen and carbon monoxide at this experimental temperature. On the other hand, the WGS favours lower temperatures thus it is not active at 750 ℃. Meanwhile, the input steam is less in case 9 than in cases 8 and 10, thus it is hard to shift the WGS reaction forwards to convert carbon monoxide into carbon dioxide and hydrogen.

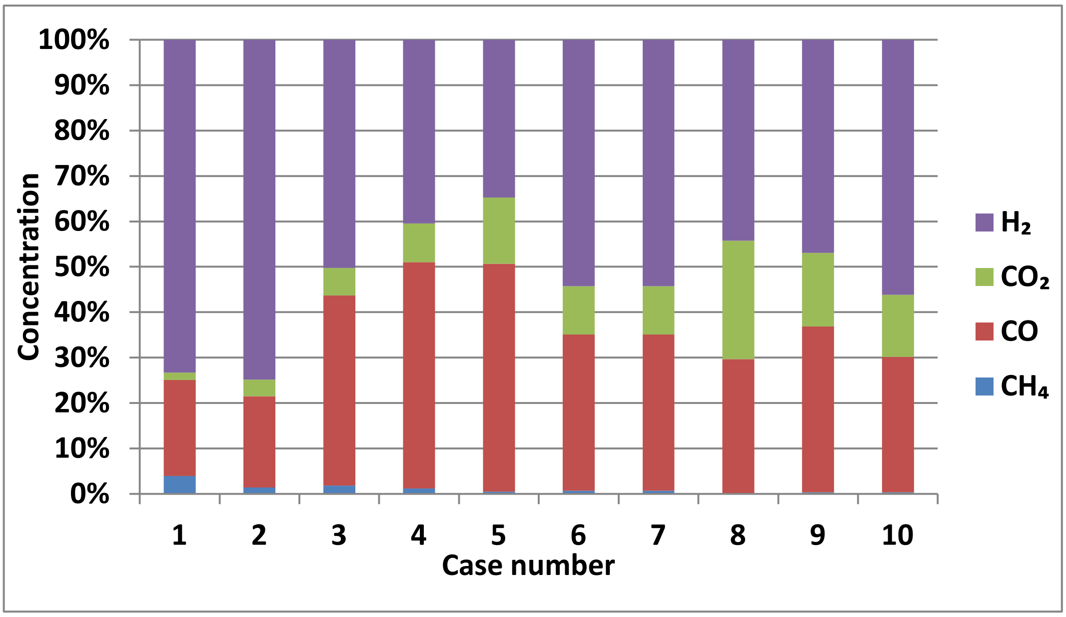

Figure 5-2 Results from CEA modelling for different scenarios omitting carbon and water.

5.3 Experimental Verification

5.3.1 Introduction

Combined methane steam and dry reforming was conducted experimentally and results are presented in this section. Methane was mixed with steam and carbon dioxide under different ratios. By using an SOFC half-cell (anode and electrolyte) as the catalyst, the aim of this experiment was to investigate the methane internal reforming with recycled anode off-gas and how it affects the cell performance and the formation of solid carbon.

Helium, and other non-reactive gases, were not added for keeping the same total flow rate in each case. The reason was that this experiment was designed to simulate the reforming reactions inside the cell with the AOGR gases. In the case of AOGR, the flow rate is affected by two factors: 1) the recycling rate and, 2) the cell operation status such as the fuel utilisation, as different reactions can produce different amounts of gases. As a result, the amount of the total gas flow rate is not constant. Additionally, this experiment was also conducted to validate the modelling based on the thermodynamic equilibrium. In the model the reactions theoretically are not affected by the flow rate.

The experimental results would then be compared to the thermodynamic modelling results previously presented.

5.3.2 Methane Reforming

This section presents the results from the different experimental conditions listed in Table 5.1. The 10 cases are divided into four sections, namely, steam reforming, dry reforming, the effect of flow rate, and combined steam and dry reforming.

Steam Reforming

Figure 5-3 and Figure 5-4 present results of steam methane reforming with a steam to methane molar ratio of 1.0 and 1.5, respectively (case 1 and 2 in Table 5.1). During the reaction in case 1 (as shown in Figure 5-3), the hydrogen production slowly increased to around 60%. The residual methane partial pressure is around 33%, with the carbon monoxide and hydrogen partial pressures are around 9% and 0.6%, respectively. After 2 hours, the reaction was relatively stable. It can be seen that higher steam concentrations in Figure 5-4 diminished the methane reforming performance. The GC froze twice during the case 2 experiment. The residual methane concentration increased from 33% to 60%; meanwhile, the hydrogen partial pressure decreased from 59% down to 34%. With higher steam content the reaction needed almost 4 hour for stabilisation (Figure 5-4). These results differ from the equilibrium model results for several reasons. First, the higher flow rate used in the experiments, increased the gas flow velocity and reduced the reaction time. This led to a further distance from the equilibrium and caused an unstable reforming result. Additionally, the higher steam partial pressure also decreased the methane partial pressure, thus lowering the possibility of methane being absorbed by the catalyst.

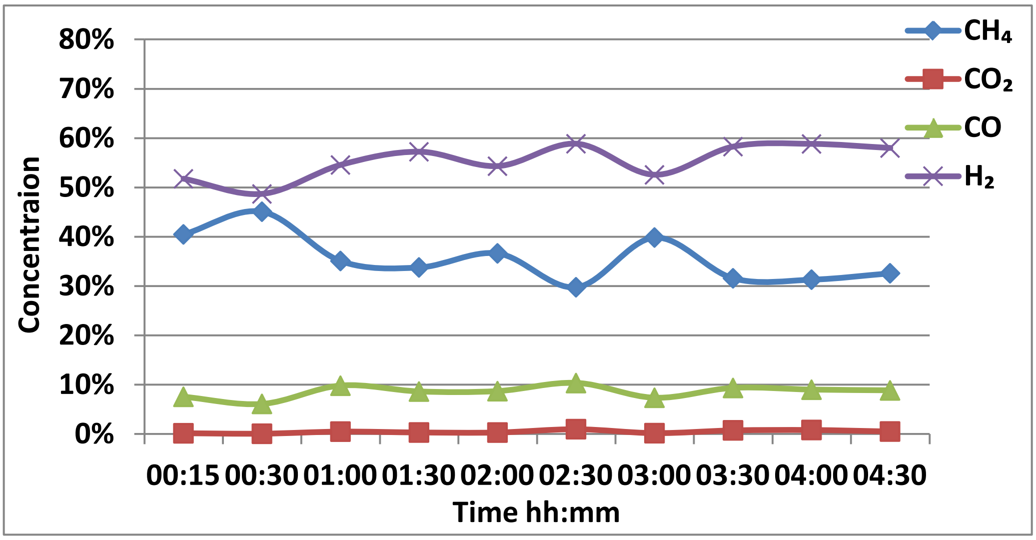

Figure 5-3 The reaction results from case 1 (CH_4:H_2O = 1:1).

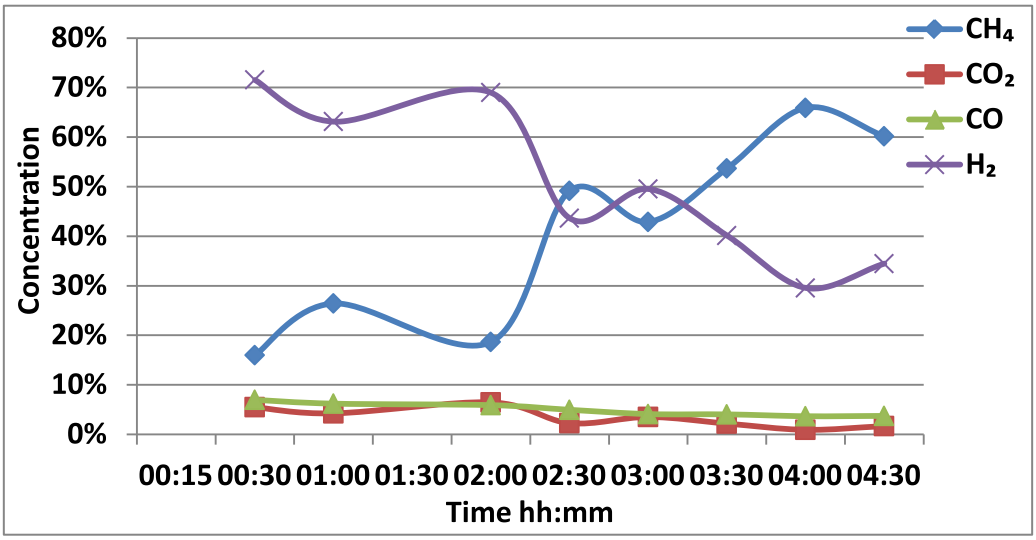

Figure 5-4 The reaction results from case 2 (CH_4:H_2O = 1:1.5).

Dry Reforming

The dry reforming results, shown in Figure 5-5, Figure 5-6, and Figure 5-7 (case 3, 4, and 5 in Table 5.1), depict carbon dioxide mixed with methane at the different ratios of 1.0, 1.5 and 2.0. The results from dry reforming reactions are relatively stable than the results from steam reforming reactions. The hydrogen concentration decreased from 43%, 38% down to 35%, respectively, with increasing carbon dioxide partial pressure. Meanwhile, the carbon monoxide, which is expected to be produced at the same ratio as hydrogen gas, shared a similar partial pressure as hydrogen. The carbon monoxide concentrations were 38%, 37%, and 35%, in cases 3, 4, and 5. This is due to the short reaction time in the practical experiments, in which the time only allows the gases to react through the DR, instead of other reactions such as the reversed SMR and the reversed WGS reactions. This can also be seen from the partial pressures of the methane and carbon dioxide in all three cases: the ratio between these two concentrations remained in similar ratios as the initial given ratios throughout the experiment period. Additionally, the higher carbon dioxide to methane ratios led to a higher residual carbon dioxide partial pressure after reforming, and thus lowered the hydrogen concentration. Both methane and carbon dioxide gases were having higher concentrations in the practical experiment than in the modelling results. This suggested that the practical experiment was far from the thermodynamic equilibrium state. However, the experimental results supported the modelling results in general.

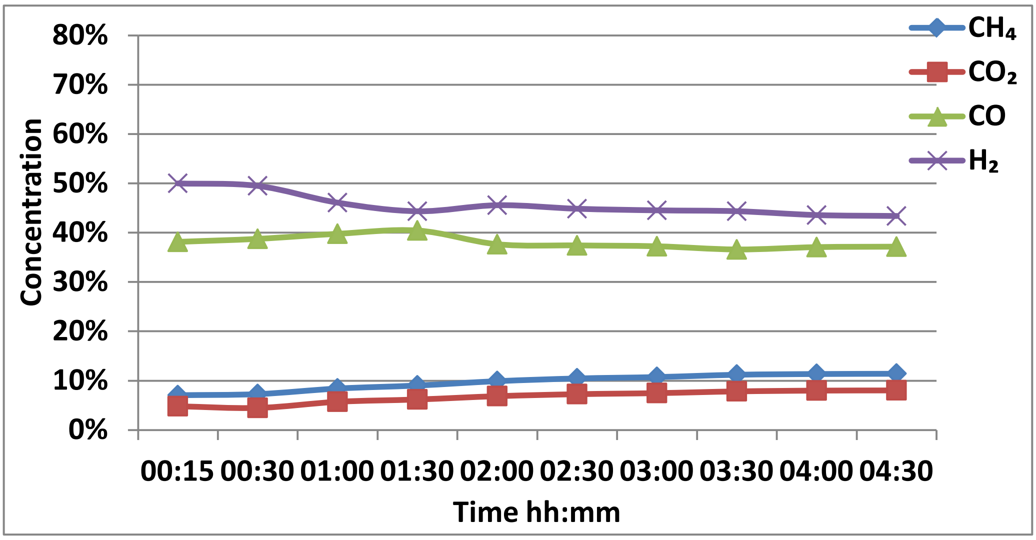

Figure 5-5 The reaction results from case 3 (CH_4:CO_2 = 1:1).

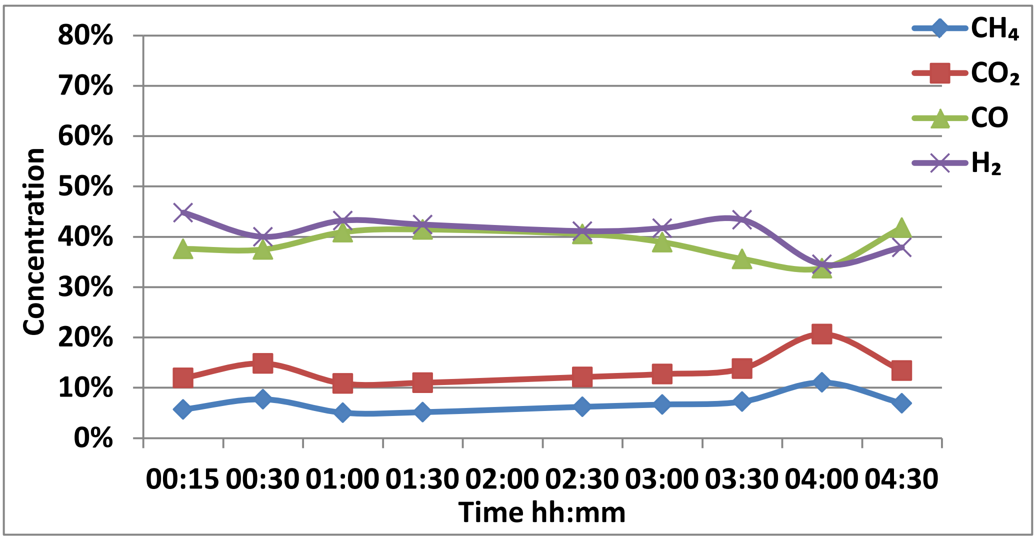

Figure 5-6 The reaction results from case 4 (CH_4:CO_2 = 1:1.5).

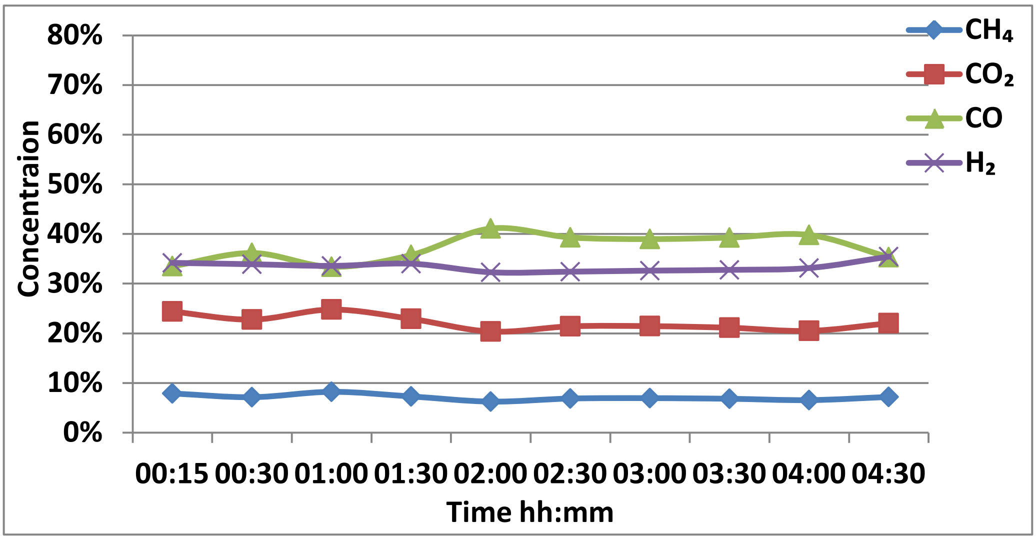

Figure 5-7 The reaction results from case 5 (CH_4:CO_2 = 1:2).

Figure 5-8 to Figure 5-12 present results from mixed steam and dry reforming (sometimes called bi-reforming). Cases 6 and 7 in Table 5.1 were used to test the relationship between the flow rates and reforming reactions, as both cases were given the same ratios among methane, steam, and carbon dioxide. Therefore cases 6 and 7 were expected to have the same results from a thermodynamic viewpoint, as reported in the modelling work. This is because they have the same molar ratios among methane, water and carbon dioxide (1:1:1). However, during the practical experiments, the kinetic behaviour dominated the results. Cases 8, 9, and 10 were used for the investigation of the composition between stem and carbon dioxide for reacting the methane.

The Effect of Flow Rate

The flow rate can affect the reaction process significantly, as shown Figure 5-8 and Figure 5-9. It can be seen that case 6, which has a higher flow rate, has a worse reforming performance. The hydrogen partial pressures was fluctuating between 5% to 20% together with the reforming by-product, carbon monoxide, has partial pressure ranging from 3% to 18%. Moreover, the methane and carbon dioxide concentrations remained relatively high, between 50% and 30%. This phenomenon is different in case 7, in which all initial flow rates were halved. The hydrogen concentration (around 50%) were much higher than the carbon monoxide concentration (around 25%), which implies that steam reforming was dominating the reactions as more hydrogen was produced than carbon monoxide. This is due to the lower flow rates providing a longer residence time of the gas reacting with the catalysts. A noteworthy issues is that in both cases 6 and 7, the carbon dioxide concentrations were higher than the methane concentrations, although they were given in the same amount. This suggests that steam has a significant effect on the combined reforming. Additional, with the lower flow rate in case 7, the steam was dominating the reactions, although carbon dioxide was also given to the system. Finally, the results of the case 7 were closer to the modelling results presented before than the results from the case 6, as the flow rate of all gases were halved. A reduced flow rate provided more time for the fuel to react with the catalyst and thus the results were closer to the equilibrium status, as shown in Figure 5-8 and Figure 5-9. This is because methane cracks down into solid carbon and gaseous hydrogen firstly in the reforming process. The carbon is then removed from the catalyst by the carbon dioxide or steam in the system. As a result, if the reaction time is insufficient, the second stage of reforming process is unable to carry out and thus causes carbon deposition.

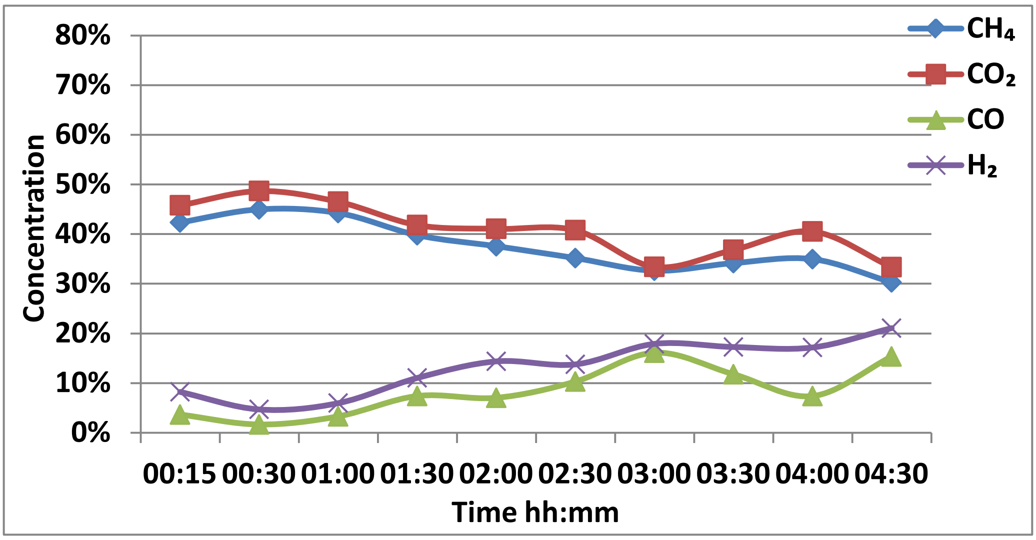

Figure 5-8 the reaction results from case 7 (CH_4:H_2O:CO_2 = 2:2:2).

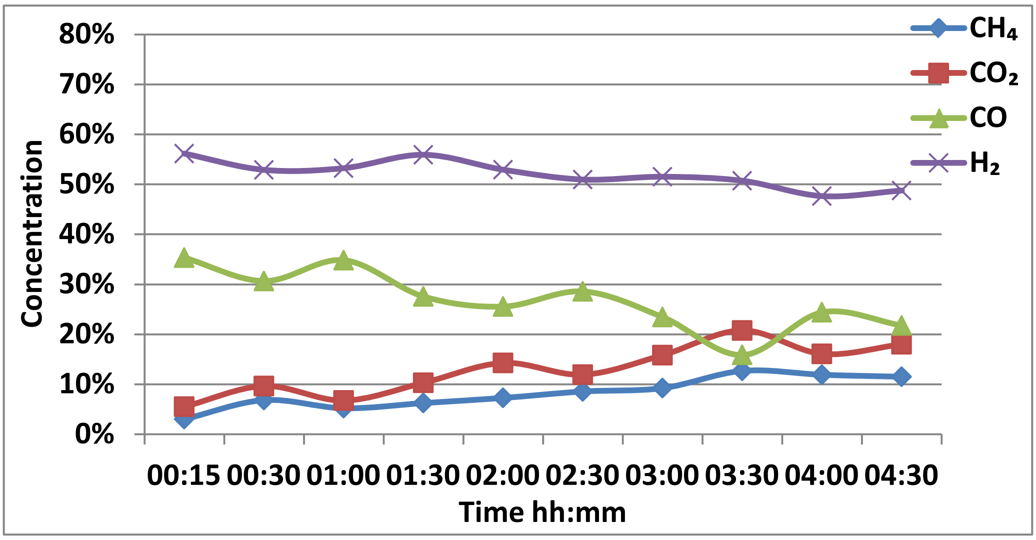

Figure 5-9 the reaction results from case 8 (CH_4:H_2O:CO_2 = 1:1:1).

Combined Steam and Dry Reforming

In Figure 5-10 to Figure 5-12 (case 8, 9, and 10 in Table 5.1) results are presented from the combined steam and dry methane reforming at different ratios between methane, water and carbon dioxide. The residual methane concentration in the case 8 was higher than in cases 9 and 10. This was also affected by the total flow rate as discussed before. The increased ratios of water and carbon dioxide to methane increased the flow velocity, and thus lowered the methane partial pressure and the reaction time for methane to be adsorbed onto the catalyst. Despite the fact that the modelling results showed a more complete conversion of methane in case 8 (0.11% methane concentration at equilibrium) than in any other scenario, the practical experiment results were dominated by the kinetic mechanisms.

The residual methane concentration was similar in cases 9 and 10 (around 10%) because these two cases had the same flow rate, and also similar O/C ratio (1.6 and 1.75 respectively). However, there was significant difference in hydrogen production, around 40% in the case 10 against 50% in case 10. This is because the higher steam ratio released more hydrogen molecules, as discussed before. Additionally, the results present only the dry components. The change of the water concentration could not be observed. For the case 9, the higher concentration of carbon dioxide gas was competing with the steam to reform the methane, thus producing carbon monoxide and hydrogen, leading to a higher residual carbon dioxide concentration. It is also possible that higher carbon dioxide concentration shifted the WGS reaction towards reactants. This could explain the difference in hydrogen concentration, but similar residual methane concentrations in cases 9 and 10.

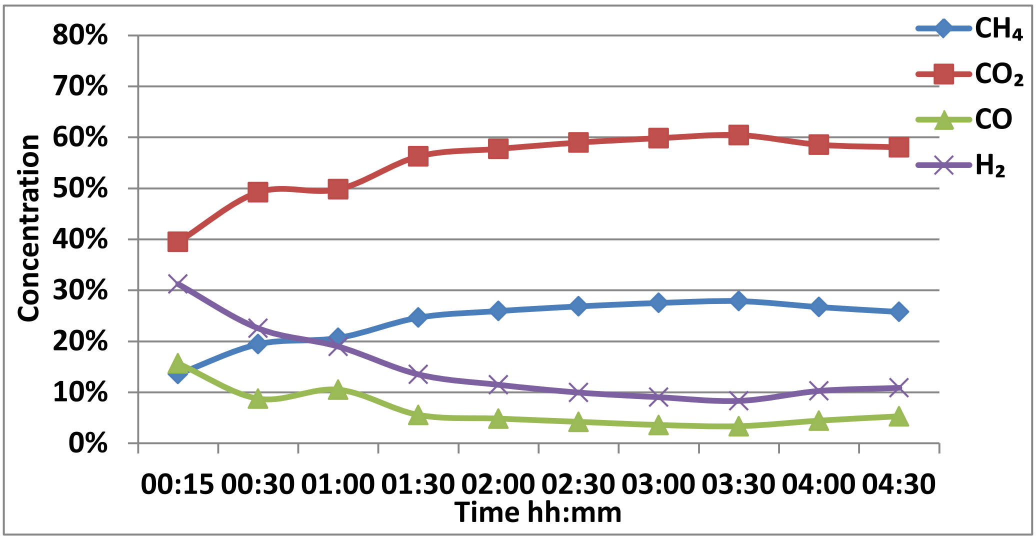

Figure 5-10 The reaction results from case 8 (CH_4:H_2O:CO_2 = 1:2:2).

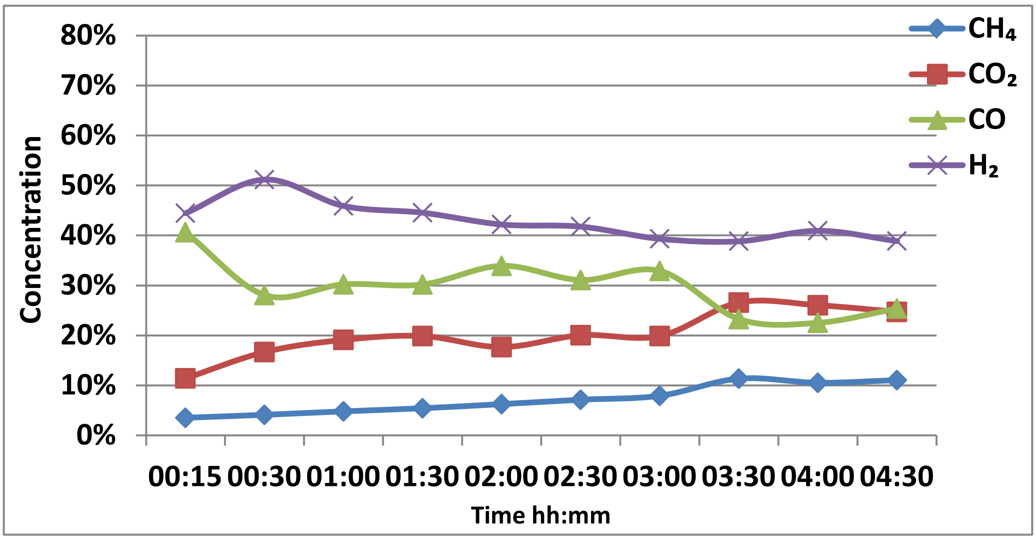

Figure 5-11 The reaction results from case 9 (CH_4:H_2O:CO_2 = 1:1:1.5).

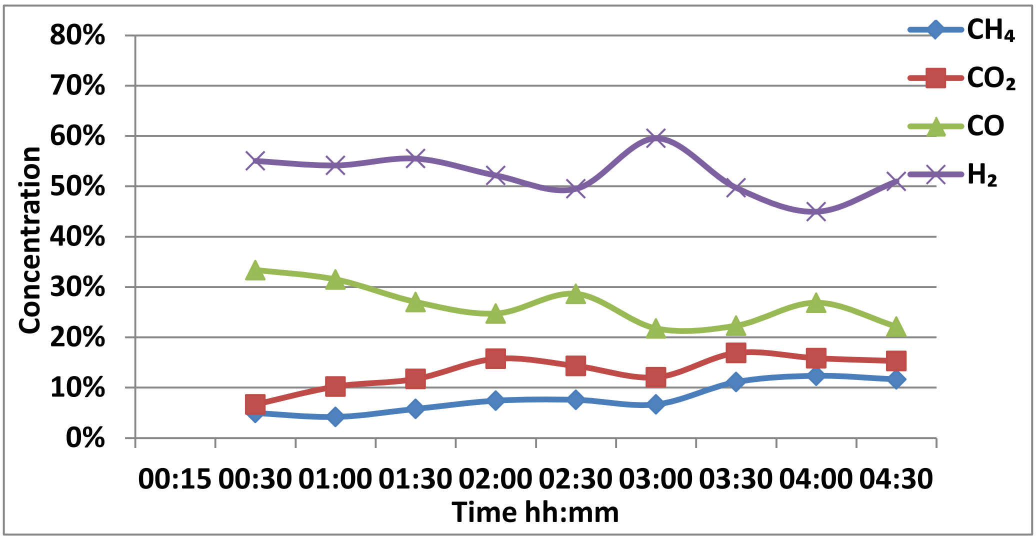

Figure 5-12 The reaction results from case 10 (CH_4:H_2O:CO_2 = 1:1.5:1).

5.3.3 Carbon Formation

Thermogravimetric Analysis

Figure 5-13 presents the results from the TGA for examining the carbon formation on the catalyst during the reforming reactions. An increase in weight can already be observed due to the oxidation of metallic nickel. The unused catalyst was first reduced and then oxidised under the same conditions as all other cases to measure the weight change from the oxidation of nickel metal to nickel oxide, which can be used as a reference. The theory is that when being oxidised, the carbon forms carbon dioxide and escapes to the atmosphere, reducing the weight; meanwhile, the weight also increases due to the oxidation of metallic nickel. As a result, the increase in weight from the carbon and nickel mixture oxidation will be less than the one from pure nickel oxidation. The weight change in percentage against the reference was then turned into the numerical data, as shown in Figure 5-14, for comparing with the TPO results.

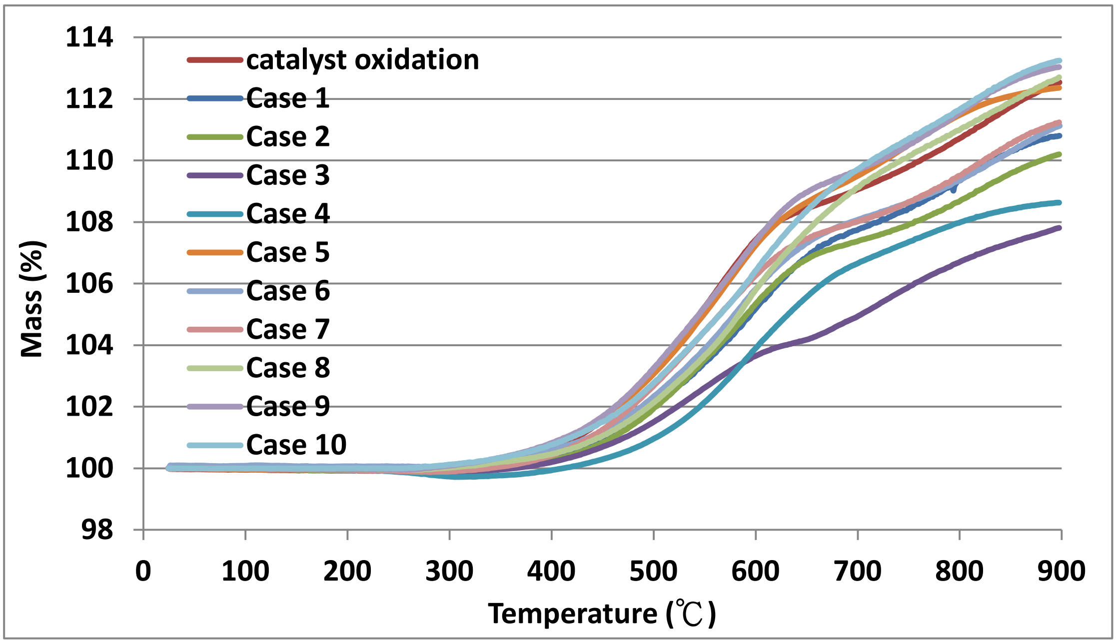

Figure 5-13 The TGA results of all the cases listed in Table 5.1 (p.111).

The highest increase in weight was observed in cases 8 to 10. Within the measurement error, the weight of these samples follow the trend of the reference. The reason why the cases 8, 9, and 10 have a higher weight increase was because the oxidation level. For the pure catalyst oxidation used as reference here, the sample only experienced a short period to reduction. The system was heated to 900 ℃ and then cooled down directly. In comparison, those samples used for the reforming experiments experienced an hour of reduction process under pure hydrogen and 750℃. With the highest O/C ratio (2.0, 1.6, 1.75, respectively) among all cases, these three combined methane reforming scenarios suggest that carbon formation was completely prevented.

The pure dry methane reforming, case 5 that has the ratio of 2 between carbon dioxide and methane, shows a similar increase percentage in weight as the reference case. This suggests that with the value of 1.33 in its O/C ratio, this condition was able to prevent the formation of solid carbon.

In case 7, 6 and 1, it can be seen that the weight increase percentage is lower than the above cases. Case 7 and 6, which were used to test how the flow rate affects the reforming reactions, and, thus had the same O/C ratio of 1.5, showed a similar result from the TGA. Case 1 is in the same region as case 7 and 6. The results of these three cases show the formation of carbon from the methane reforming reactions.

The lowest weight increase group, which consists of case 2, 4, and, 3 implies a significant amount of solid carbon formed. For case 2, despite having an O/C ratio of 1.5, it was observed that more carbon formed than in case 6 or 7 mentioned previously.

This case, which has an 1.5 ratio between water and methane, even had a worse performance than the O/C = 1.0 ratio in case 1.

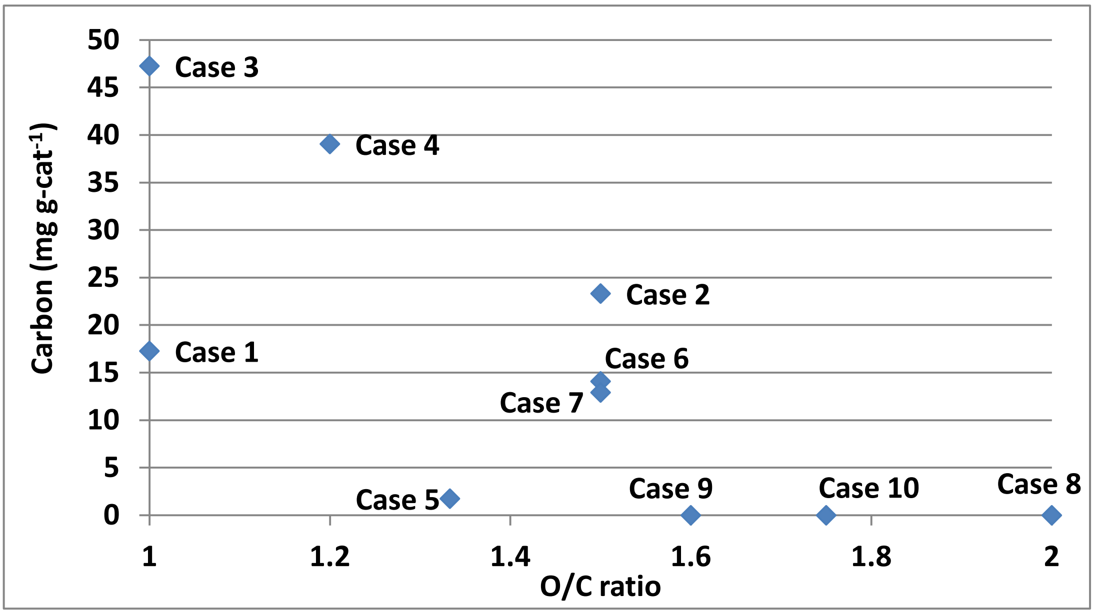

Figure 5-14 The amount of carbon formed from TGA against the O/C ratio from all the cases listed in Table 5.1 (p.111).

From this experiment, it could be seen that combined reforming with water and carbon dioxide performed better than any other cases, which could be due to their high O/C ratios. In general, the higher the O/C ratio, the less carbon formed, as shown in Figure 5-14. A noteworthy issue is that the pure methane dry reforming has a better performance over the pure steam methane reforming. This significantly differs from the results from the thermodynamic equilibrium modelling shown in the previous sessions. The reason could be that : 1) the experiment was far from the equilibrium state, and, 2) the experiment was highly dependent on kinetic interactions. Unlike the equilibrium modelling, the reactants had limited time for the reaction to occur. The time was insufficient for the methane to fully react on the catalyst.

Temperature Programmed Oxidation

The results in Figure 5-15 show the amount of solid carbon formed on the catalyst examined by the TPO method. The TPO results of cases 10 and 11 are missing due to the failure of MS. All conditions were suffering from the formation of solid carbon. For methane steam reforming, carbon was found in both cases 1 and 2. Moreover, the carbon formed in the case 2, 29.68 mg g-cat^{-1} was more than the amount of 14.85 mg g-cat^{-1} in the case 1, which supports the TGA results. The higher steam concentration lowers the methane reforming rate and increases the amount of solid carbon. This was different from the equilibrium modelling results, which suggests that the 1.5 O/C ratio should be free from this problem. The high adsorption enthalpy of water causes this problem, because this means a longer reaction time but the reaction time is limited in the experiment, which is also supported by Wang et al. [139]. This also causes the lower reforming performance in the kinetic modelling results presented in the next chapter.

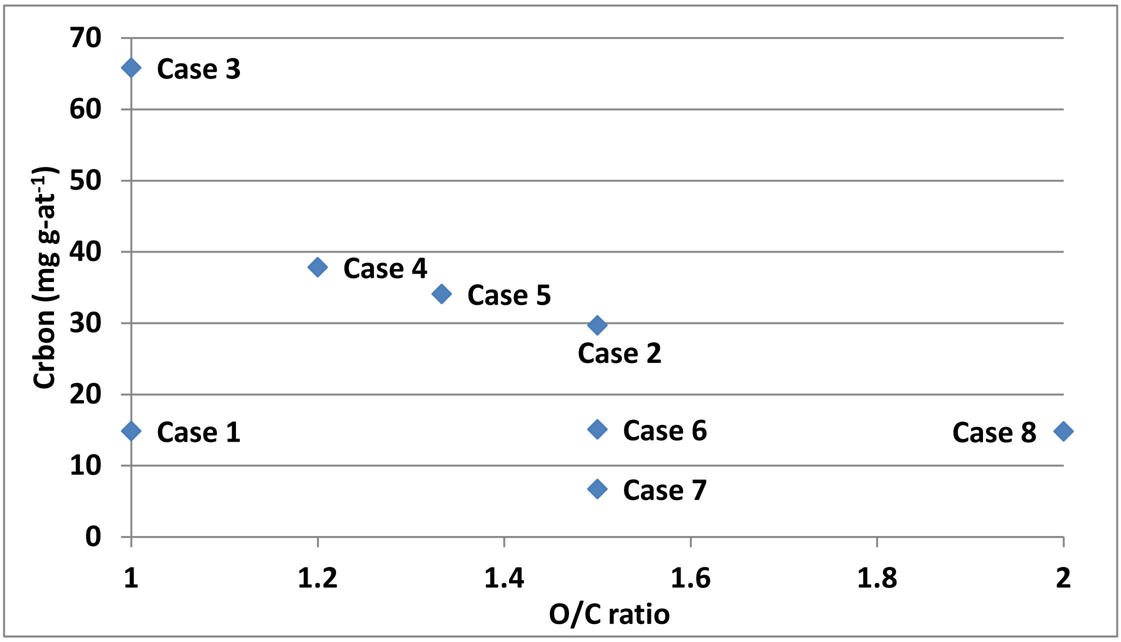

Figure 5-15 The amount of carbon formed from TPO against the O/C ratio from all the cases listed in Table 5.1 (p.111).

Cases 3, 4 and, 5 show that the carbon formation was decreased with increasing O/C ratio. The amount of 65.83 mg g-cat^{-1} was found in case 3, which has only 1.0 in its O/C ratio, and has the largest carbon formed among all the cases. This phenomenon was improved with the increase of the O/C ratio by giving more carbon dioxide gases. There were 37.84 and 34.09 mg g-cat^{-1} of carbon were formed in cases 4 and 5, respectively (O/C = 1.2 and 1.33, respectively).

Cases 6 and 7, which were used to examine how the flow rate affects the reforming process, showed that gas flow rate had effect on carbon formation. The higher flow rate in the case 6 lowered the methane conversion. The carbon can theoretically removed by water through the SF reaction, but the high flow velocity leads to the insufficient time for this reaction. Case 7, by comparison, had the same ratio among methane, water, and carbon dioxide but the flow rates were halved in each species. It was found to have less carbon formed.

The case 8, which had the highest O/C ratio among all scenarios, still had 14.81 mg g-cat^{-1} formed. This amount was similar to the 15.09 mg g-cat^{-1} in the case 6 and 14.85 mg g-cat^{-1} in the case 1, although both cases had O/C ratios of 1.5 and 1, respectively. Again, water had a significant role in these three cases. The higher concentration of steam lowered the reforming performance and the ability to prevent the carbon formation. The higher amount of carbon was found in the case 2, which had a 1.5 ratio between steam and methane, as shown in Figure 5-15.

In general, in steam reforming, the O/C ratio was in a positive correlation to the amount of deposited carbon, and higher O/C ratios lead to more deposited carbon. Dry reforming showed negative correlation. The increasing O/C ratio decreased the amount of deposited coke.

It can been seen from Figure 5-15 that the relationship between the O/C ratio and the amount of carbon formed is insignificant, unlike the thermodynamic modelling results. This is due to the fact that practical reforming is more related to the kinetic interaction, the results can be affected by many issues such as the flow rate, adsorption enthalpy of the gases.

5.3.4 TGA and TPO Comparison

Figure 5-16 shows the carbon formation from the TPO and the TGA analysis. The black line here shows that the TGA and TPO results agree with each other in the amount of carbon. In general, the higher the O/C ratio, the less the carbon formed, apart from the pure steam reforming. This was obvious in case 8, when the combined reforming was applied. Case 8 had only trace of carbon formed. In the steam reforming reactions, increasing the amount of steam resulted in higher coke deposition, due to the high adsorption enthalpy of steam. In the dry reforming reaction, the highest coke formation was found when the O/C ratios are 1.2 and 1.0. Therefore, case 4 with O/C ratio 1.2 was optimal for DR from the methane conversion point of view, but the catalyst life would be significantly reduced due to significant coke deposition in that case. Additionally, it could also be seen that for pure steam or dry reforming, the higher flow rate lowered the ability in preventing carbon formation. This was due to the limited reaction time for the steam or carbon dioxide to remove the carbon atom from the catalyst.

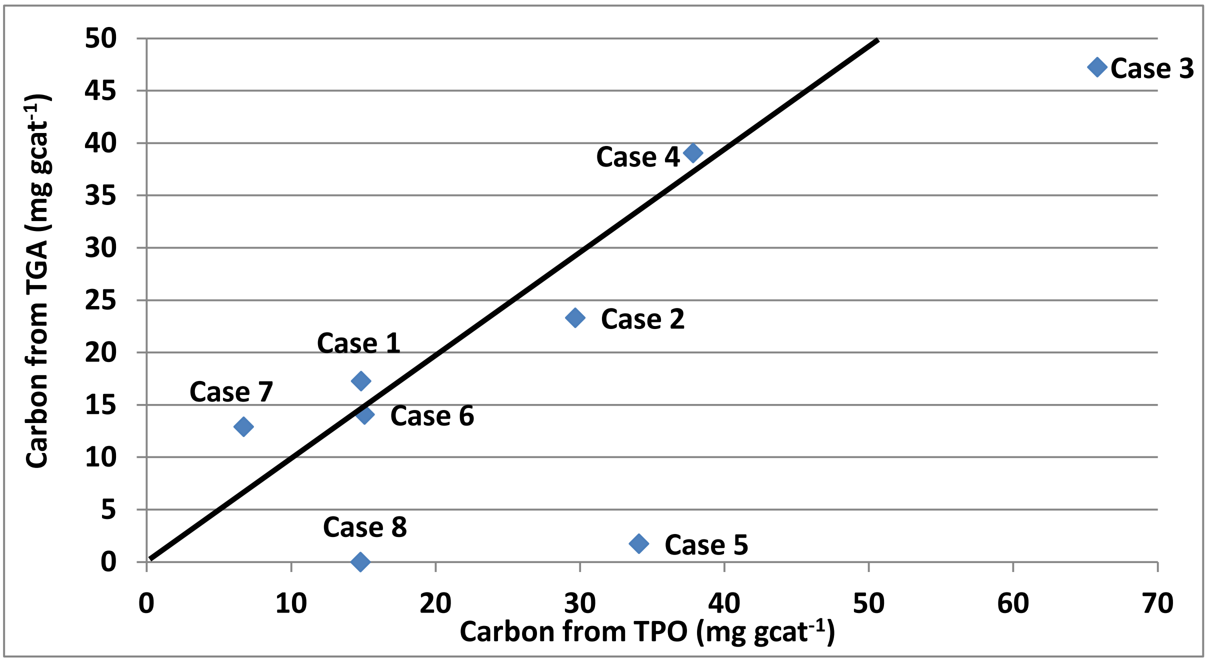

Figure 5-16 The amount of carbon formed examined by TPO and TGA

from all the cases listed in Table 5.1 (p.110).

5.4 Comparison of the Modelling and Experimental Results

In this section, the laboratory results are compared and with the results from the equilibrium modelling from different perspectives, such as the methane conversion, hydrogen yield to carbon deposition.

Figure 5-17 and Figure 5-18 are the methane conversion results and hydrogen yield, respectively, from both modelling and experimental works.

The methane conversion rate and the hydrogen yield were calculated based on the formula listed in Equation 3.64 and Equation 3.67. A noteworthy issue is that the hydrogen yield is based on the hydrogen moles per methane mole so the results could be higher than 100%. As a result, the hydrogen yield rate could be up to 400% methane steam reforming due to the combination of SMR and WGS and 200% for DR.

In general the modelling results showed a higher methane conversion rate in all cases than the laboratory results. As discussed in section 2.5, the methane molecule is absorbed on the catalyst surface, and then broken down into solid carbon and gaseous hydrogen. Meanwhile, the carbon dioxide or steam are also experienced a similar process, which offers the oxygen atoms to the carbon to form carbon dioxide or carbon monoxide. The whole process is affected by the reaction time and the adsorption constants significantly, but these two issues were not considered in the modelling process. As a result, the different results can be obtained from different methods.

Steam Reforming

From Figure 5-17, it can be seen that a higher steam concentration leads to a better methane conversion rate from the thermodynamic modelling; whilst, the experimental results showed that higher steam concentration lowers the conversion rate. This is due to the high adsorption constant of steam (k_{H_2O}), as discussed in the previous chapter (section 3.4.2) and from Equation 3.39 to Equation 3.41. As the adsorption constant of steam is in the denominator of these three equations, it can cause a significant negative effect to the reforming results kinetically. This is the reason why those cases with a higher steam concentration input have a lower reforming ability. As a result, even though the modelling results showed a high conversion rate, the experiment results were much lower.

The low methane conversion directly affects the hydrogen yield, as shown in Figure 5-18. With the high conversion rate of methane, high hydrogen yields were obtained, from 138% to 192%. By contrast, only 96% and 50% of hydrogen yields were obtained from kinetic experiments. The hydrogen yield definition in this work is based on the hydrogen molecules produced from every methane molecule. From the stoichiometric viewpoint, the yield could be as high as 400% when SMR and WGS were considered together. However, some produced hydrogen could react with side products in the system such as carbon diode through the reversed DR reaction, forming methane and carbon monoxide. In the practical experiment, by contrast, the hydrogen yield was decreasing with the increasing of steam due to the lower methane conversion rates.

Dry Reforming

The methane dry reforming, however, had a better consistency in both experiment and modelling works, when steam is not used for the reforming. The methane conversion rates were significantly improved in the experiments, even though not as high as the modelling ones. This is because the reaction time in the experiment is limited, the gases had limited time to react on the catalyst, and it is highly affected by the flow rate. As a result, the methane conversion was slightly lower in the case 5 in the experiment part, which could be caused by a high gas flow velocity. However, the reaction time in the modelling is not restricted, and the equilibrium constant of DR ($K_{P,DR}$) at 1023 K is 53.11 kPa^2 (shown in Figure 2-8). This suggests that under this condition, methane and carbon dioxide tend to reform into carbon monoxide and hydrogen. This increased the hydrogen yields in cases 3, 4 and 5. On the other hand, the produced hydrogen and other side products such as carbon monoxide could react through the reversed SMR and form methane and water. This leads to the higher hydrogen yields in the experiments than the hydrogen yields in the modelling results. However, in general, the hydrogen yield increased with increasing of carbon dioxide to methane ratio due to an increasing O/C ratio.

The Effect of Flow Rate

Cases 6 and 7 show that the flow rate has a significant effect on reforming performance. Even though the modelling work indicates the identical performance, the results from practical experiments suggest different results. By decreasing the flow rate by 50%, the methane conversion rate was improved by almost 20% and the hydrogen yield has an even higher improvement. It is obvious that a lower flow rate can improve the reforming ability due to a longer interaction time between the catalyst and the fuel gas. Clearly, the high flow rate in case 6 leads to incomplete reaction, whereas the hydrogen yield in case 7 is approximately at the theoretical value.

Combined Steam and Dry Reforming

The combined steam and dry reforming of methane in case 8, which has the highest O/C ratio (O/C = 2) in this work, was suggested by the modelling result to have the highest methane conversion rates. However, it also had the highest flow rates, and this lowered the methane conversion rates due to the short reaction time in the kinetic experiments. Despite the fact that the modelling suggested an almost complete conversion of methane at equilibrium, the case 8 had a low methane conversion and hydrogen yield.

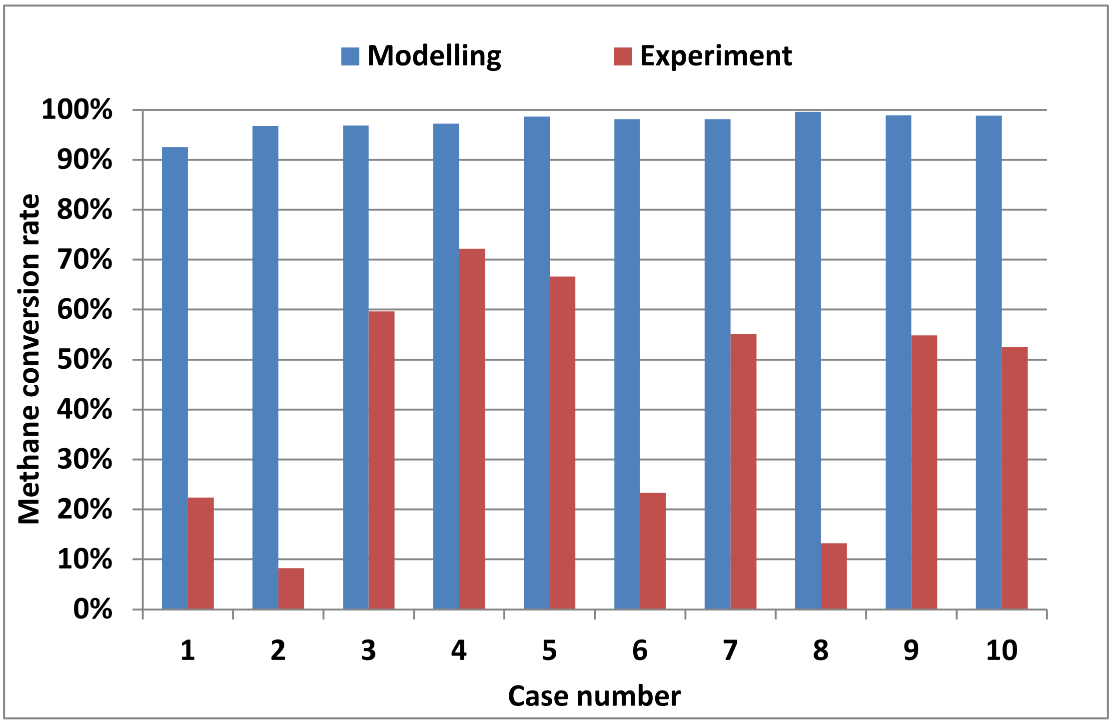

Figure 5-17 The methane conversion results different cases from modelling and experiments from of the all cases listed in Table 5.1 (p.111).

On the other hand, the short reaction time in the experiments also avoid the hydrogen consuming reactions discussed previously. This is the reason why cases 9 and 10 have a similar hydrogen yield in both modelling and experiment works, even though the methane conversion rates were different from each other. Additionally, the methane conversion rates were also improved in these two cases as the water and carbon dioxide inlet flow rates were decreased in case 9 and 10.

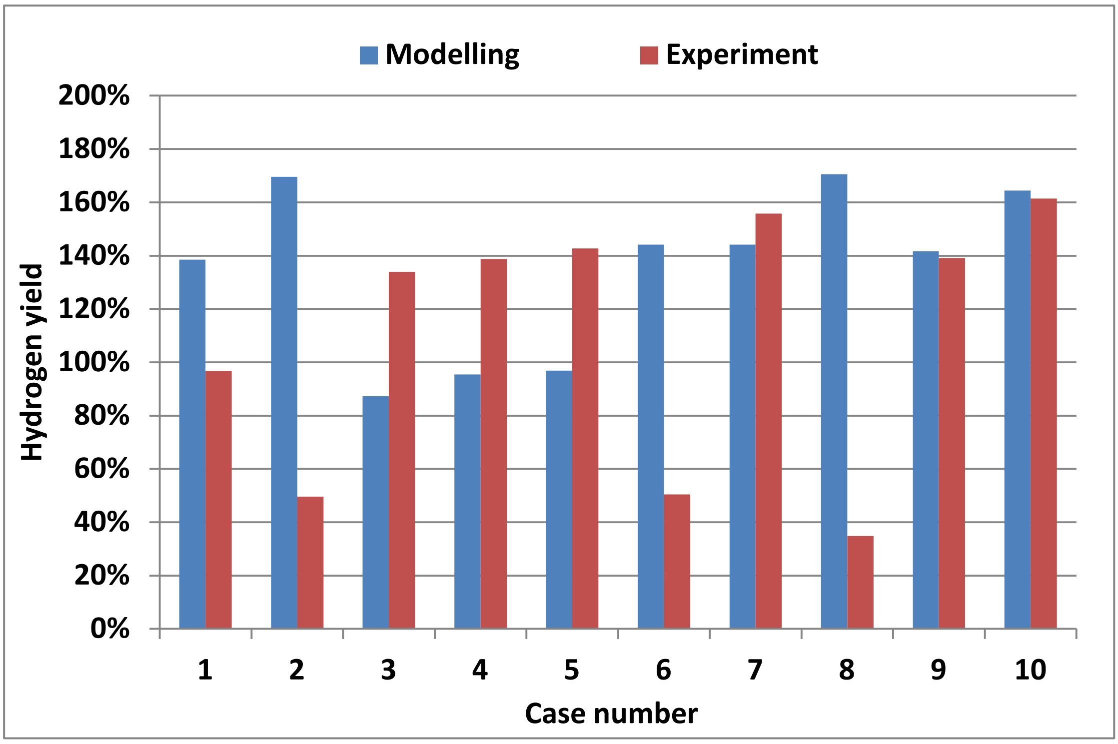

Figure 5-18 The hydrogen yield results in different cases from modelling and experiments from of the all cases listed in Table 5.1 (p.111).

From the results, it can be seen that both the total flow rate and methane partial pressure can lead to significant effects to the reforming performance when a "real" system is considered, where the reactants flow over the catalyst. This is somewhat similar to the "real" situation across an SOFC anode. Moreover, the lower reforming performance in cases 2, 6 and 8 suggest that high steam concentration can lead to a lower methane conversion, whereas the high carbon dioxide concentration does not reveal this problem. This could be either due to 1) the vaporised steam condenses to water in the kinetic reaction and/or 2) the high adsorption coefficient of steam compared to other gaseous reactants such as hydrogen and carbon dioxide as discussed in section 3.4.2 (Table 3.2). This needs an extra effort when applying the thermodynamic equilibrium modelling to the practical experiments.

5.5 Chapter Review and Conclusions

From the methane conversion and the hydrogen yield point of view, the pure methane dry reforming demonstrates a better performance than the pure steam reforming. The high adsorption coefficient of water in the pure steam reforming led to a shorter reaction time for the steam reforming reactions and lowered the methane conversion rate.

The carbon deposition results from TGA supported the modelling results that the higher O/C ratios give a better performance in preventing carbon formation than the lower ratios. The pure DR had a better ability over the pure SMR. However, the results from TPO were less conclusive due to the inhomogeneous samples used for the TPO and the small amount compared with the fuel flow rate.

The conclusion from this experiment is that the kinetic approach is better than thermodynamic equilibrium for analysis of carbon formation and methane reforming. Methane dry reforming has a higher methane conversion rate than the methane steam reforming, and the value of 2 in the O/C ratio is suggested for a better methane reforming reactions and carbon formation resistance.

Chapter 6 The Anode Recirculation Modelling

6.1 Introduction

In this chapter, kinetic models based on the theories introduced in chapter 3 were built for investigating the SOFC systems. Various models such as methane steam reforming, SOFC unit, fuel utilisation, carbon deposition and performance monitoring were firstly built and tested under different conditions. These models were then integrated, forming a larger system consisting of the SOFC, internal methane steam reforming, anode recirculation and carbon deposition was built to examine the relationships among the fuel compositions, the fuel cell operating status, the anode recycling rates and the carbon formation. The following modelling results were obtained by using MATLAB® R2010b Simulink® software and the code is in the attached CD.

6.2 Fuel Cell Model

6.2.1 Introduction

In this section, the fuel cell model was tested. In order to test the fuel cell model, both the reforming and the anode recirculation models were not considered in this work, as shown in Figure 6-1. Different fuel conditions were given for testing this model;

however, some general assumptions were made. The anode side was assumed to have 3% water vapour under all conditions, as the system was set to operate under non-sealed, non-pressurised ambient air. For the same reason, the pressure was fixed at 1 atm and the oxygen partial pressure for the cathode is 0.21. The operating temperature was set to be 1023 K. The total inlet flow rate was 357 sccm in all three cases discussed in this session. The fuel conditions and SOFC operating conditions used here would be used as the reference for an UAV application. Different ratios between hydrogen and nitrogen used in case 2 were the parametric setup to see effect of fuel dilution. In case 3, the fuel composition was the simulated reformed syngas.

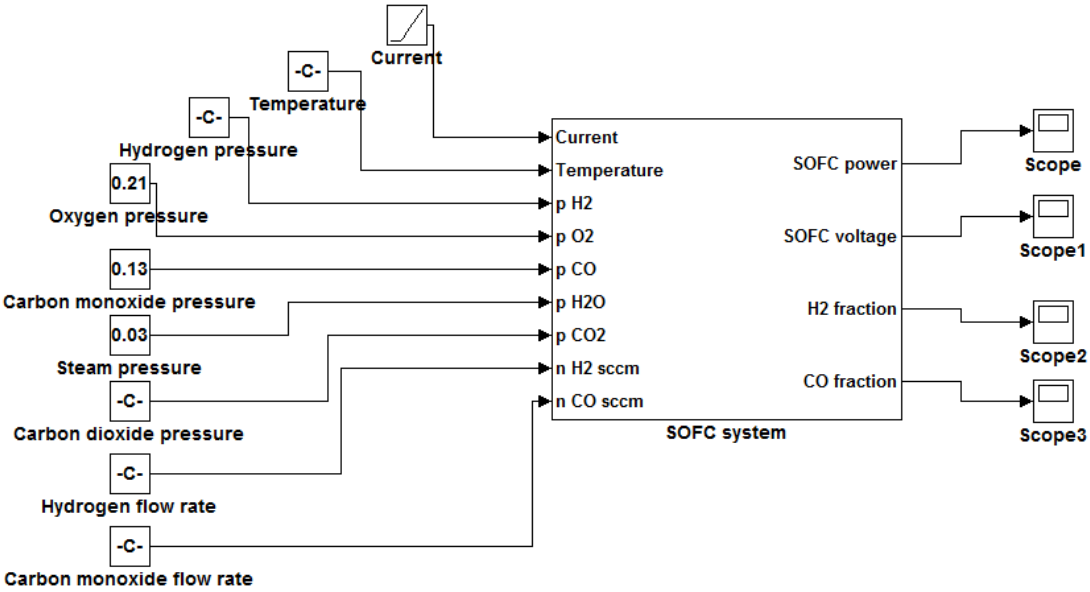

Figure 6-1 The modelling diagram of the fuel cell model as implemented in Matlab.

6.2.2 Case 1: Pure Hydrogen and Diluted Hydrogen

In this section, two different fuel conditions were given as input to the fuel cell model to examine how the fuel composition affects the cell performance. One case used 100 sccm pure hydrogen as the fuel, whilst in the other case, the same hydrogen flow rate was diluted by the addition of 257 sccm nitrogen gas flow.

The results are shown in Figure 6-2. An OCV of 1.11 V was obtained in the pure hydrogen case, which is better than the 1.05 Vin the diluted hydrogen case. The better performance was continuing throughout all different output current densities. At the high output current density (i.e. 1800 mA cm^{-2}), the pure hydrogen case has 0.87 V which is still better than the 0.83 V from the mixed gas case. This is because the former case had a higher hydrogen partial pressure than the latter case, and thus a higher Nernst voltage is produced.

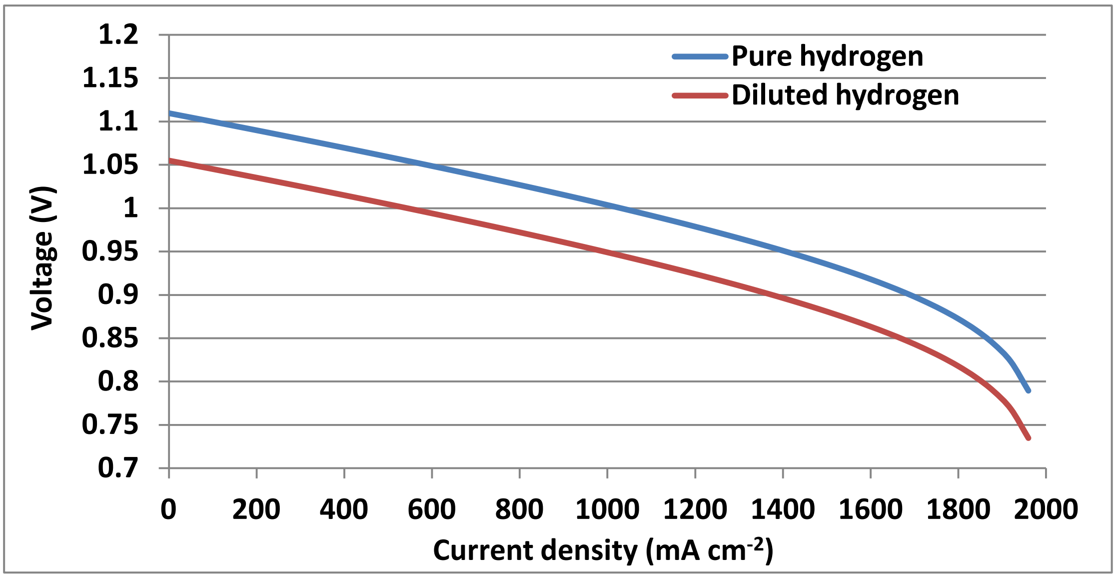

Figure 6-2 The IV curve SOFC fed with pure hydrogen and diluted hydrogen.

6.2.3 Case 2: Different Hydrogen Partial Pressure

In this section, the hydrogen was mixed with nitrogen in different ratios including H_2:N_2 = 30%:70%, 40%:60%, 50%:50% and 60%:40% in flow rate. The results are shown in Figure 6-3. With an OCV of 1.09 V, the 60% hydrogen case has a higher voltage among all scenarios due to the highest hydrogen partial pressure, as expected from the Nernst equation. The performance decreases with decreasing hydrogen concentration, as there is a relative increase of the nitrogen dilution gas. An OCV of 1.05 V was produced by the lower hydrogen concentration case (30%). All the ratios produce a similar output voltage at high output current densities (above 1800 mA cm^{-2}) because it is the concentration losses that dominate the cell performance. The effect of the Nernst equation is undermined within this region, thus the difference of the output voltage among different cases are smaller than they are at the OCV and low output current densities.

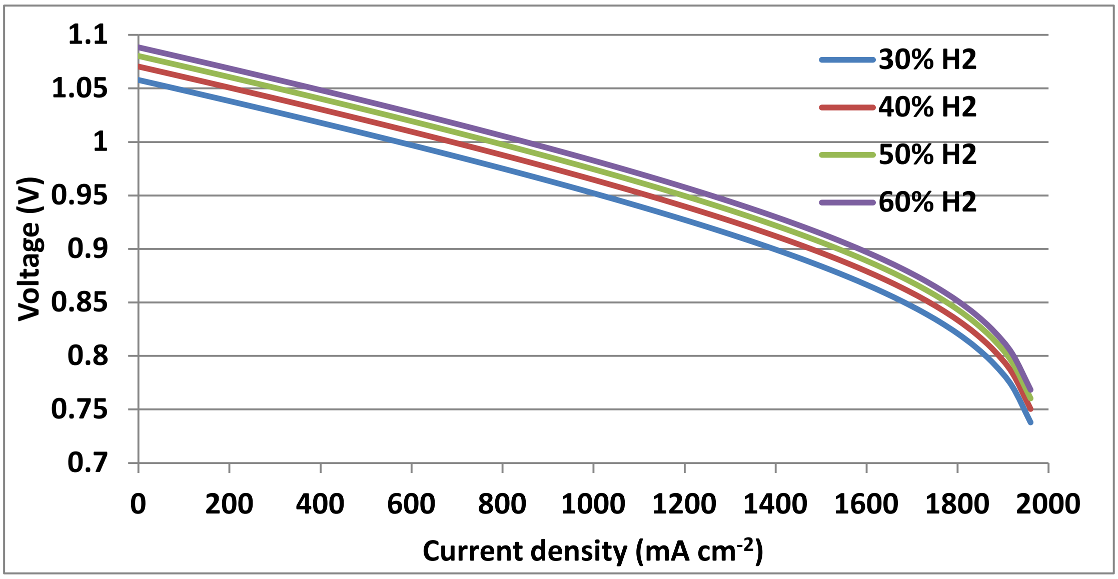

Figure 6-3 the IV curve of different ratios between hydrogen and nitrogen.

6.2.4 Case 3: Mixed Gases

In this case, more gases are introduced to the fuel cell model as the fuel compositions. The inlet fuel flow contains 13% carbon monoxide, 14.2% hydrogen, 6.2 carbon dioxide, 0.8% methane, and 65.8% nitrogen. However, the methane reforming reactions were not included in this model and therefore the voltage was generated from the oxidation of the given hydrogen and carbon monoxide. A noteworthy issue is that even though with only 27.2% of the fuel partial pressure (13% carbon monoxide and 14.2% hydrogen), the OCV, 1.12 V, is still higher than the OCV in the 30%

hydrogen scenario, around 1.05 V, in session 6.2.3. This is due to the higher Gibbs free energy of the carbon monoxide oxidation reaction, as shown in Figure 3-1. The higher Gibbs free energy leads to higher Nernst voltage and thus a better performance is observed. This is shown in Figure 6-4.

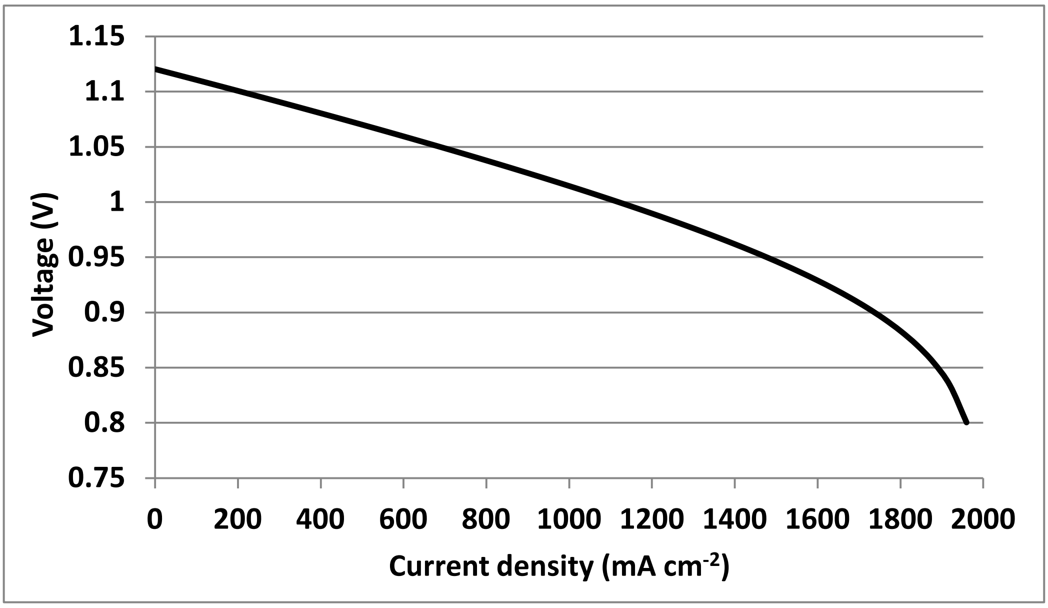

Figure 6-4 The IV curve of the mixture fuel.

6.3 Fuel Cell and Anode Recirculation

This section examines the anode recirculation effect on SOFC systems. Hydrogen was assumed to be the only fuel for the SOFC model, methane reforming reactions and heat management were not considered. Systems operating under different current densities with different recycling rates were investigated in order to determine their impact on the system.

6.3.1 Model Integration

The fuel cell, together with the utilisation and recycling models, were integrated to test the performance of the anode recirculation. Hydrogen was the only fuel and no reforming reactions were considered.

The oxygen was remained at 0.21 bar and the water pressure was set as 0.11 bar. The system was assumed to operate at 1023 K, with 20 sccm of hydrogen flow. The hydrogen pressure is set to 0.89 bar, due to some water vapour in the atmosphere mentioned previously. A ramp signal was given to the fuel cell model to represent the different current densities. This meant that the model could work out the voltage according to the given current density, resulting in an I-V curve, as shown in Figure 6-6. Meanwhile, the fuel utilisation model works out the fuel utilisation from the given current density and fuel flow rate in units of moles per second. The fuel utilisation was then used by the recycling model for calculating the produced water and residual hydrogen. The recycled hydrogen and water were added to the inlet fuels before being fed into the SOFC model. In this work, different recycling rates including 0%, 30%, 50%, 80%, and 100% was investigated. The modelling layout is shown in Figure 6-5.

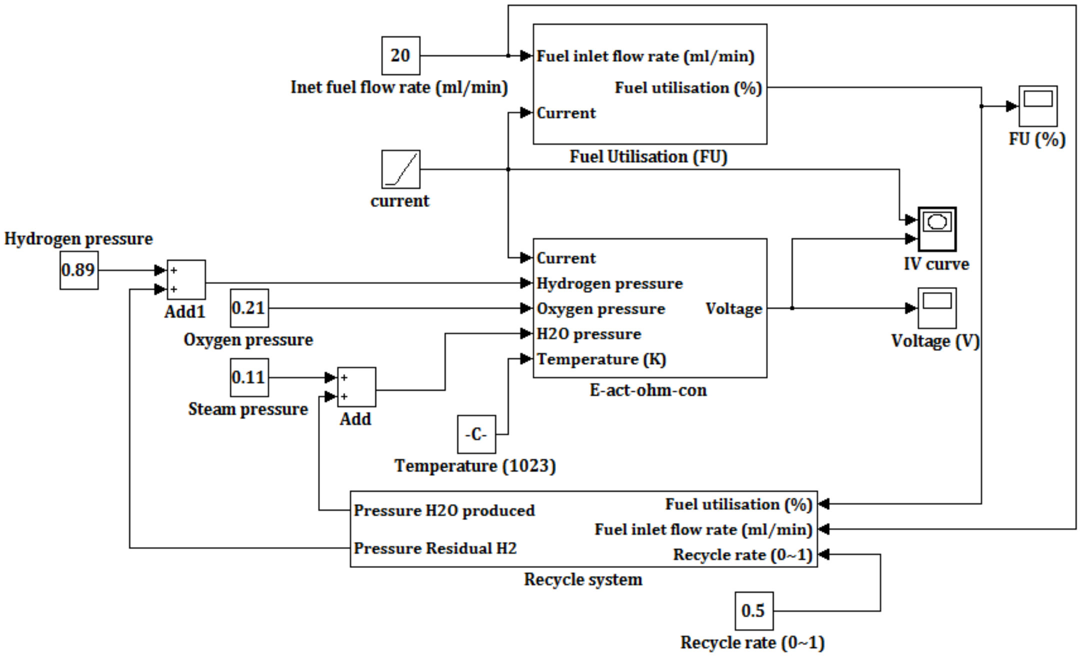

Figure 6-5 Modelling diagram of fuel cell with anode recirculation system as implemented in Matlab.

6.3.2 Cell Performance

Figure 6-6 shows the I-V curve with different AOGR rates. At low current densities operation (below 300 mA cm^{-2}), high recycling rates have a better cell performance. This is because of the low fuel utilisation at low current densities. Thus the main composition of anode off-gas is still hydrogen. High recycling rates bring more hydrogen back to the system and increase its partial pressure. Therefore the cell performance is improved from the recirculation. On the other hand, with the increase of current density (above 300 mA cm^{-2}), more hydrogen is consumed and turned into water. The increasing recycled steam decreases the hydrogen concentration in the cell, and as a result, lowers the cell voltage. However, only hydrogen was considered as fuel and the reforming reactions are not included in this model. Additionally, the heat management within the system is not considered as well.

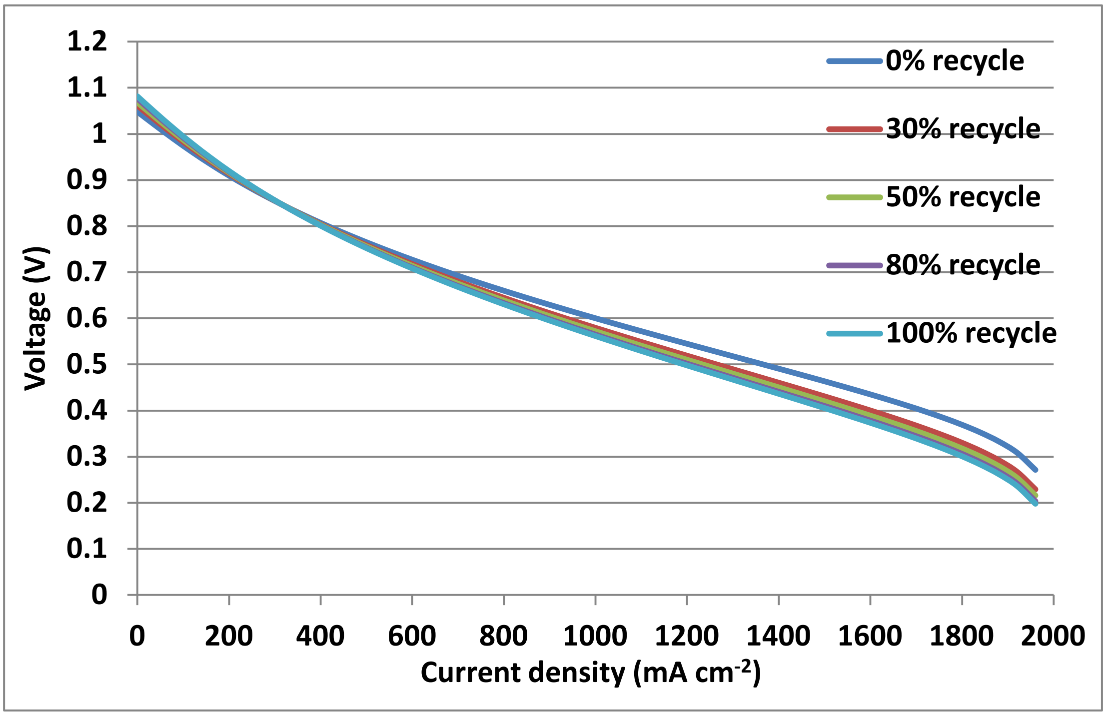

Figure 6-6 Current density against voltage with different recycling rates

6.3.3 Discussion

From the results in this section, it can be clearly seen that the fuel composition can significantly affect the cell performance. As a result, the recycling rate has to be carefully determined according to the cell operating conditions. At low current density (below 300 mA cm^{-2}), higher recycling rates (i.e. 80% and 100%) bring more unused hydrogen to the inlet fuel stream, and increase cell performance. On the other hand, high current densities imply high fuel utilisation, and therefore more water is produced, diluting the fuel. This model only considers hydrogen as a fuel. For a methane fed SOFC system, anode recirculation could have a different influence for several reasons. First, SOFCs can react with carbon monoxide, and methane, to generate electricity. These fuels have higher Gibbs free energies in their oxidation reactions, as mentioned previously in section 3.1. Secondly, water or carbon dioxide is essential for methane reforming. Higher concentrations of water or carbon dioxide can convert methane and carbon monoxide into hydrogen more completely, as discussed in the previous chapter. Thirdly, the high conversion of methane and carbon monoxide lowers the possibility of carbon deposition on the anode side. A further discussion will be presented in the following sections.

6.4 SOFC with Internal Reforming and Anode Recirculation

In this section, a dynamic modelling approach is employed to investigate how different steam to methane ratios and the AOGR rates affect the methane internal reforming, cell performance, and carbon formation.

6.4.1 Model Integration

The dynamic model consists of a methane steam reforming model, SOFC model, recycling model, a carbon formation model and system monitoring model.

The initial temperature and inlet fuel flow rate was set at 1073 K and a total of 60 ml min^{-1} (sccm) with the different steam to methane ratios ranging from 1:4, 1:2, 1:1, 2:1 and 4:1. The inlet fuel flow was mixed with the recycled fuel flow. The total flow rate is then the sum of initial fuel stream and the recycled anode off-gas. By providing the system pressure (here, it is 1 bar), the partial pressure of each gas in kpa can be worked out based on their flow rate after mixing. The output was then fed into the steam methane reforming model, in which the SMR, WGS and DIR occur. Since the consumption/formation rate of each gas was the only output provided by the reforming model, the output of the reforming model was then added to the flow from the first mixing, and fed into the second mixing model. A new partial pressure and flow rate was then obtained after the second mixing model, which was then fed into the SOFC model.

The output voltage was calculated from the SOFC model with the given current density, partial pressure of each gas and other operating conditions. The fuel utilisation was then also obtained based on the fuel flow rate after the second mixing model. Three different current densities including 0.5, 1.0 and 1.4 A cm^{-2} were selected here to represent the low, medium and high current density operating conditions. The utilisation rates were calculated based on the given operating current density, and the flow rate of fuel fed into the SOFC model. The formation/consumption velocity of each gas was then calculated and summed to obtain the composition of the anode off gas. After multiplying this by the recycling rate, the recycled exhaust was then added, with the system inlet fuel flows, to the first mixing model. Once the recycled exhaust gases were mixed with the inlet flow, the carbon deposition model can provide the carbon activities discussed in session 3.5 to determine the possibility of carbon formation. The methane conversion rate and cell performance were also calculated by the system monitoring model, as shown in Figure 6-7.

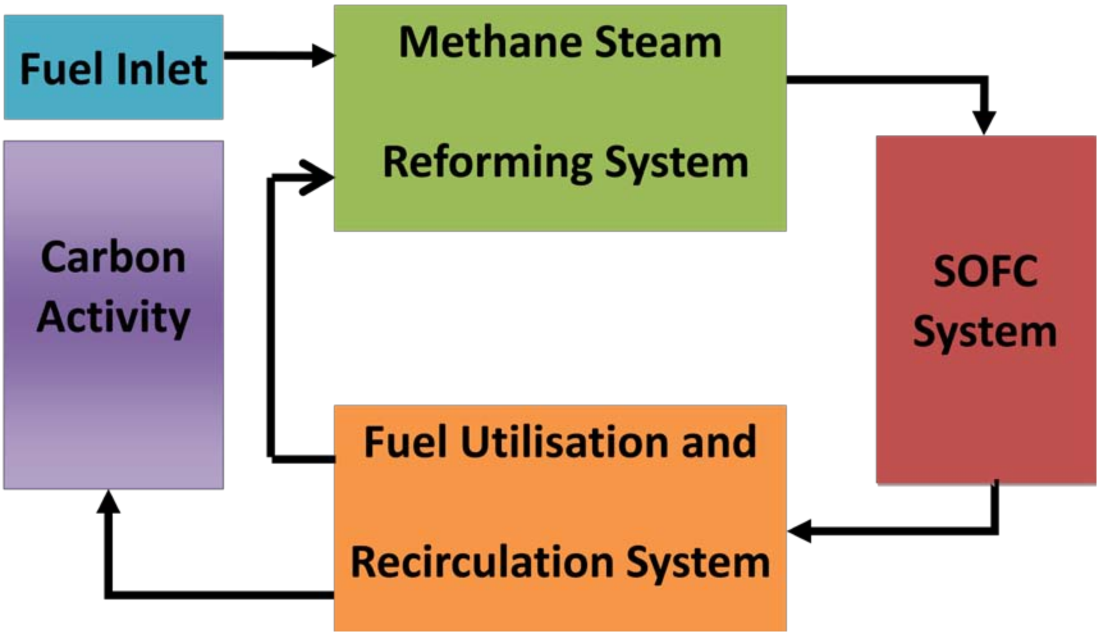

Figure 6-7 The kinetic modelling diagram.

6.4.2 Methane Conversion

Good methane conversion rates are observed when the cell is operating under low current densities and low recycling rates. The conversion rate then decreases with the increase of the recycling rate, as shown in Figure 6-8 (a). Because the low current also implies low fuel utilisation, more unused fuel was recycled with the increase of recycling rate. Based on Le Chatelier's principle, higher concentration of products shifts the reaction backwards. In this case, the unused hydrogen and carbon monoxide is recycled into the reforming chamber and causes a high concentration of product which reverses the reaction direction, and thus decreases the conversion rate.

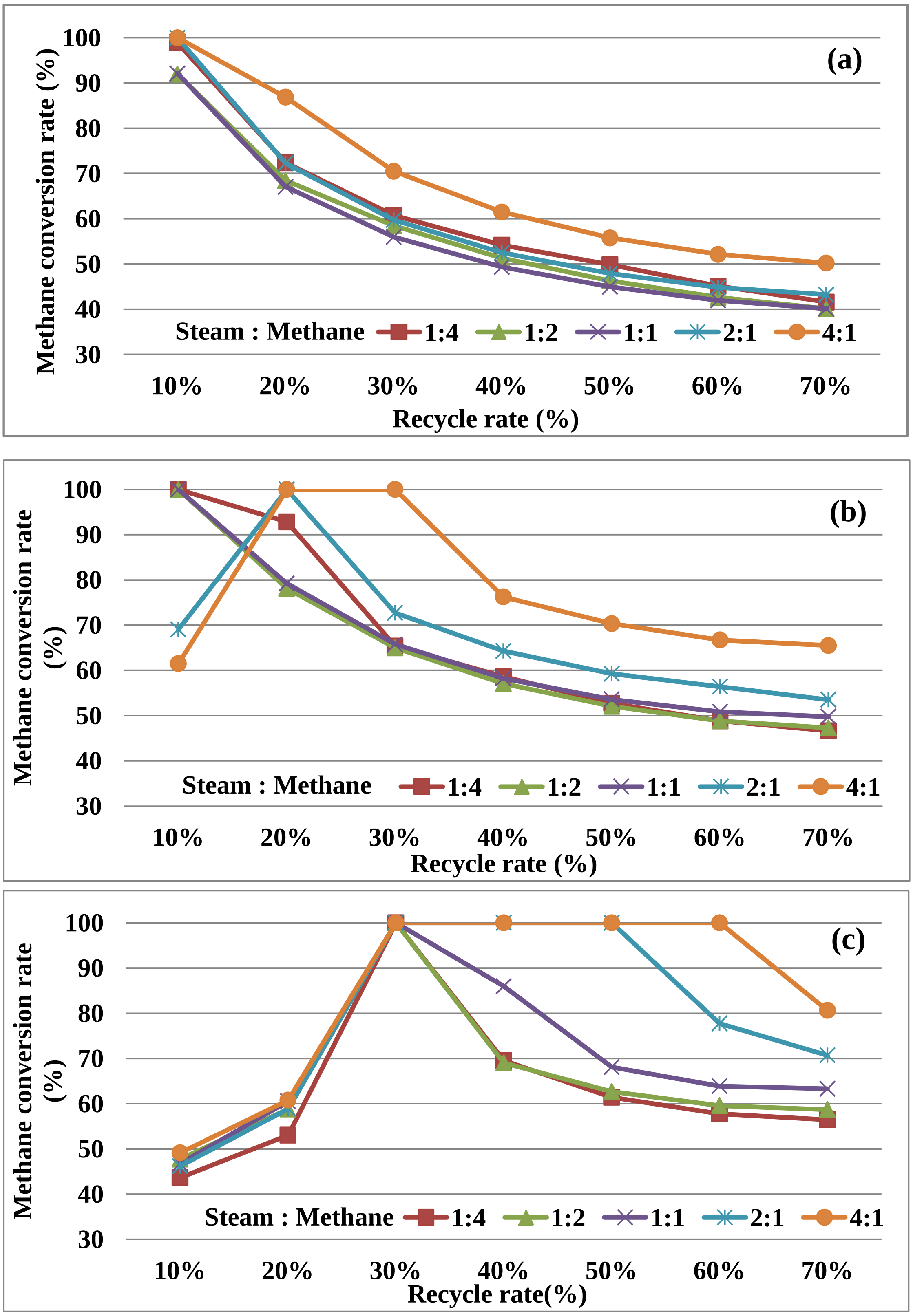

Figure 6-8 Methane conversion rates under a(a) low current density at 0.5 A cm^{-2}, (b) medium current density at 1.0 A cm^{-2} and (c) high current density at 1.4 A cm^{-2} with different steam/methane ratios and recycle rates.

When the cell is operating at medium current density, two different situations appear. Good conversion rates are obtained in low S/C ratios (i.e. 1:4, 1:2 and 1:1). However, excess water in high ratios decrease the reforming performance. This is because water has a relatively high adsorption coefficient (1.77×10^{5}) compared with carbon monoxide (8.23×10^{-5}), methane (6.65×10^{-4}) and hydrogen (6.12×10^{-9}) [78, 136, 140]. This was discussed in Table 3.2 (section 3.4.2).

This can be seen from Equation 3.42. According to Equation 3.39 to Equation 3.41, a small amount of water can cause a significant effect. This phenomenon reduces with an increase of recycling rate, because more unused methane is recycled and the excess water is consumed, thereby improving the conversion rates, as shown in Figure 6-8 (b). Under high recycling rates, all S/C conditions give lower conversion performance due to the used reactants, as in the low current densities.

Under high current density, shown in Figure 6-8 (c), high fuel utilisation produces high concentration of water. The reforming performance is significantly affected even with low recycling rates. This situation decreases with an increase of recycling rates as more methane is recycled, thus diluting the water concentration until higher recycling rates.

6.4.3 Cell Performance

The cell performance under different operating conditions is presented in Figure 6-9. Figure 6-9 (a) shows the voltage when the output current density is 0.5 A cm^{-2}. From the viewpoint of steam to methane ratio, higher ratios bring more water which decreases the partial pressure of fuel and thus results in a lower voltage. With an increase in recycling rate, more exhaust gases are recycled, diluting the fuel and therefore decreasing the voltage.

For the cell performance, being affected by the reforming results, two different situations appear under medium current density. For higher steam to methane ratios (i.e. steam : methane = 2:1 and 4:1), smaller fuel partial pressures due to the low conversion rates together with higher water concentration cause lower cell voltage, as shown in Figure 6-9 (b). The phenomenon reduces when the recycling rate increases because more unused methane is recycled, and thus more hydrogen and carbon monoxide are produced from methane reforming. However, under high recycling rates, all operating conditions generate low cell voltage due to the diluted fuel.

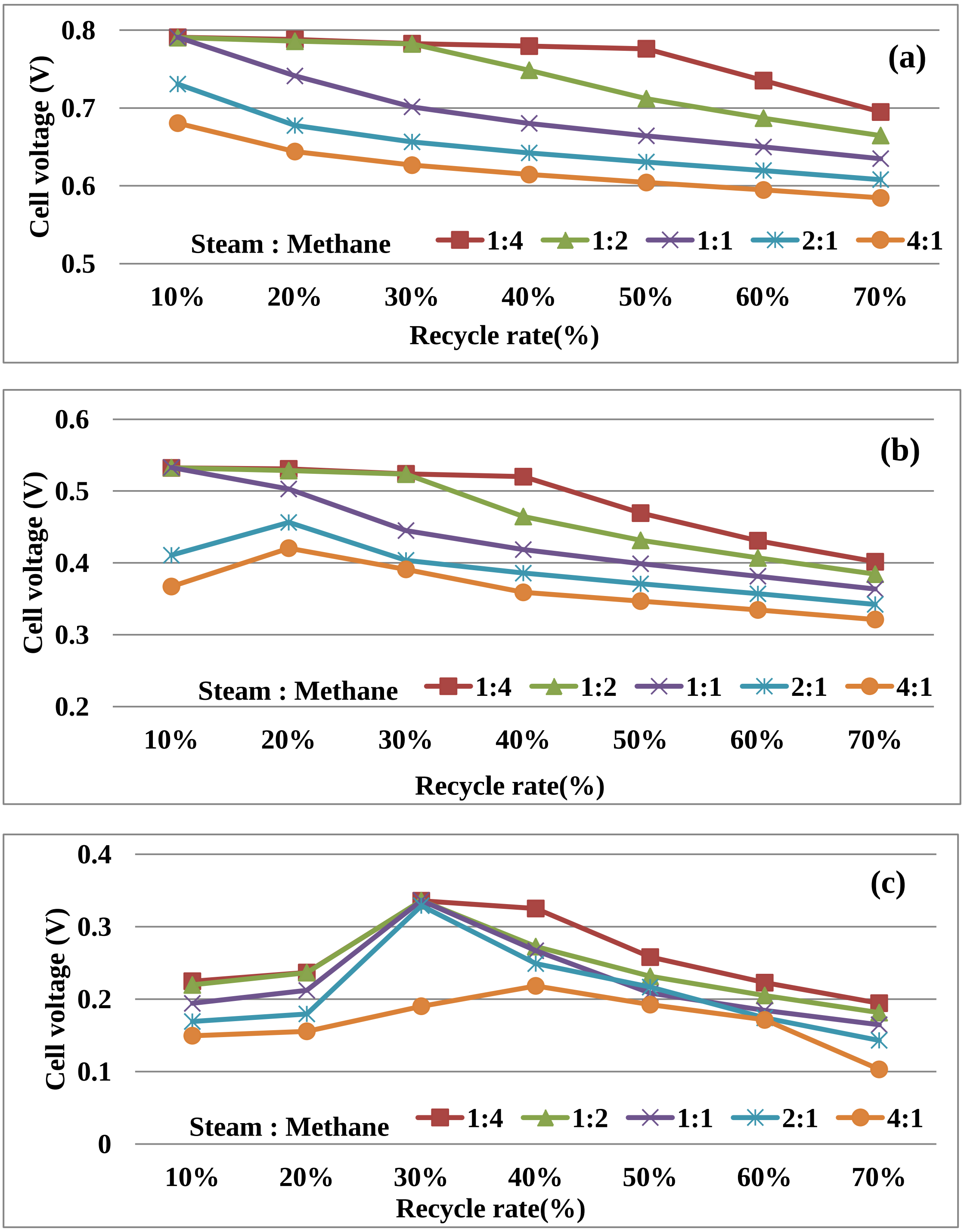

Figure 6-9 Cell voltages under a (a) low current density at 0.5 A cm^{-2}, (b) medium current density at 1.0 A cm^{-2} and (c) high current density at 1.4 A cm^{-2} with different steam/methane ratios and recycle rates.

For the medium current density loading, the cell performance has dropped due to the low methane conversion rates and the higher output current than the previous scenario. Besides, high fuel utilisations come from high current densities, which also dilute the fuel concentration and thus a decrease in voltage is observed whilst the recycling rate is increasing above 50%. This is shown in Figure 6-9 (c).

6.4.4 Carbon Deposition

Figure 6-10 shows the carbon coefficients under different operating conditions. The negative value of log(γ) (the shadowed area), corresponding to $\gamma < 1$, implies the possibility of carbon formation in the system.

At low current density operation, solid carbon is formed when the lower steam to methane ratios coincide with lower recycling rates. For the steam : methane = 1:4 and 1:2 scenarios, high recycling rates such as 70% and 60% are required for the system to inhibit carbon formation. A 40% - 50% recycling rate is required for the steam : methane = 1:1 scenario, and lower rates required for the higher ratios, as shown in Figure 6-10 (a).

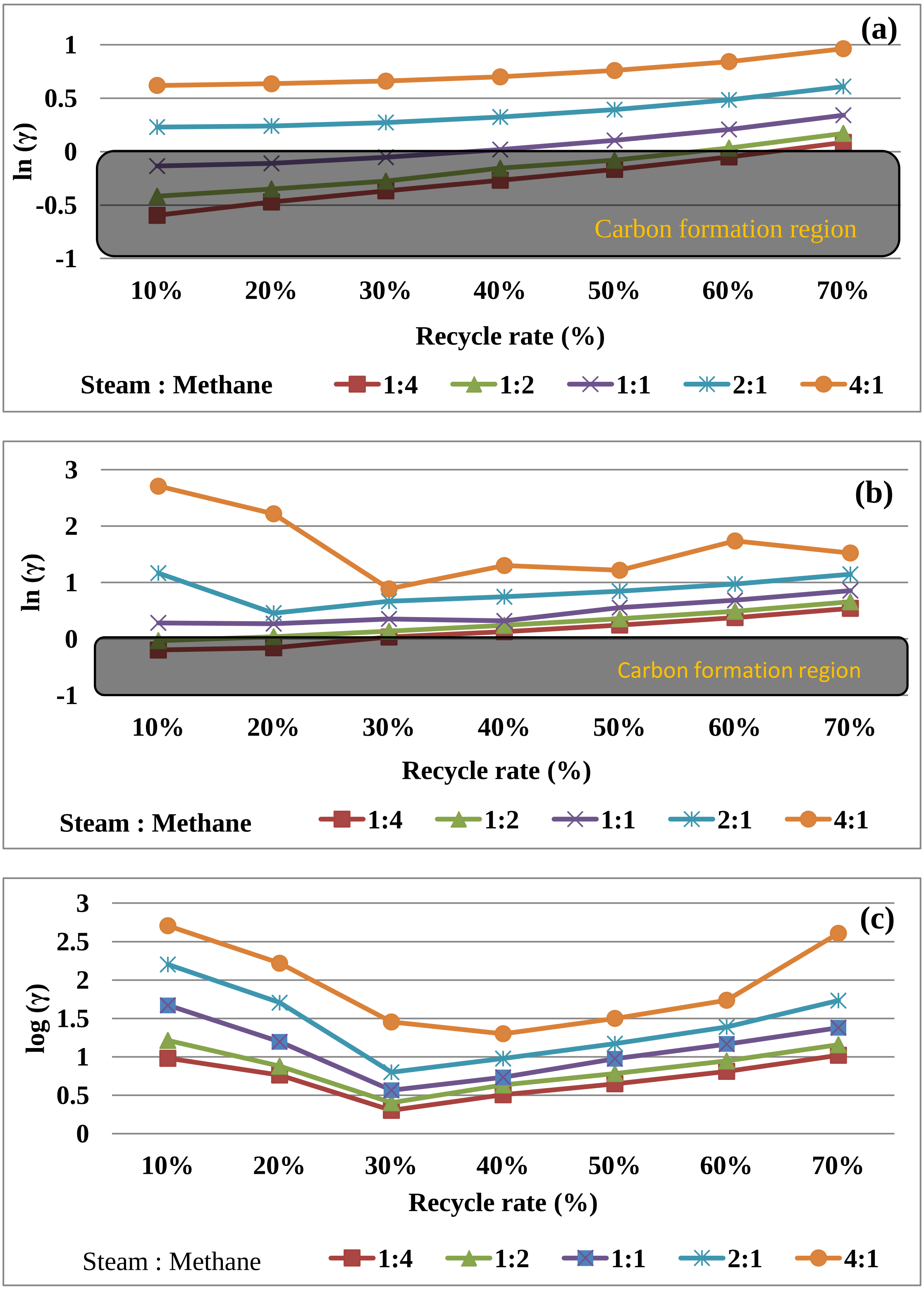

Figure 6-10 Carbon coefficients under a (a) low current density at 0.5 A cm^{-2}, (b) medium current density at 1.0 A cm^{-2} and (c) high current density at 1.4 A cm^{-2} with different steam/methane ratios and recycle rates.

This is because, under low fuel utilisation, a significant amount of unused methane is also recycled with a relatively low concentration of water. High recycling rates bring unused hydrogen back to the system to shift the methane cracking reaction (Equation 2.31) backwards. For higher ratios, sufficient water at the inlet end provides better methane conversion and prevents carbon deposition completely.

Unlike at low current density, smaller amounts of hydrogen and more water are recycled when the system is operating at medium current densities. As a result, lower recycling rates are sufficient for preventing carbon deposition. A noteworthy issue is that in 20-30% recycling for the steam : methane = 4:1 and 2:1 ratios, the carbon activities decrease and then increase with the increase of recycling rates in Figure 6-10 (a). Under 1.0 A cm^{-2}, more hydrogen is consumed and formed into water. This is then recycled back to the system and increases the conversion rate of methane, as shown in Figure 6-8 (b). With the excess water being consumed in the methane conversion, the carbon coefficients imply the system is moving towards carbon formation. However, as more water is recycled due to the high recycling rates, the system does not again favour carbon formation. Under high current density operation, all ratios have a good performance with regard to preventing carbon formation even with a low recycling rate. This is shown in Figure 6-10 (c). However, similarly to the high ratios in medium current density, decreased carbon activities are observed when the rate increases from 10% to 30%. For high fuel utilisation, higher water vapour concentration lowers the methane conversion rate. The unconverted methane is then recycled back to consume the excess water. When the recycling rate reaches 30%, the amount of recycled methane is sufficient for consuming the water produced, and so the methane conversion rates go up which decreases the possibility of carbon formation inside the system.

6.4.5 Discussion

It can be seen from previous figures that the steam to methane ratio, together with the cell operating conditions can affect the formation of solid carbon dramatically. Lower steam to methane ratios (e.g. 1:4 and 1:2) need more additional water to prevent carbon formation. Therefore, low current density (j = 0.5 A cm^{-2}), high recycling rates (70% and 60%) are required. This demand decreases as the current density increases. At medium current density (j = 1.0 A cm^{-2}), the demand of additional water for the low steam to methane ratios decreases to 60% and 50%, respectively. At high current (j = 1.4 A cm^{-2}), even a 10% of recycling rate is sufficient for the system to prevent carbon formation. Higher steam to methane ratios (e.g. steam : methane = 1:1, 1:2, and 1:4) are free from carbon formation in all three current densities, regardless of the recycling rates as the water supplied in the inlet stream is able to convert methane more completely. The lower methane concentration leads to a lower possibility of carbon formation. A good combination of initial steam to methane ratio and recycling rate with cell operation status can effectively avoid the formation of solid carbon, and have minimal detrimental effect on the cell performance.

6.5 Chapter Review and Conclusions

This chapter presented the modelling results in different areas, from single cell with various fuel compositions, different recycling rates, to a dynamic modelling for the system consisting of methane reforming, SOFC, recirculation and carbon deposition modules.

In the first section, the results show that higher hydrogen concentration leads to a higher Nernst voltage and a better cell performance is obtained. For the AOGR system with hydrogen is used as fuel, higher recycling rates (above 50%) is suggested when the fuel utilisation rate is less than 15%. On the other hand, a lower recycling rate is recommended when the fuel utilisation is above 15%.

The results of the kinetic modelling showed that from the perspective of methane reforming, higher water concentration reduced the methane conversion rate as it lowered the methane partial pressure. On the other hand, an increase of the ratio between steam and methane or increase in recycling rate and current density could improve the ability to prevent carbon formation.

Chapter 7 Conclusions and Further Work

7.1 Conclusions

With the base of thermodynamics, followed by the kinetic and equilibrium modelling and together with the practical experiments, this thesis presented a prospect for a long operation methane fed SOFC with anode off-gas recirculation (AOGR) system by investigating the interactions among the methane reforming, cell performance, anode off-gas recycling rate and carbon formation in the SOFC anodes.

7.1.1 Carbon Formation Determination

A detailed introduction and comparison of the C-S EQ and the CA approach were presented and discussed. The C-S EQ approach can only deal with systems consisting methane and steam only, whilst the RSF needs to be considered when the CA approach is employed to determine carbon formation. The CA approach with RSF reaction, $\gamma_{MC\text{-}BD\text{-}RSF}$, can produce similar results as the C-S EQ approach. A peak demand of 1.48 in the steam to methane ratio was found at 850 K from both approaches. The ratio decreases when the temperature increase. A ratio of 1.2 in the steam to carbon ratio is required at 1000 K to prevent carbon formation, and this value is only 1.0 at temperature above 1100 K. Additionally, the CA approach is not restricted by the fuel composition, it can be applied to systems containing carbon oxides such as the AOGR system, in which the C-S EQ approach fails. The modified approach is expected to provide reasonable results as the C-S EQ approach.

7.1.2 Methane Reforming

Combined methane steam and dry reforming was investigated, from both thermodynamic equilibrium modelling and kinetic experiment approaches. The modelling results indicated the thermodynamic equilibrium is not affected by the total flow rate but by the oxygen to carbon atomic ratio in the fuel stream, and higher O/C ratios lead to better methane conversion and could effectively prevent carbon formation. The steam reforming can have a better methane conversion and its hydrogen yield is doubled than the hydrogen yield in dry reforming. Additionally, the combined steam and dry reforming of methane can achieve more than 99% of methane conversion.

However, in the practical experiments, more issues other than the O/C ratio and temperature can affect the reforming performance. Steam reforming preformed worse than dry reforming. The methane conversion rate was only up to 20%, comparing to the 60% - 80% in dry reforming. The high fuel flow rate lowered the methane conversion rate. Despite the fact that the combined reforming has a higher O/C ratio, the high flow rate lowers the reforming ability.

From the prospect of preventing carbon formation, higher O/C ratio is suggested as it can improve the methane conversion and thus reduce the sources of solid carbon. However, as mentioned before, higher steam and/or carbon dioxide input increases the flow velocity, reducing the reaction time and lowers the cell performance kinetically. A trade-off between the SOFC performance and preventing carbon formation needs to be considered.

7.1.3 Solid Oxide Fuel Cells

A trade-off between the SOFC operating conditions and anode off-gas recycling rate is required to for a higher system efficiency and longer operating life.

The cell operating performance is affected by the fuel partial pressure significantly. When only hydrogen is used as fuel, higher recycling rates (above 50%) is preferred when the fuel utilisation is low, as most hydrogen is not consumed. On the other hand, lower recycling rates are recommended when the fuel utilisation is high as most hydrogen is turned into water and lowers the fuel pressure when being recycled.

By contrast, when methane is used as fuel, the anode-off gas recirculation is expected to improve the reforming performance and reduce carbon formation. The steam to methane = 1:4 ratio case can generate a 0.2 V higher cell voltage than the 4:1 case, whilst there could be only 0.1 V difference in the same fuel condition with different recycling rates.

7.2 Further work

Some efforts are still required attaining the origin aim of this project. They can be divided into the modelling work and the practical work as following:

Modelling work:

1. This anode recirculation modelling in this work only considered the steam reforming of methane. The dry reforming of methane is suggested to be considered in the future work as DR can occur in the AOGR system.
2. This work did not consider the heat transmission and losses. For example, the temperature of recycled gas can drop quickly in the recycling loop. As a results, these gases hardly carrying a similar temperature to the SOFC operating

temperature when they reached the inlet steam, thus the additional heat source may be required.

3. Higher dimensional (i.e. 1, 2 or 3-D) kinetic modelling works including the heat management can be a helpful tool for a more detailed investigation towards carbon deposition within the cell dynamically, as the reactions may be endothermic or exothermic and occur in different parts of the cell causing the different temperature distribution within the cell, and a significant effect to the operating conditions.
4. The rate determination of the reactions within SOFCs. It is shown in this work that methane breaks down into solid carbon and gaseous hydrogen firstly in the reforming process. The carbon is then removed from the catalyst by the water or carbon dioxide. It is important to understand the reaction rate and descript in mathematical forms, so that the amount of carbon formed can be determined. After that, the oxidation rates of hydrogen and carbon monoxide are also required to be determined so that the model can predict the production rate and thus will be able to estimate the amount of carbon removal by using the produced water or carbon dioxide.

Practical work:

1. As mentioned previously, the reaction rates need to be demined for building mathematical equations. This may require to use the isotopic elements to for detailed examination.
2. A bigger scale of internal SOFC internal reforming is expected to allow the reforming status to be closer to thermodynamic equilibrium, improving the methane conversion and lowering the possibility of carbon formation.
3. The composition of the anode exhaust needs to be examined first and compared with the modelling results under different output current densities. The simulated gases according to the results are produced and mixed with the inlet gases before being fed into the cell. The optimised recycling can be worked out from the O/C ratio in order to prevent carbon formation. The cell is then tested for a longer period to observe its performance and the formation of carbon on the anode side after testing.

References

1. Ni, M., *Modeling of SOFC running on partially pre-reformed gas mixture.* International Journal of Hydrogen Energy, 2012. **37**(2): p. 1731-1745.

2. Brouwer, J., *On the role of fuel cells and hydrogen in a more sustainable and renewable energy future.* Current Applied Physics, 2010. **10**(2, Supplement): p. S9-S17.

3. Zink, F., Y. Lu, and L. Schaefer, *A solid oxide fuel cell system for buildings.* Energy Conversion and Management, 2007. **48**(3): p. 809-818.

4. Shekhawat, D., et al., *Effects of fuel cell anode recycle on catalytic fuel reforming.* Journal of Power Sources, 2007. **168**(2): p. 477-483.

5. Jia, J., et al., *Effects of gas recycle on performance of solid oxide fuel cell power systems.* Energy, 2011. **36**(2): p. 1068-1075.

6. Kazempoor, P., V. Dorer, and A. Weber, *Modelling and evaluation of building integrated SOFC systems.* International Journal of Hydrogen Energy, 2011. **36**(20): p. 13241-13249.

7. Taher, S.A. and S. Mansouri, *Optimal PI controller design for active power in grid-connected SOFC DG system.* International Journal of Electrical Power & Energy Systems, 2014. **60**(0): p. 268-274.

8. Bompard, E., et al., *Technical considerations of SOFCs for mixed DG/backup power applications.* International Journal of Hydrogen Energy, 2008. **33**(22): p. 6743-6748.

9. Vakouftsi, E., et al., *A detailed model for transport processes in a methane fed planar SOFC.* Chemical Engineering Research and Design, 2011. **89**(2): p. 224-229.

10. Singhal, S.C. and K. Kendall, *High Temperature Solid Oxide Fuel Cells*. 2003, Oxford: Elsevier Ltd.

11. Stolten, D., ed. *Hydrogen and Fuel Cells - Fundamentals, technologies and Applications*. 2010, WILEY-VCH Verlad GmbH and Co.: Weinheim.

12. *Protonex award to further develop military SOFC systems.* Fuel Cells Bulletin,

2009. **2009**(5): p. 6.

13. Cimenti, M. and J. Hill, *Direct Utilization of Liquid Fuels in SOFC for Portable Applications: Challenges for the Selection of Alternative Anodes.* Energies, 2009. **2**(2): p. 377-410.

14. Hartmann, L., et al. *POX-reformer for gas oil / Diesel in stationary and automotive SOFC-technologies* 2012 [cited 2014; Available from: http://wordpress.owi-aachen.de/wp-uploads/2012/07/Luzern_020704.pdf.

15. Reinkingh, J., et al., *Fuel cell power for transportation 2002*. 2002: Society of Automotive Engineers.

16. Mukerjee S, G.M., Haltiner K, Faville M, Noetzel J, Keegan K, et al, *Solid oxide fuel cell auxiliary power unit – a new paradigm in electric supply for transportation.*, in *Proceedings of the SOFC VII Electrochemical Society*. 2001. p. 173.

17. Behling, N.H., *Fuel Cells: Current Technology Challenges and Future Research Needs*. 2012: Elsevier Science.

18. Automotive, D.; Available from: http://delphi.com/manufacturers/auto/fuelcells/.

19. Winkler, W., *APPLICATIONS – TRANSPORTATION | Ships: Fuel Cells*. Encyclopedia of Electrochemical Power Sources, ed. J. Garche. 2009, Amsterdam: Elsevier. 338-358.

20. McConnell, V.P., *Military UAVs claiming the skies with fuel cell power.* Fuel Cells Bulletin, 2007. **2007**(12): p. 12-15.

21. Sehra, A.K. and W. Whitlow Jr, *Propulsion and power for 21st century aviation.* Progress in Aerospace Sciences, 2004. **40**(4–5): p. 199-235.

22. Aguiar, P., D.J.L. Brett, and N.P. Brandon, *Solid oxide fuel cell/gas turbine hybrid system analysis for high-altitude long-endurance unmanned aerial vehicles.* International Journal of Hydrogen Energy, 2008. **33**(23): p. 7214-7223.

23. Kim, T. and S. Kwon, *Design and development of a fuel cell-powered small unmanned aircraft.* International Journal of Hydrogen Energy, 2012. **37**(1): p. 615-622.

24. *Military funding, contracts for Adaptive Materials' SOFC power.* Fuel Cells Bulletin, 2008. **2008**(5): p. 9-10.

25. Lee, T.S., J.N. Chung, and Y.-C. Chen, *Design and optimization of a combined fuel reforming and solid oxide fuel cell system with anode off-gas recycling.* Energy Conversion and Management, 2011. **52**(10): p. 3214-3226.

26. Dietrich, R.-U., et al., *Efficiency gain of solid oxide fuel cell systems by using anode offgas recycle – Results for a small scale propane driven unit.* Journal of Power Sources, 2011. **196**(17): p. 7152-7160.

27. Chen, W.-H., et al., *Thermodynamic analysis of hydrogen production from methane via autothermal reforming and partial oxidation followed by water gas shift reaction.* International Journal of Hydrogen Energy, 2010. **35**(21): p. 11787-11797.

28. Biesheuvel, P.M. and J.J.C. Geerlings, *Thermodynamic analysis of direct internal reforming of methane and butane in proton and oxygen conducting fuel cells.* Journal of Power Sources, 2008. **185**(2): p. 1162-1167.

29. Yen, T.-H., et al., *Experimental investigation of 1kW solid oxide fuel cell system with a natural gas reformer and an exhaust gas burner.* Journal of Power Sources, 2010. **195**(5): p. 1454-1462.

30. Hawkes, A. and M. Leach, *Solid oxide fuel cell systems for residential micro-combined heat and power in the UK: Key economic drivers.* Journal of Power Sources, 2005. **149**(0): p. 72-83.

31. Andújar, J.M. and F. Segura, *Fuel cells: History and updating. A walk along two centuries.* Renewable and Sustainable Energy Reviews, 2009. **13**(9): p. 2309-2322.

32. Grgicak, C.M., R.G. Green, and J.B. Giorgi, *SOFC anodes for direct oxidation of hydrogen and methane fuels containing H2S.* Journal of Power Sources, 2008. **179**(1): p. 317-328.

33. Nagel, F.P., et al., *The impact of sulfur on the performance of a solid oxide fuel cell (SOFC) system operated with hydrocarboneous fuel gas.* Journal of Power Sources, 2009. **189**(2): p. 1127-1131.

34. Chen, Y., et al., *Chemical, Electronic and Nanostructure Dynamics on Sr(Ti1-xFex)O3 Thin-Film Surfaces at High Temperatures.* ECS Transactions,

2011. **35**(1): p. 2409-2416.

35. Inui, Y., et al., *Performance simulation of planar SOFC using mixed hydrogen and carbon monoxide gases as fuel.* Energy Conversion and Management, 2006. **47**(13–14): p. 1738-1747.

36. Kang, Y., et al., *One-dimensional Dynamic Modeling and Simulation of a Planar Direct Internal Reforming Solid Oxide Fuel Cell.* Chinese Journal of Chemical Engineering, 2009. **17**(2): p. 304-317.

37. Yang, Y., et al., *Investigation of methane steam reforming in planar porous support of solid oxide fuel cell.* Applied Thermal Engineering, 2009. **29**(5–6): p. 1106-1113.

38. Evans, W.K., et al., *The simulations of tubular solid oxide fuel cells (SOFCs).* Chemical Engineering Journal, 2011. **168**(3): p. 1301-1310.

39. Jiang, W., et al., *Parameter setting and analysis of a dynamic tubular SOFC model.* Journal of Power Sources, 2006. **162**(1): p. 316-326.

40. Nakajo, A., et al., *Modeling of thermal stresses and probability of survival of tubular SOFC.* Journal of Power Sources, 2006. **158**(1): p. 287-294.

41. Akhtar, N., S.P. Decent, and K. Kendall, *A parametric analysis of a micro-tubular, single-chamber solid oxide fuel cell (MT-SC-SOFC).* International Journal of Hydrogen Energy, 2011. **36**(1): p. 765-772.

42. Dhir, A., Improved Microtubular Solid Oxide Fuel Cells, 2008. **PhD thesis**: The University of Birmingham

43. Lee, S.-B., et al., *Development of a 700W anode-supported micro-tubular SOFC stack for APU applications.* International Journal of Hydrogen Energy, 2008. **33**(9): p. 2330-2336.

44. Sammes, N.M., Y. Du, and R. Bove, *Design and fabrication of a 100W anode supported micro-tubular SOFC stack.* Journal of Power Sources, 2005. **145**(2): p. 428-434.

45. Dhir, A. and K. Kendall, *Microtubular SOFC anode optimisation for direct use on methane.* Journal of Power Sources, 2008. **181**(2): p. 297-303.

46. Tsai, T.-I., et al., *Control system design for micro-tubular solid oxide fuel cells.*

International Journal of Low-Carbon Technologies, 2013.

47. Lanzini, A. and P. Leone, *Experimental investigation of direct internal reforming of biogas in solid oxide fuel cells.* International Journal of Hydrogen Energy, 2010. **35**(6): p. 2463-2476.

48. Lawlor, V., et al., *Review of the micro-tubular solid oxide fuel cell: Part I. Stack design issues and research activities.* Journal of Power Sources, 2009. **193**(2): p. 387-399.

49. Bujalski, W., C.M. Dikwal, and K. Kendall, *Cycling of three solid oxide fuel cell types.* Journal of Power Sources, 2007. **171**(1): p. 96-100.

50. Kendall, K., et al., *Effects of dilution on methane entering an SOFC anode.* Journal of Power Sources, 2002. **106**(1–2): p. 323-327.

51. Wang, K., et al., *A Review on solid oxide fuel cell models.* International Journal of Hydrogen Energy, 2011. **36**(12): p. 7212-7228.

52. Colclasure, A.M., et al., *Modeling and control of tubular solid-oxide fuel cell systems. I: Physical models and linear model reduction.* Journal of Power Sources, 2011. **196**(1): p. 196-207.

53. Bove, R., P. Lunghi, and N. M. Sammes, *SOFC mathematic model for systems simulations. Part one: from a micro-detailed to macro-black-box model.* International Journal of Hydrogen Energy, 2005. **30**(2): p. 181-187.

54. Akkaya, A.V., *Electrochemical model for performance analysis of a tubular SOFC.* International Journal of Energy Research, 2007. **31**(1): p. 79-98.

55. Xue, X., et al., *Dynamic modeling of single tubular SOFC combining heat/mass transfer and electrochemical reaction effects.* Journal of Power Sources, 2005. **142**(1–2): p. 211-222.

56. Serincan, M.F., U. Pasaogullari, and N.M. Sammes, *Effects of operating conditions on the performance of a micro-tubular solid oxide fuel cell (SOFC).* Journal of Power Sources, 2009. **192**(2): p. 414-422.

57. Akhtar, N., *Micro-tubular, single-chamber solid oxide fuel cell (MT–SC-SOFC) stacks: Model development.* Chemical Engineering Research and Design, 2012. **90**(6): p. 814-824.

58. Colpan, C.O., I. Dincer, and F. Hamdullahpur, *Thermodynamic modeling of direct internal reforming solid oxide fuel cells operating with syngas.* International Journal of Hydrogen Energy, 2007. **32**(7): p. 787-795.

59. Zhu, Y., et al., *Fuel ejector design and simulation model for anodic recirculation SOFC system.* Journal of Power Sources, 2007. **173**(1): p. 437-449.

60. Zhu, Y., Y. Li, and W. Cai, *Control oriented modeling of ejector in anode gas recirculation solid oxygen fuel cell systems.* Energy Conversion and Management, 2011. **52**(4): p. 1881-1889.

61. Cheddie, D.F. and R. Murray, *Thermo-economic modeling of a solid oxide fuel cell/gas turbine power plant with semi-direct coupling and anode recycling.* International Journal of Hydrogen Energy, 2010. **35**(20): p. 11208-11215.

62. Eveloy, V., *Numerical analysis of an internal methane reforming solid oxide fuel cell with fuel recycling.* Applied Energy, 2012. **93**(0): p. 107-115.

63. Kakaç, S., A. Pramuanjaroenkij, and X.Y. Zhou, *A review of numerical modeling of solid oxide fuel cells.* International Journal of Hydrogen Energy, 2007. **32**(7): p. 761-786.

64. Hajimolana, S.A., et al., *Mathematical modeling of solid oxide fuel cells: A review.* Renewable and Sustainable Energy Reviews, 2011. **15**(4): p. 1893-1917.

65. Rostrupnielsen, J.R. and J.H.B. Hansen, *CO2-Reforming of Methane over Transition Metals.* Journal of Catalysis, 1993. **144**(1): p. 38-49.

66. Soria, M.A., et al., *Thermodynamic and experimental study of combined dry and steam reforming of methane on Ru/ ZrO2-La2O3 catalyst at low temperature.* International Journal of Hydrogen Energy, 2011. **36**(23): p. 15212-15220.

67. Jasinski, P., et al., *Nanocomposite Nickel Ceria Cermet with Low Nickel Content for Anode-Supported SOFCs.* Electrochemical and Solid-State Letters, 2005. **8**(4): p. A219-A221.

68. Kawano, M., et al., *Steam reforming on Ni-samaria-doped ceria cermet anode for practical size solid oxide fuel cell at intermediate temperatures.* Journal of Power Sources, 2008. **182**(2): p. 496-502.

69. Wang, J.B., J.-C. Jang, and T.-J. Huang, *Study of Ni-samaria-doped ceria anode for direct oxidation of methane in solid oxide fuel cells.* Journal of Power Sources, 2003. **122**(2): p. 122-131.

70. Gaudillère, C., et al., *Screening of ceria-based catalysts for internal methane reforming in low temperature SOFC.* Catalysis Today, 2010. **157**(1–4): p. 263-269.

71. Prashanth Kumar, V., et al., *Thermal and electrical properties of rare-earth co-doped ceria ceramics.* Materials Chemistry and Physics, 2008. **112**(2): p. 711-718.

72. Leng, Y.J., et al., *Low-temperature SOFC with thin film GDC electrolyte prepared in situ by solid-state reaction.* Solid State Ionics, 2004. **170**(1–2): p. 9-15.

73. Chourashiya, M.G. and L.D. Jadhav, *Synthesis and characterization of 10%Gd doped ceria (GDC) deposited on NiO-GDC anode-grade-ceramic substrate as half cell for IT-SOFC.* International Journal of Hydrogen Energy, 2011. **36**(22): p. 14984-14995.

74. Modafferi, V., et al., *Propane reforming on Ni–Ru/GDC catalyst: H2 production for IT-SOFCs under SR and ATR conditions.* Applied Catalysis A: General, 2008. **334**(1–2): p. 1-9.

75. Wang, F.-Y., S. Cheng, and B.-Z. Wan, *Porous Ag–CGO cermets as anode materials for IT-SOFC using CO fuel.* Fuel Cells Bulletin, 2008. **2008**(5): p. 12-16.

76. Niakolas, D.K., et al., *Au-doped Ni/GDC as a new anode for SOFCs operating under rich CH4 internal steam reforming.* International Journal of Hydrogen Energy, 2010. **35**(15): p. 7898-7904.

77. Souentie, S., et al., *Mathematical modeling of Ni/GDC and Au–Ni/GDC SOFC anodes performance under internal methane steam reforming conditions.* Journal of Catalysis, 2013. **306**(0): p. 116-128.

78. Xu, J. and G.F. Froment, *Methane steam reforming, methanation and water-gas shift: I. Intrinsic kinetics.* AIChE Journal, 1989. **35**(1): p. 88-96.

79. Malyi, O.I., et al., *Density functional theory study of the effects of alloying additions on sulfur adsorption on nickel surfaces.* Applied Surface Science,

2013. **264**(0): p. 320-328.

80. Gong, M., et al., *Sulfur-tolerant anode materials for solid oxide fuel cell application.* Journal of Power Sources, 2007. **168**(2): p. 289-298.

81. Poppinger, M. and H. Landes, *Aspects of the internal reforming of methane in solid oxide fuel cells.* Ionics, 2001. **7**(1-2): p. 7-15.

82. Vernoux, P., J. Guindet, and M. Kleitz, *Gradual Internal Methane Reforming in Intermediate‐Temperature Solid‐Oxide Fuel Cells.* Journal of The Electrochemical Society, 1998. **145**(10): p. 3487-3492.

83. Cao, Y., et al., *Synthesis Gas Production with an Adjustable H2/CO Ratio through the Coal Gasification Process: Effects of Coal Ranks And Methane Addition.* Energy & Fuels, 2008. **22**(3): p. 1720-1730.

84. Majewski, A.J. and J. Wood, *Tri-reforming of methane over Ni@SiO2 catalyst.* International Journal of Hydrogen Energy, 2014. **39**(24): p. 12578-12585.

85. Oyama, S.T., et al., *Dry reforming of methane has no future for hydrogen production: Comparison with steam reforming at high pressure in standard and membrane reactors.* International Journal of Hydrogen Energy, 2012. **37**(13): p. 10444-10450.

86. Zhang, J., et al., *Thermodynamic and kinetic model of reforming coke-oven gas with steam.* Energy, 2010. **35**(7): p. 3103-3108.

87. Iwai, H., et al., *Numerical simulation of intermediate-temperature direct-internal-reforming planar solid oxide fuel cell.* Energy, 2011. **36**(4): p. 2225-2234.

88. Klein, J.M., et al., *Modeling of a SOFC fuelled by methane: From direct internal reforming to gradual internal reforming.* Chemical Engineering Science, 2007. **62**(6): p. 1636-1649.

89. Fuerte, A., et al., *Study of a SOFC with a bimetallic Cu–Co–ceria anode directly fuelled with simulated biogas mixtures.* International Journal of Hydrogen Energy, 2014. **39**(8): p. 4060-4066.

90. Darujati, A.R.S. and W.J. Thomson, *Kinetic study of a ceria-promoted catalyst in dry-methane reforming.* Chemical Engineering Science, 2006. **61**(13): p. 4309-4315.

91. Goula, G., et al., *Catalytic and electrocatalytic behavior of Ni-based cermet anodes under internal dry reforming of CH4 + CO2 mixtures in SOFCs.* Solid State Ionics, 2006. **177**(19–25): p. 2119-2123.

92. Moon, D.J. and J.W. Ryu, *Electrocatalytic reforming of carbon dioxide by methane in SOFC system.* Catalysis Today, 2003. **87**(1–4): p. 255-264.

93. Wei, J. and E. Iglesia, *Isotopic and kinetic assessment of the mechanism of reactions of CH4 with CO2 or H2O to form synthesis gas and carbon on nickel catalysts.* Journal of Catalysis, 2004. **224**(2): p. 370-383.

94. Hou, K. and R. Hughes, *The kinetics of methane steam reforming over a Ni/α-Al2O catalyst.* Chemical Engineering Journal, 2001. **82**(1–3): p. 311-328.

95. Massardo, A.F. and F. Lubelli, *Internal Reforming Solid Oxide Fuel Cell-Gas Turbine Combined Cycles (IRSOFC-GT): Part A—Cell Model and Cycle Thermodynamic Analysis.* Journal of Engineering for Gas Turbines and Power, 1999. **122**(1): p. 27-35.

96. Resini, C., et al., *Yttria-stabilized zirconia (YSZ) supported Ni–Co alloys (precursor of SOFC anodes) as catalysts for the steam reforming of ethanol.* International Journal of Hydrogen Energy, 2008. **33**(14): p. 3728-3735.

97. Wongsakulphasatch, S., W. Kiatkittipong, and S. Assabumrungrat, *Comparative study of fuel gas production for SOFC from steam and supercritical-water reforming of bioethanol.* International Journal of Hydrogen Energy, 2013. **38**(14): p. 5555-5562.

98. da Costa, L.O.O., et al., *The study of the performance of Ni supported on gadolinium doped ceria SOFC anode on the steam reforming of ethanol.* International Journal of Hydrogen Energy, 2012. **37**(7): p. 5930-5939.

99. Augusto, B.L., et al., *Ethanol reforming over Ni/CeGd catalysts with low Ni content.* International Journal of Hydrogen Energy, 2012. **37**(17): p. 12258-12270.

100. *Franklin's SOFC hits good power density on ethanol, Navy funding.* Fuel Cells Bulletin, 2005. **2005**(8): p. 8.

101. Santarelli, M., et al., *Direct reforming of biogas on Ni-based SOFC anodes: Modelling of heterogeneous reactions and validation with experiments.* Journal of Power Sources, 2013. **242**(0): p. 405-414.

102. Alves, H.J., et al., *Overview of hydrogen production technologies from biogas and the applications in fuel cells.* International Journal of Hydrogen Energy, 2013. **38**(13): p. 5215-5225.

103. Shiratori, Y., et al., *Internal reforming SOFC running on biogas.* International Journal of Hydrogen Energy, 2010. **35**(15): p. 7905-7912.

104. Staniforth, J. and K. Kendall, *Biogas powering a small tubular solid oxide fuel cell.* Journal of Power Sources, 1998. **71**(1–2): p. 275-277.

105. Woolcock, P.J. and R.C. Brown, *A review of cleaning technologies for biomass-derived syngas.* Biomass and Bioenergy, 2013. **52**(0): p. 54-84.

106. Yin, L., et al., *Simulation of effect of catalyst particle cluster on dry methane reforming in circulating fluidized beds.* Chemical Engineering Journal, 2007. **131**(1–3): p. 123-134.

107. Di Carlo, A., D. Borello, and E. Bocci, *Process simulation of a hybrid SOFC/mGT and enriched air/steam fluidized bed gasifier power plant.* International Journal of Hydrogen Energy, 2013. **38**(14): p. 5857-5874.

108. Lorente, E., M. Millan, and N.P. Brandon, *Use of gasification syngas in SOFC: Impact of real tar on anode materials.* International Journal of Hydrogen Energy, 2012. **37**(8): p. 7271-7278.

109. Aloui, T. and K. Halouani, *Analytical modeling of polarizations in a solid oxide fuel cell using biomass syngas product as fuel.* Applied Thermal Engineering, 2007. **27**(4): p. 731-737.

110. Li, C.-X., et al., *Microstructure, performance and stability of Ni/Al2O3 cermet-supported SOFC operating with coal-based syngas produced using supercritical water.* International Journal of Hydrogen Energy, 2012. **37**(17): p. 13001-13006.

111. Hackett, G.A., et al., *Performance of solid oxide fuel cells operated with coal syngas provided directly from a gasification process.* Journal of Power Sources, 2012. **214**(0): p. 142-152.

112. Zhan, Z., J. Liu, and S.A. Barnett, *Operation of anode-supported solid oxide fuel cells on propane–air fuel mixtures.* Applied Catalysis A: General, 2004. **262**(2): p. 255-259.

113. Langmuir, I., *THE ADSORPTION OF GASES ON PLANE SURFACES OF GLASS, MICA AND PLATINUM.* Journal of the American Chemical Society, 1918. **40**(9): p. 1361-1403.

114. Szekely, J., *Gas-Solid Reactions*. 2012: Elsevier Science.

115. Physics, U.C.f.C.C.a. [cited 2014 28, Oct]; Available from: http://www.chem.ucl.ac.uk/cosmicdust/er-lh.htm.

116. *Chapter 9 Heterogeneous catalysis*. Comprehensive Chemical Kinetics, ed. F.G. Helfferich. Vol. Volume 40. 2004: Elsevier. 273-308.

117. Hougen, O.A. and K.M. Watson, *General Principles.* Industrial & Engineering Chemistry, 1943. **35**(5): p. 529-541.

118. Kendall, K. *Proceedings of the international forum on fine ceramics*. in *International forum on fine ceramics*. 1992. Japan Fine Ceramics Center, Nagoya

119. Assabumrungrat, S., N. Laosiripojana, and P. Piroonlerkgul, *Determination of the boundary of carbon formation for dry reforming of methane in a solid oxide fuel cell.* Journal of Power Sources, 2006. **159**(2): p. 1274-1282.

120. Armor, J.N., *The multiple roles for catalysis in the production of H2.* Applied Catalysis A: General, 1999. **176**(2): p. 159-176.

121. Haag, S., M. Burgard, and B. Ernst, *Beneficial effects of the use of a nickel membrane reactor for the dry reforming of methane: Comparison with thermodynamic predictions.* Journal of Catalysis, 2007. **252**(2): p. 190-204.

122. Buccheri, M.A., A. Singh, and J.M. Hill, *Anode- versus electrolyte-supported Ni-YSZ/YSZ/Pt SOFCs: Effect of cell design on OCV, performance and carbon formation for the direct utilization of dry methane.* Journal of Power Sources, 2011. **196**(3): p. 968-976.

123. Liu, M., et al., *Anode recirculation behavior of a solid oxide fuel cell system: A safety analysis and a performance optimization.* International Journal of Hydrogen Energy, 2013. **38**(6): p. 2868-2883.

124. Girona, K., et al., *Carbon deposition in CH4/CO2 operated SOFC: Simulation and experimentation studies.* Journal of Power Sources, 2012. **210**(0): p. 381-391.

125. Piroonlerkgul, P., et al., *Selection of appropriate fuel processor for biogas-fuelled SOFC system.* Chemical Engineering Journal, 2008. **140**(1–3): p. 341-351.

126. Al-Nakoua, M.A. and M.H. El-Naas, *Combined steam and dry reforming of methane in narrow channel reactors.* International Journal of Hydrogen Energy, 2012. **37**(9): p. 7538-7544.

127. Maestri, M., et al., *Steam and dry reforming of methane on Rh: Microkinetic analysis and hierarchy of kinetic models.* Journal of Catalysis, 2008. **259**(2): p. 211-222.

128. Özkara-Aydınoğlu, Ş., *Thermodynamic equilibrium analysis of combined carbon dioxide reforming with steam reforming of methane to synthesis gas.* International Journal of Hydrogen Energy, 2010. **35**(23): p. 12821-12828.

129. Nikoo, M.K. and N.A.S. Amin, *Thermodynamic analysis of carbon dioxide reforming of methane in view of solid carbon formation.* Fuel Processing Technology, 2011. **92**(3): p. 678-691.

130. Blum, L. and E. Riensche, *FUEL CELLS – SOLID OXIDE FUEL CELLS | Systems*. Encyclopedia of Electrochemical Power Sources, ed. G. Editor-in-Chief: Jürgen. 2009, Amsterdam: Elsevier. 99-119.

131. Huang, K.G.J.B., *Solid oxide fuel cell technology : principles, performance and operations*. 2009, Cambridge, UK; Boca Raton, FL: Woodhead Pub. ; CRC Press.

132. Ackmann, T., *Mikromodellierung einer keramischen Hochtemperaturbrennstoffzelle.* Berichte des Forschungszentrums Julich, 2004. **4119**: Techn. Hochsch. Aachen Forschungszentrum, Zentralbibliothek

133. Takahashi, H., et al., *Effect of interaction between Ni and YSZ on coke deposition during steam reforming of methane on Ni/YSZ anode catalysts for an IR-SOFC.* Journal of Molecular Catalysis A: Chemical, 2011. **350**(1–2): p. 69-74.

134. Ni, M., D.Y.C. Leung, and M.K.H. Leung, *Electrochemical modeling and parametric study of methane fed solid oxide fuel cells.* Energy Conversion and Management, 2009. **50**(2): p. 268-278.

135. Matsuzaki, Y. and I. Yasuda, *Electrochemical Oxidation of H 2 and CO in a*

H2 - H2O - CO - CO2 System at the Interface of a Ni-YSZ Cermet Electrode and YSZ Electrolyte. Journal of The Electrochemical Society, 2000. **147**(5): p. 1630-1635.

136. Park, J., P. Li, and J. Bae, *Analysis of chemical, electrochemical reactions and thermo-fluid flow in methane-feed internal reforming SOFCs: Part I – Modeling and effect of gas concentrations.* International Journal of Hydrogen Energy, 2012. **37**(10): p. 8512-8531.

137. Roberts, R.A. and J. Brouwer, *Dynamic Simulation of a Pressurized 220 kW Solid Oxide Fuel-Cell--Gas-Turbine Hybrid System: Modeled Performance Compared to Measured Results.* Journal of Fuel Cell Science and Technology, 2006. **3**(1): p. 18-25.

138. Steinberger-Wilckens, R., et al., *Recent Results in Solid Oxide Fuel Cell Development at Forschungszentrum Juelich*. 2011.

139. Wang, Y., et al., *Performance and effective kinetic models of methane steam reforming over Ni/YSZ anode of planar SOFC.* International Journal of Hydrogen Energy, 2009. **34**(9): p. 3885-3893.

140. Oliveira, E.L.G., C.A. Grande, and A.E. Rodrigues, *Steam methane reforming in a Ni/Al2O3 catalyst: Kinetics and diffusional limitations in extrudates.* The Canadian Journal of Chemical Engineering, 2009. **87**(6): p. 945-956.

141. Fernandes, F.A.N. and A.B. Soares Jr, *Methane steam reforming modeling in a palladium membrane reactor.* Fuel, 2006. **85**(4): p. 569-573.

142. Campanari, S., *Thermodynamic model and parametric analysis of a tubular SOFC module.* Journal of Power Sources, 2001. **92**(1–2): p. 26-34.

143. Gubner, A., *Modelling of High Temperature Fuel Cells: The Thermal, Chemical, Electrochemical and Fluidmechanical Behaviour of Solid Oxide Fuel Cells Operating with Internal Reforming of Methane.* 1996. **PhD**: University of Portsmouth

144. Wang, H., et al., *Thermodynamic analysis of hydrogen production from glycerol autothermal reforming.* International Journal of Hydrogen Energy, 2009. **34**(14): p. 5683-5690.

145. NASA. *NASA Chemical Equilibrium with Applications (CEA).* [cited 2014 MAR 25]; Available from:

http://www.grc.nasa.gov/WWW/CEAWeb/ceaHome.htm.

146. Santarelli, M., et al., *Experimental evaluation of the sensitivity to fuel utilization and air management on a 100kW SOFC system.* Journal of Power Sources, 2007. **171**(1): p. 155-168.

147. Stiller, C., et al., *Control strategy for a solid oxide fuel cell and gas turbine hybrid system.* Journal of Power Sources, 2006. **158**(1): p. 303-315.

Appendix I: Mini-Project: Control System Design For A Solid Oxide Fuel Cell

Overview

Control systems are important for SOFC systems as they can increase the efficiency as well as extend the operating lifetime when implemented correctly. High operating temperatures allow more flexible fuel selection for SOFCs as they can be directly reform methane inside the cell. However, cracks can be caused a high fuel reformation rate and/or utilisation, as well as fast heating rates when the system is starting [146, 147]. This is generally because the thermal shock of ceramic cracking can occur due to large temperature gradients induced by the endothermic reforming reactions. On the other hand, relatively low fuel utilisations due to high inlet fuel flow rates imply low system efficiency.

The aim of this chapter is to design a control for a micro-tubular SOFC (μ-SOFC) to maintain the temperature of the furnace, as well as the fuel inlet flow rate. A data acquisition (DAQ) 6009 and Labview programme from National Instruments™, as well as some related electronic components were employed in the work. The control system diagram is shown in Figure A 1 and Figure A 2.

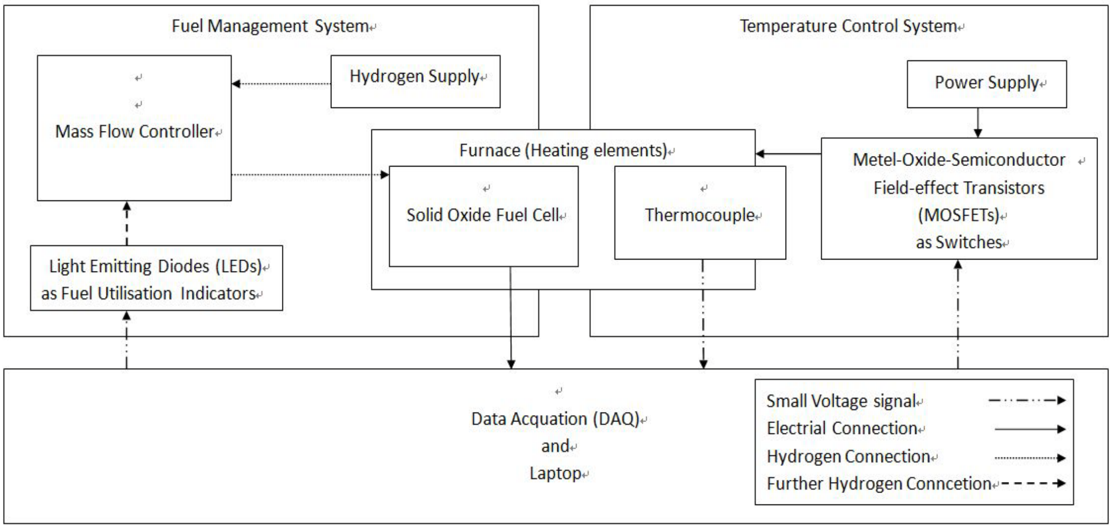

Figure A 1 Control system diagram for a micro-tubular SOFC.

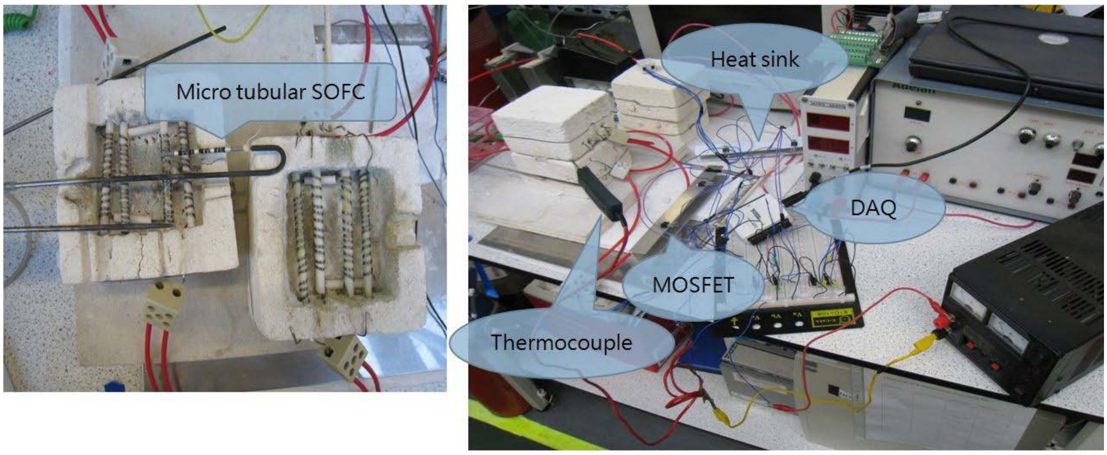

Figure A 2 The furnace and mirco-SOFC (left), and the set-up of a temperature control system (right).

Fuel Management

Fuel Flow Rate, Utilisation and Efficiency

Figure A 3 shows the average result from testing more than 12 μ-SOFC cells. An improvement of the electrical power output was shown when the inlet fuel rate was increased from 10 sccm to 20 sccm. When the inlet fuel flow rate was further increased to 30 sccm, the increase of output power was insignificant and a very low overall efficiency was observed. This result indicates that it is very crucial to control the fuel inlet flow rate. Because for any specific output power commonly required by the SOFC applications, there is a suitable fuel flow rate demand. A higher fuel flow rate causes a waste of energy in form of unused fuel, lowering the overall efficiency. A lower fuel flow rate leads to a higher fuel utilisation, however, can cause damages to the cell due to the high temperature gradient. A control system, therefore, is required to determine the fuel flow rate, allowing for optimisation of the systWem.

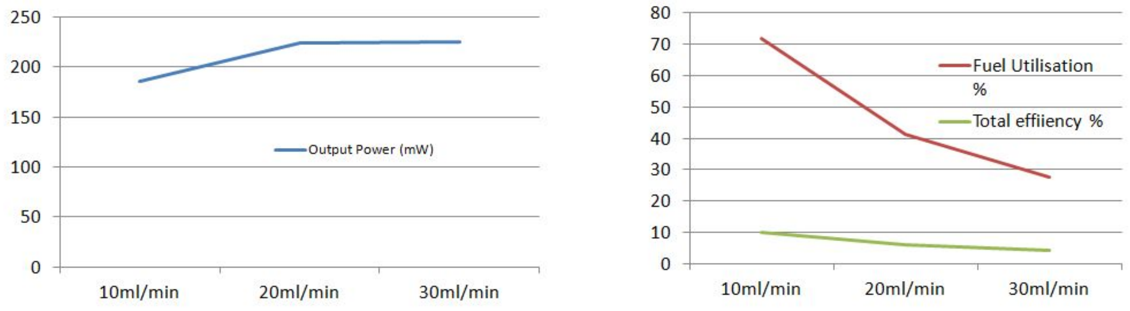

Figure A 3 The electrical output power (left), the overall efficiency and fuel utilisation (right).

under different hydrogen flow rate.

Fuel Control

The aim for the fuel controlling strategy is to control the inlet fuel flow rate to optimise the system performance. A UFC-7300 mass flow controller from Unit Instrument, which has ±1% accuracy, was employed in this work to control the inlet fuel flow rate. Electrical output wires of the SOFC were connected to the data acquisition unit and the output voltage and current data were sent to the computer. The overall efficiency (η) and fuel utilisation (U_f) were then calculated according to the formulae in Equation 3.58 and Equation 3.61, respectively.

Results

As a prototype of a control system, the fuel control is an open loop control system. Instead of a closed loop which the signals are used to control the MFCs for fuel management, Light Emitting Diodes (LEDs) were used in the experiments as in indicator.

Three different situations including high ($U_f > 75\%$), safe ($60\% \le U_f \le 75\%$), and low ($U_f < 60\%$) were obtained from the inlet fuel flow rate and SOFC output power.

Different voltage signals representing the decisions made, such as decreasing, maintaining, and increasing the inlet flow rate, were then sent from the computer through DAQ to the MFCs. MFCs for allowing feedback loops is expected in future work to make the system fully automatic. Since there are different output power requirements for most SOFC applications under different conditions, the closed fuel control system is expected to allow SOFCs to consume the fuel more economically and optimise the system as a whole.

Temperature Control

Furnace and Heating Up Facility

The furnace was formed of two hollowed thermal ceramic bricks, and the heating up facility is composed of four ceramic rods wound by four 80 cm Ni-Chrome wires. The wires were connected to the Metal-Oxide-Semiconductor Field-Effect Transistors (MOSFETs), employed as switches, and a 500 W power supply. A type K thermocouple was placed in the centre of the furnace close to the SOFC to monitor, and provide the temperature readings to the computer via DAQ. Voltage signals represent the computer decisions sent to the MOSFETs via DAQ to switch the heating circuits on or off.

The MOSFETs were attached to the aluminium heat sink/cooling rib to transfer the excess heat produced by a large current flow through the internal resistance to the surroundings. This was done as they might have damaged the MOSFETs as the furnace was being heated. Moreover, since the high resistance Ni-chrome wires used for heating up are highly inductive, diodes were placed parallel to the MOSFETs for preventing the counter Electromotive Force (EMF), as shown in Figure A 4.

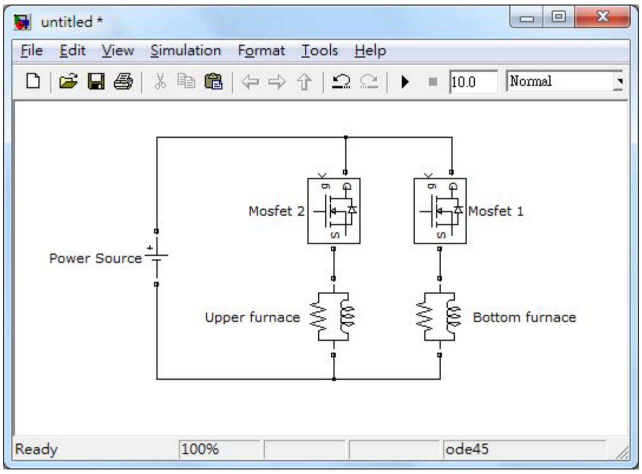

Figure A 4 The heating-up circuit.

Results

During the heating up stage, a type K thermocouple was placed inside the furnace to monitor the temperature and report back to the computer via DAQ, for recording and decision making. At temperatures below 725 ℃, signals were sent from the computer via DAQ, to the MOSFETs instructing them to keep the circuit closed. One set of

MOSFETs was turned off when the temperature was above 725 ℃. The other set remained on to generate heat for covering the heat losses and maintaining the temperature inside the furnace. The signal was regenerated to switch on the MOSFET again when the furnace was cooler than 715 ℃.

It can be seen from Figure A 5 that the temperature controller system was working as expected. With a time constant of about 173 seconds, the temperature steadily increased to 725 ℃ within 8.5 minutes. When the temperature reached 725 ℃, one set of MOSFETs was switched off by the signal from the computer, and the heat losses were counteracted by one set of heating circuits. As a result, the temperature has a ±5 ℃ fluctuation from the target value.

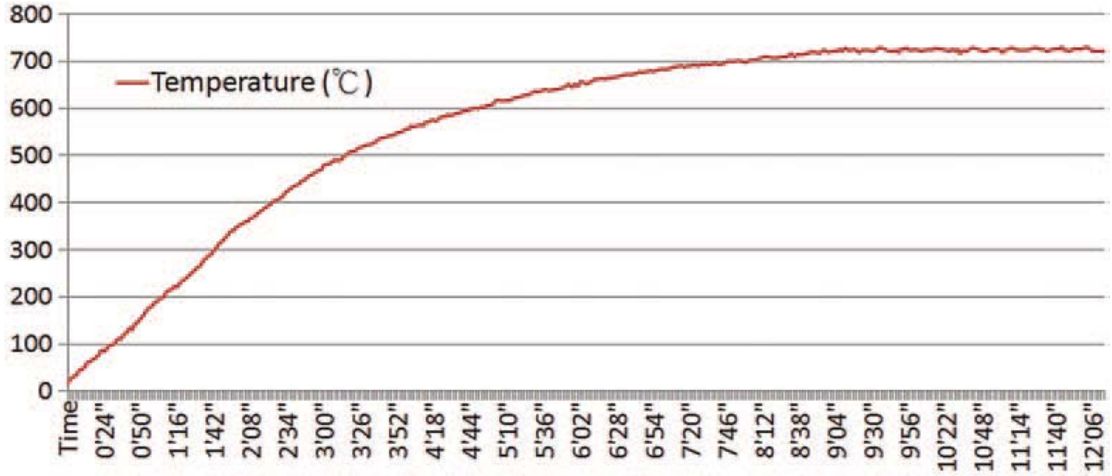

Figure A 5 The temperature of the furnace against time in heating up.

Discussions and Applications

The concept of controlling SOFC systems has been shown in this experiment. The LEDs give correct signals according to different fuel utilisation states. The heating equipment has successfully heated the system to the target temperature and remained approximately constant.

For the single cell study, 1.8 J of heat was produced under 50% fuel utilisation at 20 sccm fuel flow rate. Compared with the 500 W required by the furnace to heat up, the heat produced from a single cell is quite insignificant. Nevertheless, there could be up to thousands of cells in a stack for some SOFC applications. The heat from the stack would be much more than the heat discussed in this case, so it could be used to cover the heat losses and maintain the furnace temperature, as well as provide excess heat for a CHP unit.

The control system can be applied to the anode recirculation system. The component of exhaust gas can be predicted from the fuel utilisation. Since the amount of water and carbon dioxide in the exhaust are known, by using the carbon formation system mentioned in the previous chapter, the recycling rate required to prevent carbon formation can be determined. The appropriate signals can then be generated by the computer and sent to the valves and pumps to control the recycling flow.

The temperature control method can also be applied to the recirculation system. The same mechanism can be used for the heating up stage. As mentioned before, the heat produced by a stack could be huge and it will re-enter the system through the anode off-gas recirculation. The air inlet flow rate can be adjusted to control the temperature. Higher air flow rates are required if the system is overheated, and once the cooling has lowered the temperature below a critical level, the heating up circuit can be closed to produce heat, thus warning up the system again to the desired temperature.

Project Review and Conclusions

In this project, the design and build of the control system for controlling the flow rate and the furnace temperature were presented. The results show that a well-designed control system can optimise the system performance by using the energy more efficiently. However, this is just a control system for a single μ-tubular cell and the furnace is not ideally thermo-isolated. The first factor results in the insignificant heat and energy produced for self-heating and a very low efficiency. The latter factor leads to a high heat loss that requires half of the heating current being on all the time and again, lowers the system efficiency. These two drawbacks can be improved in future work when a μ-SOFC stack and furnace are employed. Moreover, the control system can also be applied for controlling the anode recirculation as it can calculate the fuel utilisation and has the ability to control the gas flow rate. This strategy allows the anode recirculation system to be more efficient and meanwhile prevent the carbon formation in the SOFC cells.

Appendix II: Funding Acknowledgements

Some sections of this research received funding from the European Union's Seventh Framework Programme (FP7/2007-2013) for the Fuel Cells and Hydrogen Joint Undertaking under grant agreement n° 278525 - MMLCR=SOFC.

Appendix III: Publications

- **Tsai T-I**, Majewski A, Wood J, Steinberger-Wilckens R, *"Methane Internal Reforming in SOFC with Anode Off-Gas Recirculation."* Journal of Power Sources (in preparation).
- **Tsai T-I**, Sands JD, Rong Y, Du S, Steinberger-Wilckens R, *"Steam Methane Reforming and Carbon Deposition."* Journal of Power Sources (in preparation).
- **Tsai T-I**, Du S, Dhir A, Williams AA, Steinberger-Wilckens R, *"Modelling a Methane Fed Solid Oxide Fuel Cell With Anode Recirculation System."* ECS Transactions. 2013;57:2831-9.
- **Tsai T-I**, Du S, Fisher P, Kendall K, Steinberger-Wilckens R, *"Control system design for micro-tubular solid oxide fuel cells."* IJLCT. 2013.